HYDROGEN DECREPITATION AND REPROCESSING OF Sm-Co MAGNETS

Anas Eldosouky

Doctoral Dissertation
Jožef Stefan International Postgraduate School
Ljubljana, Slovenia

Supervisor: Dr. Irena Škulj, Kolektor KFH d.o.o., Ljubljana, Slovenia
Co-Supervisor: Prof. Dr. Kristina Žužek Rožman, IPS and Jožef Stefan Institute, Ljubljana, Slovenia

Evaluation Board:
Prof. Dr. Sašo Šturm, Chair, IPS and Jožef Stefan Institute, Ljubljana, Slovenia
Prof. Dr. Boštjan Markoli, Member, Faculty of Natural Sciences and Engineering, University of Ljubljana, Ljubljana, Slovenia
Dr. Boris Saje, Member, Kolektor Magnet Technology GmbH, Essen, Germany

MEDNARODNA PODIPLOMSKA ŠOLA JOŽEFA STEFANA
JOŽEF STEFAN INTERNATIONAL POSTGRADUATE SCHOOL

Anas Eldosouky

HYDROGEN DECREPITATION AND REPROCESSING OF Sm-Co MAGNETS

Doctoral Dissertation

DEKREPITACIJA V VODIKU IN PREDELAVA MAGNETOV Sm-Co

Doktorska disertacija

Supervisor: Dr. Irena Škulj

Co-Supervisor: Prof. Dr. Kristina Žužek Rožman

Ljubljana, Slovenia, September 2019

Acknowledgments

I would first like to express my very deep gratitude to my supervisor, Dr. Irena Škulj, for supervising me without causing much stress and hence knowing when I needed to be pushed a little bit. I would like to thank her for the continuous scientific and personal support, without which I might have stopped the work at some point. I am very thankful to my co-supervisor, Prof. Dr. Kristina Žužek Rožman, for her continuous support of providing any scientific or practical help and for letting me use the equipment available in the Department for Nanostructured Materials at the Jožef Stefan Institute, where a large part of the experiments in this thesis was done. The thanks also go to Prof. Dr. Omneya El Hussaini from the Nuclear Material Authority of Egypt for helping me to get this position from scratch and doing all she could to ensure that.

I am very grateful to all the staff in my host company, Magneti Ljubljana d.d., for providing all the necessary equipment and for accepting my application in the first place. Also many thanks to Dr. Benjamin Podmiljšak and Prof. Dr. Sašo Šturm from the Jožef Stefan Institute for the help given scientifically and practically.

Some parts of the work mentioned here were done in secondments in the Katholieke Universiteit Leuven and Jožef Stefan Institute, in collaboration with Prof. Koen Binnemans, Martina Orefice, Awais Ikram and Farhan Mehmood, to whom I am very thankful for the help given and making the most out of the secondments.

The European Commission is truly much appreciated for every step taken to remove the barriers to science and letting minds meet from all over the world to solve worldwide problems by creating such effective programs as DEMETER project, which is the umbrella for this work. The research described here has received funding from the European Community's Horizon 2020 Programme [(H2020/2014-2019)] under Grant Agreement No. 674973 (MSCA-ETN DEMETER). I would like to thank all the supervisors and ESRs in the DEMETER project for putting all their efforts to work as one effective team for 3 years from 6 different countries.

I would also like to thank many colleagues for the training offered and sometimes performing the whole experiment or analysis mainly by themselves, Dr. Matejka Podlogar for microscopy, Xuan Xu for XRD analysis, Jan Balderman for casting and Almina Ahmetović for ICP-OES analysis.

Almina together with Larisa Suhodolčan, David Sojer and Miha Škof are heartily thanked for keeping a friendly and social atmosphere in and out of the workplace, which was a very key component for reaching the end of this PhD. Thanks to Ahmed Zohair for being my best friend for almost 15 years and for always being around. Thanks also to Arnab Chakraborty for the deep scientific and personal conversations throughout those 3 years.

Finally, but most importantly, thanks to my parents and my very beautiful two sisters and underappreciated brother for the pure, unconditional and continuous love and prayers. Sorry for not being by your side during all those years and for all the years to come.

Abstract

Sm-Co magnets are the second most widely industrially used REE-permanent magnets (REE: rare earth elements) after Nd-Fe-B. The magnets are used in a wide range of applications, such as electronics, aerospace and medical applications. Sm-Co provides the highest known coercivity and thermal stability values in the market. However the magnets are mainly composed of REE (Sm) and Co, and over the past 10 years the previous elements have been identified by the European Commission to be critical elements because of the risk of their supply resources; as their market is controlled by China and DRC, beside their very high economic importance. Moreover, REE-permanent magnets alone consume about 20% of the REE produced worldwide. Consequently, the recycling of Sm-Co magnets has been considered as an urgent solution to help maintain a sustainable source of those very important metals and magnets. In the work described here, Hydrogen Decrepitation (HD) has been applied as an effective way for the direct recycling of the two industrially produced types of sintered Sm-Co magnets; $SmCo_5$ and Sm_2Co_{17}. Hydrogen of a pressure of only 1 bar, room temperature for 3 hours was sufficient for the decrepitation of $SmCo_5$, however more severe conditions were required for the decrepitation of Sm_2Co_{17}; 20 bar of hydrogen gas for 2 days. The recycled magnets prepared by using more than 98 wt.% of the recycled decrepitated powder showed to have as good magnetic properties as the industrially produced ones, by using the conventional sintering route. The magnetic properties of the recycled $SmCo_5$ were remanence (B_r) = 0.95 T, intrinsic coercivity ($_iH_c$) > 1500 kA/m and maximum energy product ($(BH)_{max}$) of 171.1 kJ/m^3 and for Sm_2Co_{17} were B_r = 1.09 T, $_iH_c$ > 1500 kA/m and $(BH)_{max}$ = 218.3 kJ/m^3. Spark plasma sintering (SPS) has been studied as an alternative way for the consolidation of the recycled powder, where it was shown to be an effective route for producing isotropic $SmCo_5$ magnets with near full density and coercivity values similar to the conventionally sintered magnets. For Sm_2Co_{17}, the magnetic properties of the SPS-ed samples showed deterioration of $_iH_c$ to about 200 kA/m, which was related to the microstructure formation during the sintering process. Anisotropic polymer-bonded magnets were also produced from the recycled decrepitated powder with a very simple process of mixing the magnetic powder with a polymer binder followed by aligning, pressing and heating the pressed compact. The polymer-bonded Sm_2Co_{17} magnets showed to have promising properties of B_r = 0.58 T, $_iH_c$ > 1500 kA/m and $(BH)_{max}$ = 56 kJ/m^3. Because of the oxidation of the Sm element in $SmCo_5$ during the preparation of their polymer-bonded magnets, their $_iH_c$ was as low as 250 kA/m. As most of the industrially produced magnets are coated; usually with Ni-Cu-Ni, for protection from corrosion or chipping, and the presence of the coating residuals would deteriorate the magnetic properties of the recycled magnets, the possibility of removing the coating material from the recycled powder has been studied. By applying HD on the coated magnets, it was possible to sieve out the coating residuals from the decrepitated powder; where 98 wt.% of the coating was removed. The dissolution of the coating material was also studied by using 2M HNO_3 and 1 vol.% Br/organic systems, where it was shown that the latter system can be a promising route for the industrial application of the removal of the coating on the magnet's surface in a very short time of less than 20 min. To complete the picture, the effect of the presence of the coating residuals on the properties of Sm-Co magnets was studied, where it was shown that up to a coating content of 2 wt.% can be present in $SmCo_5$ magnets without decreasing its magnetic or mechanical properties. For Sm_2Co_{17} magnets, 1 wt.% was shown to be the maximum allowed concentration to be present without sharp negative effects on the properties of the magnets. Finally strip casting was also studied as an alternative recycling route of the Sm-Co magnets to be compared with HD, where very low recovery values of less than 50 wt.% were achieved.

Povzetek

Sm-Co magneti so drugi najpogosteje uporabljeni trajni magneti na osnovi elementov redkih zemelj, najbolj razširjeni so Nd-Fe-B magneti. Magneti se uporabljajo v najrazličnejše namene, tako v elektroniki, letalski in vesoljski industriji kot tudi v medicinske namene. Trenutno Sm-Co magneti zagotavljajo najvišjo koercitivnost in termično stabilnost. Magnete v glavnem sestavljata redka zemlja (Sm) in kobalt (Co). V zadnjem desetletju je Evropska komisija oba omenjena elementa zaradi negotovega vira prepoznala kot kritična. Dostopnost teh elementov na trgu nadzirata državi, ki imata njihove glavne vire; Kitajska ima elemente redkih zemelj, Kongo pa Co. Približno 20 % vseh izkopanih redkih zemelj se porabi za proizvodnjo magnetov. Glede na navedena dejstva je za ohranjanje trajnostnega vira teh strateških kovin najbolj smiselna uvedba reciklaže Sm-Co magnetov. Postopek hidrogenizacije z vodikom je bil uporabljen kot učinkovit postopek za direktno reciklažo obeh vrst Sm-Co sintranih magnetov; $SmCo_5$ in Sm_2Co_{17}. $SmCo_5$ magneti so uspešno razpadli že v 3 urah pri 1 bar vodika in sobni temperaturi, medtem ko so Sm_2Co_{17} magneti potrebovali bolj ostre pogoje; 2 dni v vodiku pri 20 bar. Raziskave so potrdile, da lahko več kot 98 ut.% recikliranega materiala zmešamo s svežim materialom in dobimo sintrane magnete z magnetnimi lastnostmi, ki so primerljive z originalnimi magneti. Magnetne lastnosti recikliranih $SmCo_5$ magnetov so: remanenca (B_r) = 0,95 T, koercitivnost ($_iH_c$) > 1500 kA/m in maksimalen energijski produkt ($(BH)_{max}$) = 171,1 kJ/m^3, magnetne lastnosti recikliranih Sm_2Co_{17} pa so: remanenca (B_r) = 1,09 T, koercitivnost ($_iH_c$) > 1500 kA/m in maksimalen energijski produkt ($(BH)_{max}$) = 218,3 kJ/m^3. Postopek sintranja z iskrečo plazmo (SPS) je alternativen postopek, ki se je izkazal kot primeren za sintranje izotropnih $SmCo_5$ magnetov iz recikliranega prahu z gostoto blizu teoretične gostote in koercitivnostjo, enakovredno konvencionalno sintranim magnetom. Postopek pa se ni izkazal kot primeren za izdelavo Sm_2Co_{17} magnetov. Sm_2Co_{17} magneti, sintrani s plazmo, imajo 200 kA/m nižjo koercitivnost, kar je posledica mikrostrukture, ki nastane med postopkom sintranja. Narejeni so bili tudi anizotropni polimerno- vezani magneti iz recikliranega prahu po preprostem postopku mešanja kovinskega prahu s polimernim vezivom. Homogena mešanica je bila usmerjena v magnetno polje, stisnjena in toplotno obdelana. Sm_2Co_{17} magneti so pokazali dobre magnetne lastnosti; B_r = 0,58 T, $_iH_c$ >1500 kA/m in $(BH)_{max}$ = 56 kJ/m^3. Slabšo koercitivnost $_iH_c$ >250 kA/m so pokazali $SmCo_5$ magneti, verjetno zaradi Sm faze, ki je oksidirala med samo pripravo mešanic. Večina proizvedenih magnetov je površinsko zaščitenih s plastjo Ni-Cu-Ni kot zaščito pred korozijo in okrušitvami. Preverili smo, do katere mere prisotnost prevleke nima negativnega vpliva na magnetne lastnosti. Raziskave so pokazale, da <2 ut.% ostankov Ni-Cu-Ni plasti ne moti pri $SmCo_5$ magnetih in <1 ut.% ostankov pri Sm_2Co_{17} magnetih. Pred postopkom reciklaže je torej treba večino te plasti odstraniti, ker negativno vpliva na magnetne lastnosti recikliranih magnetov. Raziskave so pokazale, da se 98 ut.% prevleke uspešno odstrani s postopkom sejanj\ po hidrogenaciji magnetov z zaščitno plastjo z vodikom. Preučen pa je bil tudi kemijski postopek odstranjevanja plasti z 2 M HNO_3 ali z 1 % Br v organski raztopini. Uporaba Br raztopine se je izkazala kot obetaven postopek, ki zaščitno plast z magneta odstrani že v kratkem času; do 20 minut. Končno smo kot postopek reciklaže preizkusili še postopek nalivanja taline na hlajeni valj (strip casting). Ugotovljeno je bilo, da so izkoristki tega postopka slabi, saj so nižji od 50 ut.%.

Contents

List of Figures

List of Tables

Abbreviations

at.%	… Atomic Percent
BSE	… Backscattered Electrons
cgs–emu	… Centimeter–Gram–Second–Electromagnetic Units
CVS	… Conventional Sintering
DMF	… Dimethylformamide
EDX	… Energy Dispersive X-ray
EG	… Ethylene Glycol
EtOAc	… Ethyl Acetate
HD	… Hydrogen Decrepitation
ICP-OES	… Inductively Coupled Plasma Atomic Emission Spectroscopy
MeOAc	… Methyl Acetate
MFM	… Magnetic Force Microscopy
Nd-Fe-B	… Neodymium Iron Boron
PA 12	… Polyamide 12
REE	… Rare Earth Elements
SE	… Secondary Electrons
SEM	… Scanning Electron Microscopy
SI	… International System of Units
Sm-Co	… Samarium Cobalt
SPS	… Spark Plasma Sintering
STEM	… Scanning Transmission Electron Microscopy
TEM	… Transmission Electron Microscopy
TM	… Transition Metal
vol.	… Volume Percent
wt.%	… Weight Percent
XRD	… X-ray Diffraction

Symbols

$(BH)_{max}$	… Maximum Energy Product
μ	… Material's Permeability
μ_0	… Vacuum's Permeability
µm	… Micrometer
μ_r	… Relative Permeability
B	… Magnetic Flux Density
${}_bH_c$	… Extrinsic Coercivity
B_r	… Remanence
Br_2	… Bromine
G	… Gauss
H	… Applied Field
H_2	… Hydrogen
HNO_3	… Nitric Acid
${}_iH_c$	… Intrinsic Coercivity
K	… Magnetocrystalline Anisotropy
kA m^{-1}	… Kiloampere per Metre
kJ m^{-3}	… Kilojoules per Metre Cubed
M	… Magnetisation
mg	… Milligram
MGOe	… Mega Gauss Oersted
mm	… Milimeter
mPa.s	… Milipascal-Second
µm	… Micrometer
M_s	… Saturation Magnetisation
Oe	… Oersted
ppm	… Parts Per Million
T	… Tesla
t	… Time
T_c	… Curie Temperature
α	… Reversible Temperature Coefficient of Remanence
β	… Reversible Temperature Coefficient of Coercivity
ρ	… Density
χ_m	… Magnetic Susceptibility

Some passages have been quoted verbatim from the following sources:

A. Eldosouky and I. Škulj, "Recycling of $SmCo_5$ magnets by HD process," *Journal of Magnetism and Magnetic Materials*, vol. 454, 249-253, 2018. Reference [1].

A. Eldosouky, A. Ikram, M. F. Mehmood, X. Xu, S. Šturm, K. Ž. Rožman and I. Škulj, "Hydrogen decrepitation and spark plasma sintering to produce recycled $SmCo_5$ magnets with high coercivity," *IEEE Magnetics Letters*, vol. 9, 1-4, 2018. Reference [2].

A. Eldosouky and I. Škulj, "Hydrogen Reaction with SmCo Compounds: Literature Review," *Journal of Sustainable Metallurgy*, vol. 4, 516–527, 2018. Reference [3].

Chapter 1

Introduction

1.1 History of Magnetism and Development of Magnetic Materials

The fundamentals and the scientific understanding of magnetism and magnetic materials were not explained until the beginning of the last century. However long before that, the phenomenon of magnetism was applied in many applications; quite accurately in some situations as in geomancy applications, and inaccurately in others as the one that led to the discovery of the Americas by Columbus as a result of confusing the North and South poles' directions.

It is believed that the first form of magnetism discovered in a material was observed in form of a rock called lodestone, named after lodestar, at least 2000 years ago [4]. Lodestone is just a stone rich in Fe_3O_4; magnetite, usually magnetized by lightning strikes. Chinese were the first to put the magnetic force in a useful application by simply carving a lodestone in the shape of a spoon, free to move on a base, the handle of the spoon is pointing towards the South pole, mostly used for geomancy applications. In 1088, the Chinese engineer Shen Kuo then invented the navigational compass [5]. The compass was reused/reinvented in Europe by the English Alexander Neckam in 1187 [6]. In 1269, Peter Peregrinus from France put his knowledge about lodestone in a letter describing the effect of self-carved loadstone to magnetize an iron needle and the attraction and repulsion between two pieces of loadstones, he is also the first to define the existence of North and South poles at the ends of the magnet; from this knowledge he proposed the possibility for the manufacturing of perpetual motion machine [7]. Around 1600, William Gilbert from England, who is known to be the father of electricity and magnetism, wrote what is considered by many to be the first scientific report about magnetism under the title "On the Magnet: Magnetic Bodies Also, and On the Great Magnet the Earth; a New Physiology, Demonstrated by Many Arguments and Experiments", identifying the source of the magnetic force for aligning the dipole of lodestone to be the rotating Earth itself, not a superstitious force or a star. In 1734, Daniel Bernoulli from Switzerland assembled the horseshoe magnet. Whereas, in 1745, Gowin Knight from England, was the first to develop self-synthesized permanent magnets of a paste containing powdered iron oxide [8].

The connection between magnetism and electricity was then observed in many occasions until it was explained by Hans Christian Ørsted, who in 1820 helped show in a theatrical event that magnetic force can be created in a coil carrying an electrical current. The previously mentioned horseshoe magnets were then replaced by the use of electromagnets after William Sturgeon in 1824. Further, the classical explanation of magnetism and its connection to electricity were studied by many great scientists such as André-Marie Ampère (1775–1836), Michael Faraday (1791–1867) and James Clerk Maxwell (1831–1879) [8]. This was followed by the use of quantum theory at the beginning of the last century for the distinction between different magnetic materials and their structures as will be discussed in the next chapters.

Around 1880, alloys of carbon steel containing 6% W or Cr were known to be relatively strong permanent magnets of that time, having a coercivity ($_iH_c$) = 4.4 kA/m and maximum energy product ($(BH)_{max}$) of about 2.4 kJ/m^3 [9]. Note: coercivity is a measurement for the energy required to demagnetize the magnet, maximum energy product is the amount of the magnetic energy stored in the magnet; further details are explained below. Those values were more than tripled by the addition of 30-40% Co to the previous steels as shown by the Japanese physicists Honda and Takagi, to reach values of

$_iH_c$ = 20 kA/m and $(BH)_{max}$ = 7.6 kJ/m^3 [10]. This was further studied by English manufacturers to produce grades of having lower Co content. In 1930, alloys of Al-Ni-Fe were shown to provide high $_iH_c$ and $(BH)_{max}$ values of 40 kA/m and 10 kJ/m^3, respectively. After the substitution of Fe with Co for the previous compound, and after heat treatment in the magnetic field, the properties were shown to increase to $_iH_c$ = 44 kA/m, and $(BH)_{max}$ = 36 kJ/m^3 [11]. By controlling the microstructure to produce a columnar grain structure, the $(BH)_{max}$ was further improved to 60 kJ/m^3. Ferrite magnets which are other permanent magnets of low coercivity value of composition close to $CoFe_2O_4$ were produced by Philips Organisation (USA) around 1940, where their development also led to the manufacturing of the first to be known as high coercivity ferrite permanent magnets of composition $MFe_{12}O_{19}$ (M=Ba, Sr, Pb), having for example for $SrFe_{12}O_{19}$, $_iH_c$ = 275kA/m and $(BH)_{max}$ = 28.2kJ/m^3. $MFe_{12}O_{19}$ were also produced in the form of polymer-bonded magnets after dispersion of its powder in a plastic binder [12].

A tremendous increase in the properties of the permanent magnets were shown by the materials composed of rare-earth elements (REE) and transition metals (TM), having a composition of RCo_5 (R = Y, Ce, Pr, Sm and Y-rich and Ce-rich mischmetals) by Strant et al. in 1966 [13]. The properties of the materials were first measured by preparing aligned powders in a plastic binder and measuring the magnetic properties parallel and perpendicular to the direction of the previous alignment, to show that the materials have a very high crystal anisotropy. Das [14] and Benz and Martin [15] then used the sintering technique for the production of the now industrially produced fully dense $SmCo_5$ magnets with $(BH)_{max}$ of 158 kJ/m^3, after the improvement of the alignment and the reduction of the particle size of the used powder to be lower than 10 μm. The title of the paper from Das was "Twenty million energy product samarium-cobalt magnet". Since the first invention of the $SmCo_5$ magnets, various experiments were carried out for the substitution of either Sm or Co by other REE or TM, until 1976 when Nagel et al. [16] prepared sintered $Sm(Co,Fe,Mn,Cr)_{8.5}$ and $Sm(Co,TM)_8$, TM = Fe or Cu, exhibiting high $_iH_c$ of 959 kA/m. The current industrially produced Sm_2Co_{17} magnets were then discovered by adding Zr of about 3 wt.% to form $Sm(Co, Fe, Cu, Zr)_z$ combined with long heat treatment, the measured $_iH_c$ for the sample of z equals 8.35 was 2069 kA/m [17].

Driven by the insanity of Co prices in 1980s, combined with the knowledge that the combination of REE and TM might produce magnets of high magnetic properties, Nd-Fe-B magnets were developed in 1982, simultaneously by General Motors (GM) [18] and Sumitomo Special Metals [19] in the form of polymer bonded and sintered magnets, respectively. The new magnet showed superior properties in terms of $(BH)_{max}$ in comparison with Sm-Co of a value of 290 kJ/m^3 for the sintered magnets, but it also shows lower temperature stability and $_iH_c$. However, enormous research has been carried out for the improvement of the $_iH_c$, temperature coefficients and corrosion resistance by microstructure optimization and metals' substitution in the magnets, especially the replacement of Nd with Dy. A value of $(BH)_{max}$ of 474 kJ/m^3 has already been achieved by NEOMAX Co. Ltd. [20] in 2005.

The latest known composition to serve as strong permanent magnets was developed by Coey and Sun [21] in 1990 of composition $R_2Fe_{17}N_y$ with $2.3<y<2.9$, (R = Ce, Pr, Nd, Sm, Gd, Tb, Dy, Ho, Er, Tm, Lu and Y). $Sm_2Fe_{17}N_{2.3}$ was introduced as a promising alloy for the development of stronger permanent magnets than the industrially produced Sm-Co magnets. However, $Sm_2Fe_{17}N_{2.3}$ is a metastable compound which decomposes above 550 ^oC to form SmN and α-Fe. Therefore, its applications are only limited to polymer-bonded magnets.

Figure 1.1 shows the development of permanent magnets in the last century, the amount of each material to provide the same magnetic energy product is also shown [22].

1.2 Origin of Magnetism and Magnetic Behaviours

Hund's rule predicts the total spin angular momentum quantum number (S), the total orbital angular momentum quantum number (L) and the total angular momentum quantum number (J) for a single atom or ion, which can be used for the theoretical calculation of the effective magnetic field (μ_{eff}) for the atom or ion in the ground state by using equation (1), where μ_B is the Bohr magneton and g_J is a factor, which can be calculated from equation (2).

$$\mu_{eff} = \mu_B g_J \sqrt{J(J+1)} \quad (1)$$

$$g_J = \frac{3}{2} + \frac{S(S+1) - L(L+1)}{2J(J+1)} \quad (2)$$

The presence of unpaired electrons would produce a non-zero dipole moment value for the atoms. As a simplified picture, the magnetic behaviour of a material is defined by how all the magnetic moments of the component atoms of the material react to external magnetic fields. Figure 1.2 shows the moments' behaviour in different materials after the application and removal of the external field, further explanation of the definitions is below.

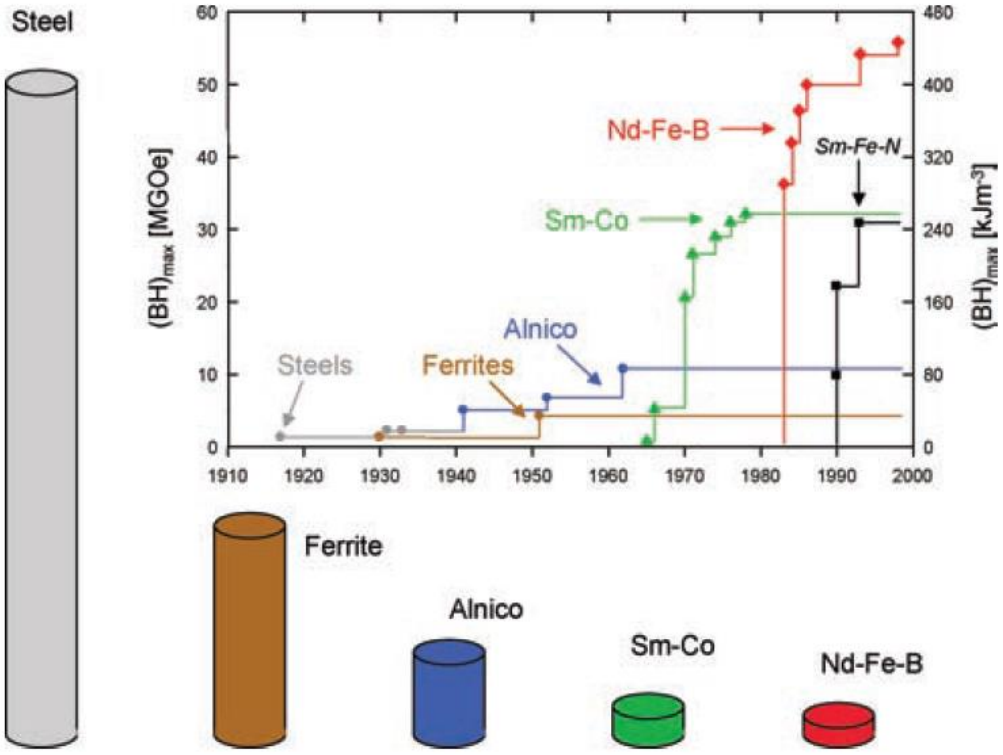

Figure 1.1: The enhancement of the magnetic energy product of the magnetic materials in the last century [22].

1.2.1 Diamagnetism

The atoms in diamagnetic materials possess a moment of a value of zero. After the application of the external field, the material repels the applied field, as magnetic moments are created inside the material which align themselves in a direction opposite to the field. When placed between two poles of a strong magnetic field, diamagnetic material is attracted towards the point where the field is the weakest.

1.2.2 Paramagnetism

Nevertheless, the component atoms in paramagnetic material show a directed magnetic moment; due to the presence of unpaired electrons. However, like diamagnetic materials, paramagnetic materials do not show permanent magnetic behaviour after the removal of the external field. This is due to the random distribution of the moments. Paramagnetic materials tend to be attracted towards the regions where the field is strong, as the moments align themselves in the same direction as the external field.

1.2.3 Ferromagnetism

Like paramagnetic materials, the atoms in ferromagnetic materials show a nonzero magnetic moment. Due to the exchange interactions between the different magnetic moments from different atoms in ferromagnetic materials, they tend to possess a permanent magnetic moment even after removing the external field, as there is parallel alignment of the magnetic moments in the material.

Bethe-Slater curve (Figure 1.3) describes the relation between the exchange interaction of the neighbouring magnetic moments as the ratio of the interatomic distance (r_{ab}) to the radius of the *d* shell (r_d) [23]. A positive value for the exchange constant (J_{exch}) is related to ferromagnetic behaviour.

1.2.4 Antiferromagnetism

Magnetic moments' interaction also happens in antiferromagnetic materials, however this leads to an antiparallel alignment of the moments; the J_{exch} value has a negative sign. This results in a net zero magnetic moment for the solid. An example of antiferromagnetic is manganese oxide (MnO).

1.2.5 Ferrimagnetism

Similar to ferromagnetism, ferrimagnetic materials also show a permanent magnetic moment after the removal of the external field. On the other hand, the magnetic structure of ferromagnetic materials contains two antiparallel alignments of magnetic moments, with one direction in excess. Magnetite; Fe_3O_4, is the most famous example for those materials.

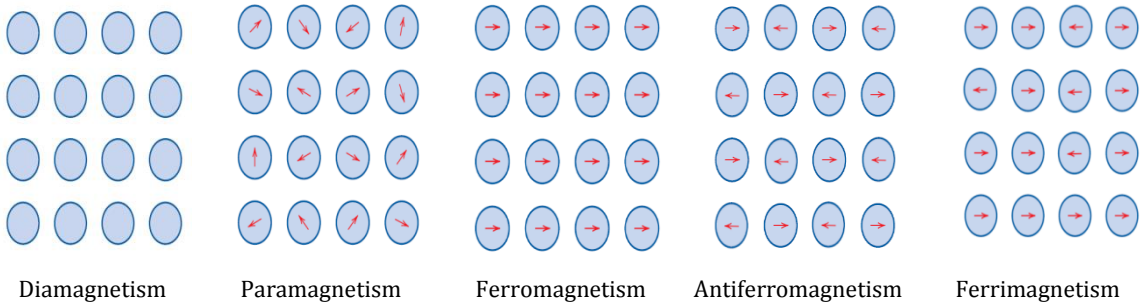

Figure 1.2: Magnetic behaviour characterization of materials after application and removal of an external field.

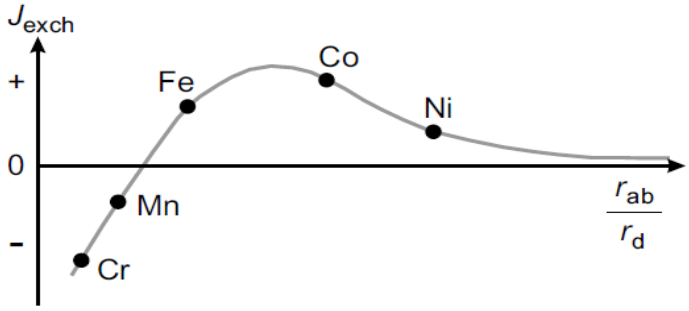

Figure 1.3: The Bethe–Slater curve to distinguish between ferromagnetic and antiferromagnetic materials [23].

1.3 Units of Magnetic Measurements

Different values and units may be used as indication for the magnetic classification of materials.

- Magnetization of a material (M): is a vector field which expresses the density of the dipole moments in the material.
- Susceptibility of a material (χ_m): is the material's magnetization M in response to an applied field H, $\chi_m = M/H$.
- Relative permeability (μ_r): is a measure for the ease with which the material can be magnetized, it equals to the material's permeability (μ)/permeability in vacuum (μ_0).
- Flux density (B): is the response of the material to an external field, it is calculated using the formula $\mu_0 H + \mu_0 M$.

The characteristic of magnetic materials of χ_m, μ_r and relation between B and H for diamagnetic, paramagnetic and ferromagnetic materials are shown in Table 1.1. Table 1.2 shows some basic magnetic units and their conversion factors between the SI and cgs–emu systems.

Table 1.1: Characterization of magnetic materials.

	Diamagnetism	Paramagnetism	Ferromagnetism
Susceptibility (χ_m):	$<0(-10^{-5})$	$>(10^{-5})$	$>>0$
Relative permeability (μ_r):	≤ 1	≥ 1	$>>1$
Direction of B relative to H	Opposite	Same	Hysteresis

Table 1.2: Magnetic Units and their conversion factors between the SI and cgs–emu [24].

	SI:- *Symbol: unit*	*cgs–emu:-* *Symbol: unit*	*Conversion*
Flux density	B: tesla (Wb/m^2)	B: gauss	1 Wb/m^2 = 10^4 gauss
Magnetic field strength	H: amp-turn/m	H: oersted	1 amp-turn/m = $4\pi \times 10^{-3}$ oersted
Magnetization	M: amp-turn/m	I: maxwell/cm^2	1 amp-turn/m = 10^{-3} maxwell/cm^2
Permeability of a vacuum	μ_0: henry/m	μ_0: unitless (emu)	$4\pi \times 10^{-7}$ henry/m = 1 emu
Relative permeability	μ_r: unitless	μ': unitless	$\mu_r = \mu'$
Susceptibility	χ_m: unitless	χ'_m: unitless	$\chi_m = 4\pi\chi'_m$

1.4 Magnetic Anisotropy Effects

Magnetization of the materials which show collective magnetism of ferromagnetism or ferrimagnetism is done by aligning the magnetic moments by an external magnetic field. After removing the external magnetic field, a reversal in magnetization may be opposed by the anisotropic forces. The direction of the magnetization is only determined by the anisotropic forces; nevertheless the exchange energy is usually much higher than the

anisotropic forces. There are many forms of the magnetic anisotropies, the most important ones are:

- Magnetocrystalline anisotropy: it is an intrinsic property which occurs due to the spin-orbit interactions of the electrons. As the electrons are linked to a certain crystallographic structure, these interactions lead to preferred crystalline axes for the magnetization which are called easy axes. Hard axis is a term used for crystallographic orientation where it is not preferred for the magnetic moments to be aligned. Magnetocrystalline anisotropy constant (K) can be measured by the energy required to rotate the magnetization vector from an easy axis to a hard one. Magnetocrystalline anisotropy depends on the material and temperature.
- Shape anisotropy: the macroscopic shape of the solid affects the magnetization. For non-spherical samples, the shape of the sample will cause magnetization preferences in certain directions.
- Induced magnetic anisotropy: tempering the sample in an external magnetic field can stabilize certain magnetization directions.

1.5 Magnetic Domain Structures

Domains are areas within ferromagnetic or ferrimagnetic materials where the magnetic moments are aligned parallel to each other due to the exchange interaction. Each domain exhibits a net magnetic field; Figure 1.4 shows an example of different domains in the same material. Before magnetization of the materials, these net magnetic fields are aligned randomly. An external magnetic field is required to align the domains' magnetic moments parallel to each other by the orientation of the individual magnetic moments. Domains are important in specifying the magnetic behaviour of a material. Domains in the materials which are easy to be magnetized and demagnetized (soft magnets) are usually larger than in the materials which are hard to be magnetized and demagnetized (hard magnets).

The domain wall is the transition region between the domains. The domain walls can be classified by the angle between the magnetic moments in two neighbouring domains with the wall as a boundary. 180° walls, the moments are oriented in opposite direction. 90° walls, the magnetization is perpendicular in the two domains. The occurrence of different types of domain walls in the material depends on the crystallographic arrangement; for example, hcp-Co exhibit a uniaxial behaviour with 180° domain wall only, while fcc-Ni shows 180°, 109° and 107° angles. Through magnetization and demagnetization, domain wall movement might occur and this movement can be pinned by the presence of defects in the material.

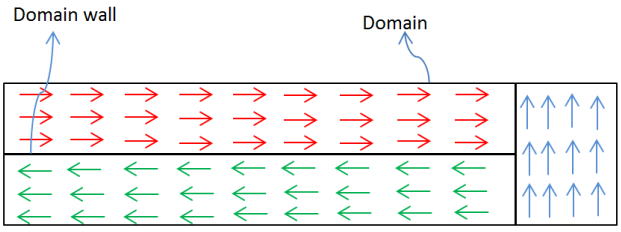

Figure 1.4: Domains in ferromagnetic or ferromagnetic materials (before magnetisation). The transition regions between the domains are called domain walls.

1.6 Hysteresis and Magnetic Properties

There is an irreversible-nonlinear relation between the B and M for ferromagnetic or ferrimagnetic materials with the applied H filed. This behaviour is due to the domains existence and formation in the material by the application of the external field. Figure 1.5 shows the hysteresis behaviour upon the application of H field. The first quadrant of the hysteresis loop represents when an applied field is used to align the domains in a material. Increasing the field would result in more domains to be aligned parallel to each other, up to where all the domains in the material are aligned in the same direction and saturation for the magnetization occurs; saturation magnetization can be represented as M_s. The presence of anisotropic forces, as discussed above, may oppose the magnetization reversal upon removal of the external field. A reverse external field $-H$ has to be applied for the demagnetization of the material, as shown in the second quadrant. By the $-H$ application, first some domains will start to align themselves in the same direction as the opposite field, for the complete demagnetization of the material, the domain walls have to be moved. The third and fourth quadrants are essentially mirrors for the first two. From the previous figure some magnetic properties can be identified:

- Remanence (B_r): is the amount of magnetism the magnet persists after magnetic saturation by an external magnetic field. Remanence is an extrinsic property of permanent magnets and it depends on the volume fraction and saturation magnetization of each phase in the microstructure, the alignment of the phases and the density which is achieved during the manufacturing process.
- Coercivity: is the resistance of the magnet to be demagnetized by an external magnetic field. A distinction is made between intrinsic ($_iH_c$) and extrinsic coercivity ($_bH_c$) as the demagnetization field required to reduce the $4\pi M$ and B to zero, respectively, Figure 1.5. Coercivity is an important parameter to characterize the magnets. There are three important mechanisms which affect the coercivity:
    - Nucleation of reverse domains: by application of a reverse external magnetic field on a magnetized sample, the moment of the domains will first resist the orientation by the external magnetic field. After a specific field magnitude, the moment will change their direction and this results in the deterioration of the magnetic properties. The presence of inhomogeneities, such as irregularities in the grain boundaries, can provide a nucleation point for the reverse domains to occur. Heat treatment is usually performed to reduce the inhomogeneities in the sample.
    - Domain wall pinning: is the pinning of the movement of the domain walls, for example due to the presence of defects in the sample as inclusions or dislocations in the crystal structure of the material. Usually a higher external magnetic field is required to overcome the domain pinning sites than the ones required to initiate the nucleation of reverse domains.
    - Single domain particles grains: this occurs by reducing the grain size of the material so they only have one domain within them. When this happens, a reverse domain cannot occur and nucleate in the grain and the demagnetization occurs through flipping the moments from one direction to another which usually needs higher reverse external magnetic fields.
- Maximum magnetic energy product: $(BH)_{max}$ is the maximum magnetic energy stored in the magnet. It is calculated from the product of $_bH_C$ and B_r by creating the largest square in the demagnetization quadrant. $(BH)_{max}$ is the main parameter used when comparing between the efficiency of different magnets. The SI unit for $(BH)_{max}$ is kJ/m^3 which equals 0.1256 MGOe in the cgs–emu system.

1.7 Curie Temperature

Temperature resistance is another important value to characterise permanent magnets and it specifies the range of the application for each magnet. Curie temperature (T_c) *is* generally used as an indication for the temperature stability of the magnets. T_c is the temperature at which permanent magnets lose their permanent magnetic properties. Co has the highest T_c of 1388 K (~ 1115 °C) among other known materials. Other values of the reversible temperature coefficient of remanence (α), and coercivity (β), which are the decrease of the value of the measured quantity by increasing the temperature by one Celsius, are also important in magnets' characterizations.

Table 1.3 shows a comparison between the above-mentioned magnetic properties of some industrially produced sintered REE-permanent magnets [20], [22], [25], [26], [27], [28], [29].

1.8 Soft Magnetism vs Hard Magnetism

Ferromagnetic and ferrimagnetic materials can be classified as soft or hard (permanent) magnets. Soft magnets show high μ_r and low ${}_iH_c$ (usually less than 1 kA/m) and so they show a weak net magnetic moment after the removal of the external field. Examples of soft magnetic materials are Fe-Si and Ni-Fe alloys. On the other hand, permanent magnets are those that create their own persistent magnetic field when magnetized by an external magnetic field. They are characterized by high ${}_iH_c$ (more than 10 kA/m) and $(BH)_{max}$. Sm-Co and Nd-Fe-B are examples of hard magnets.

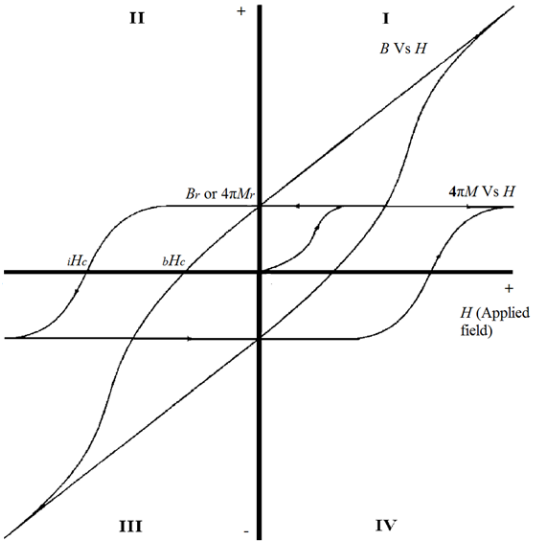

H	Applied field (Oe)
$4\pi M$	Magnetization (G)
B	Flux density (G)
B_r	Remanence (G)
${}_iH_c$	Intrinsic coercivity (Oe)
${}_bH_c$	Extrinsic coercivity (Oe)
$4\pi M_r$	Remnant magnetization (G)

Figure 1.5: Hysteresis curves for permanent magnets.

Table 1.3: Comparison between industrially produced sintered REE-permanent magnets [20], [22], [25], [26], [27], [28], [29].

	$SmCo_5$	Sm_2Co_{17}		Nd-Fe-B
Structure	$CaCu_5$	Th_2Zn_{17}	Th_2Ni_{17}	-
Symmetry	hex	rh	hex	tetr
Space group	Pb/mnm	$R\bar{3}m$	P63/mmc	P42/mnm
Product $(BH)_{max}$ (kJ/m³)	130-160	150-282		200-474
Anisotropy constant K (MJ/m³)	15-19	4.2		4.9
Reversible temperature coefficient of B_r (%/◦C)	-0.05	-0.03		-0.12
Product coercivity $_iH_c$ (kA/m)	1592 – 2400	450 – 2000		750 - 2000
Remanence B_r (T)	0.80 - 0.96	0.90 - 1.2		1.0-1.4
Curie temperature T_c (◦C)	750	850		320

hex: hexagonal, rh: rhombohedral, tetr: tetragonal

1.9 Scheme of the Dissertation and Hypothesis

The main goal of the dissertation is to look at the possibility of the industrial application of the Hydrogen Decrepitation (HD) process as a first step for the recycling of sintered $SmCo_5$ and Sm_2Co_{17} magnets. An introduction of the scheme and the steps of the different methods for the industrial preparation and production of sintered and polymer-bonded REE-permanent magnets will be described in the first part of Chapter 2. The market, the economic importance and the possibility of the recycling of the magnets will then be shown. The third part of Chapter 2 will give a detailed background on the magnetic properties, the sintering mechanism and the effect of different elements on the $SmCo_5$ and Sm_2Co_{17} magnets. The present literature on the use of HD on Sm-Co magnets will be described in details in the part 4 of the Chapter, where the effects of different conditions, such as the particle size, the chemical composition, the microstructure, the pressure, the exposure time, the temperature, and the heat treatment on enhancing the hydrogen absorption for Sm-Co compounds will be given in detail.

All the properties of the materials and the methods with the relevant utilized instruments that have been used or applied in this work will be shown in Chapter 3. The results and discussion section; Chapter 4 is divided into two parts for $SmCo_5$ and Sm_2Co_{17}. HD is first applied on fresh as-cast $SmCo_5$ and Sm_2Co_{17} alloys and Sm metal to give insights about the applicability of the process. The HD is then proceeded to be applied on sintered magnets, where it is expected that sintered magnets will need more severe conditions for decrepitation in comparison to the as-cast alloys. This is due to the decrease of the REE-rich phases in the magnets during the sintering step. It is also expected that the presence of higher REE content in the $SmCo_5$ magnets will lower the hydrogen pressure needed for the decrepitation, in comparison to Sm_2Co_{17} magnets. Studying of the lowest hydrogen pressure required for the disintegration of the sintered magnets at different experimental setups was performed, with studying the properties of the produced powder after

applying the HD process. The decrepitated powder was then proceeded to prepare recycled sintered or polymer-bonded magnets; to give flexibility on the way in which the recycled powders can be used, and their properties were compared with the original magnets before decrepitation. Two processes of conventional sintering (CVS) and spark plasma sintering (SPS) were used for the consolidation of the decrepitated powders to produce sintered magnets. The conditions needed for the near-full densification of the recycled magnets will be studied for the SPS procedure, and the properties will be compared with the conventionally sintered magnets. For $SmCo_5$, SPS is expected to be an efficient way for the densification due to the simplicity of the microstructure, in comparison with Sm_2Co_{17}. Due to the expected oxygen increase in the decrepitated powders during the recycling steps; additions of fresh as-cast alloy and/or metallic powder might be needed in order to improve the properties of the recycled magnets. As most industrially produced magnets are coated, the presence of the coating residuals in the decrepitated powder is expected to act as a source of contamination and hence to have a negative effect on the properties of the recycled magnets. This will be systemically studied by the preparation of Sm-Co magnets with different coating contents and to study the change in the microstructures and the magnetic properties of the magnets. Solvometallurgy route will also be studied for the dissolution of the coating layers on the magnets surface. Different chemicals will be used for effective fast removal of the coating with minimum dissolution of the magnets' components. Another route to be studied for the coating removal is to sieve the coating residual produced by the decrepitation of the coated magnets. It is expected that the presence of the coating layers on the magnets surface would increase the hydrogen pressure required for the decrepitation in comparison to the uncoated magnets. Strip casting was also used as a comparative way for the recycling of the sintered magnets after melting them, and studying the properties of the produced alloys. A large amount of slag is expected to be produced during the casting of the magnets, which will decrease the recovery. This is because of the presence of a higher amount of oxygen content in the magnets to be recycled, in comparison to the pure elements. Figure 1.6 shows the scheme for all the practical work that has been done in the dissertation. The conclusions of the results and the expected future work are shown in Chapter 5.

Appendix A will give a brief overview about the health and safety concerns combined with reproduction of the work done. Some functions of REE-permanent magnets in some industrial devices will be shown in Appendix B, for giving the reader an insight of the real uses of them.

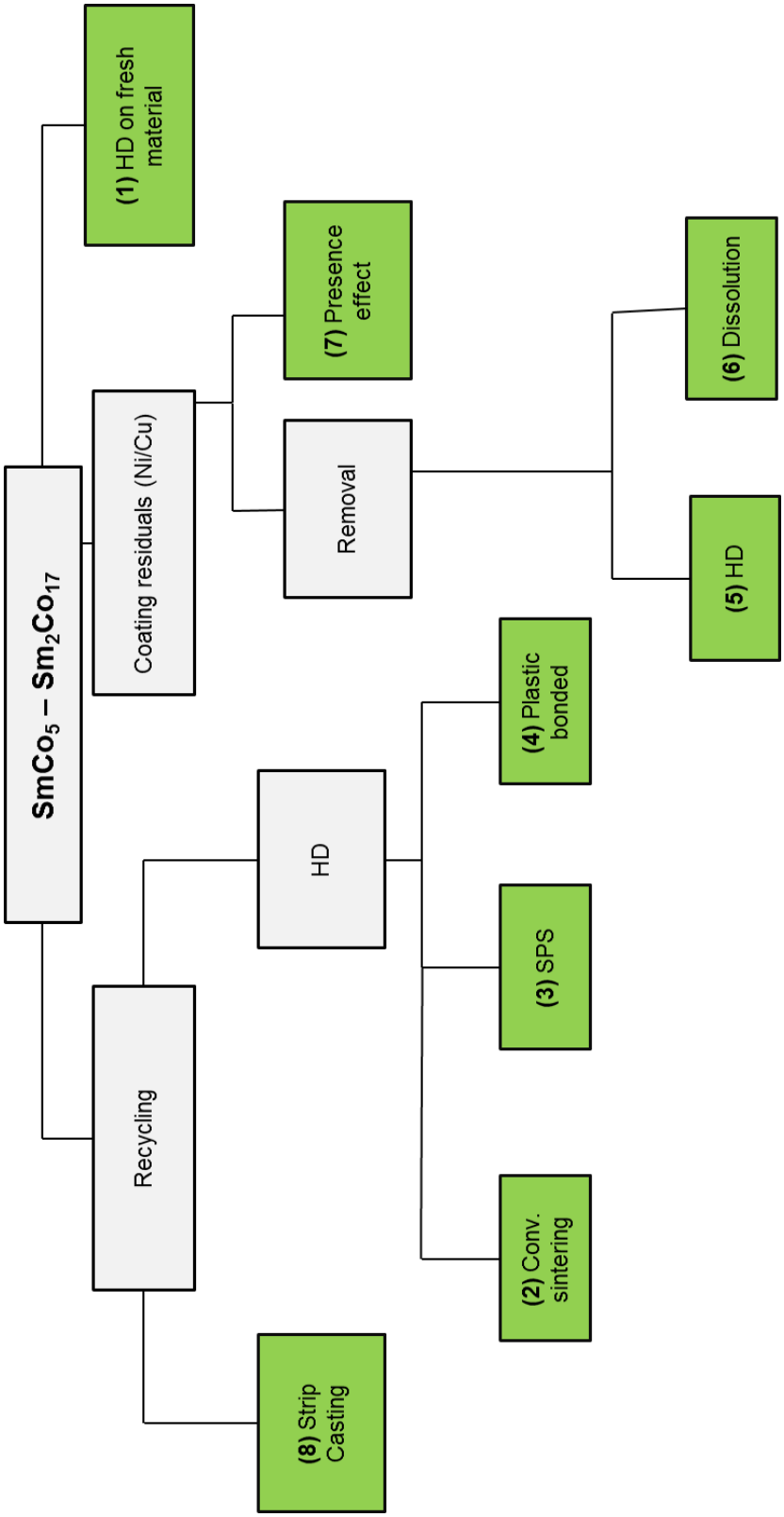

Figure 1.6: The scheme for all the practical work. The last categories are numbered according to their order of appearance in Chapter 4 (results and discussion).

Chapter 2

Literature Review

2.1 Preparation Methods of Permanent Magnets

2.1.1 Sintered permanent magnets

The preparation steps of the industrially produced sintered permanent magnets usually start with melting of the metal components having the required compositions, under an oxygen-free atmosphere. The liquid melt is then usually cast in moulds to produce solid as-cast alloys (book moulding). There are other ways in which the liquid melt could be solidified, e.g. by strip casting, which is usually used for the production of Nd-Fe-B magnets. The melt in strip casting is poured onto a fast rotating wheel, where it solidifies instantly into flakes. For Nd-Fe-B, strip casting has the advantages of reducing the grain size of the produced alloy and the elimination of the free Fe content. This results in the reduction of the energy required for the subsequent treatment and improves the properties of the produced magnets [30]. In order to be suitable for near-fully dense magnets production, the cast alloy first has to be crushed to particle size of around 0.5 mm. Mechanical crushing is usually used for the production of Sm-Co magnets industrially. For Nd-Fe-B, hydrogen decrepitation (HD) is famously used for the crushing of the alloys. A literature review on the application of HD with emphases on Sm-Co compounds will be discussed in the next chapters. The crushed material is then milled to a powder of less than 20 μm usually by the use of jet milling. The powder is then pressed in the presence of a magnetic field to produce anisotropic magnets; axial pressing or isostatic pressing are usually used for industrial production to achieve a density of about 70% of the fully dense material. The pressed compact, i.e. green compact, is then sintered to achieve near-full density. Conventional sintering (CVS) is traditionally used for magnets' production; however, spark plasma sintering (SPS) is an emerging technique which is expected to be applied more widely in the future, further details on the two processes are below. Sintered magnets are usually further processed by slicing and/or grinding, followed by coating to protect the surface of the magnets from chipping and/or oxidation. Figure 2.1 shows an example of the processing route for the production of permanent magnets industrially [31].

2.1.1.1 Conventional sintering

CVS is a compaction process to increase the density of objects under the effects of heat and/or pressure. This densification occurs without melting the material to its point of liquefaction. The microstructure of the material before the sintering step is often destroyed during the process, and the change in the temperature and pressure cycles during sintering may lead to different physical properties. One example of sintering mechanisms in CVS is liquid phase sintering, where one component of the material has lower melting point than the matrix. The melting point of this component is reached, which leads to the densification of the whole object; through atoms rearrangement, solution-precipitation and final densification. Protective gas is usually required for metal sintering in order to prevent the oxidation. CVS is an effective process for the formation of high pure materials with low porosity and high strength and other mechanical properties.

2.1.1.2 Spark plasma sintering

SPS is a process where a pulsed DC current passes through a die, which contains the powder of interest. The process is usually combined by an applied pressure. The mechanism of densification in SPS is different than CVS, where CVS consists of slow diffusion mechanisms such as grain boundary and volume diffusions. On the other hand, SPS is a rapid densification technique, where only the surface of the particle experiences localized heating, with no observed contribution from the bulk of the particles [32]. Zhaohui et al. [33] described the densification mechanism in SPS to consist of four steps; 1) powder activation and refining, 2) formation of sintering neck; these steps involve removing the surface oxide and heating the powder due to the voltage breakdown effect and formation of the neck by evaporation and condensation and diffusion, 3) growth of the sintering neck, and 4) plastic deformation densification, usually enhanced by the applied pressure. (2)

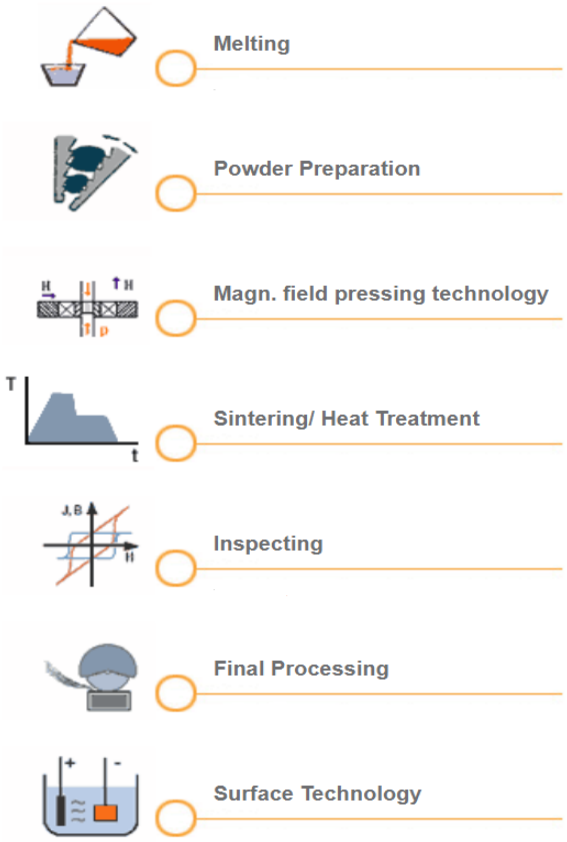

Figure 2.1: Preparation steps for permanent magnets [31].

Due to the local heat generation, the sintering temperature required for the full densification of the powder is usually lower than the one required for the CVS, with much lower sintering time as low as minutes in comparison to days sometimes for CVS. There are many parameters which can be optimized in the SPS experiments, as the pressure applied, the heating rate, the sintering temperature, the holding time and the partial pressure. The SPS technique is now a well-established technique for the production of Nd-Fe-B magnets of high coercivity and excellent magnetic properties [34], [35]. Moreover, the use of the SPS for the sintering of $SmCo_5$ magnets was shown to be an effective technique for the preparation of bulk nanocrystalline $SmCo_5$ or SmCo/Fe(Co) of good magnetic properties. Zhang et al. [36] and Yue et al. [37] used SPS for the preparation of bulk nanocrystalline $SmCo_5$ magnets. They showed that ${}_iH_c$ value of 2273 kA/m and a B_r value of 0.5 T can be achieved by using ball milled $SmCo_5$, where the sintering temperature was 700 ^oC at an applied pressure as high as 500 Mpa (5000 bar). Fang et al. [38] showed

that the use of wet-milling for the preparation of the $SmCo_5$ results in the oxidation of the powder during the processing, and the formation of Sm_2Co_{17}, with a decrease of $_iH_c$ of the magnets to a value as low as 280 kA/m. Saravanan et al. [39] studied the magnetic properties and microstructure of $SmCo_5$/Fe nanocomposite bulk magnets at different temperatures between 700-850 ^oC, 75 Mpa (750 bar), where the highest $_iH_c$ of 654 kA/m was achieved at 800 ^oC, where the produced magnet had a composition of mainly $Sm(Co,Fe)_5$ with other secondary phases such as $Sm_2(Co,Fe)_{17}$ and α-Fe(Co). Where Saito and Nishio-Hamane [40] showed that decreasing the sintering temperature to 600 ^oC results in an enhancement in the coercivity to 980 kA/m. Lu et al. [41] showed that the $BH_{(max)}$ value for the SPS-ed $SmCo_5$ can be improved by the addition of Nd-Fe-B, $BH_{(max)}$ of 115 kJ/m^3 was obtained for Sm-Co/Nd-Fe-B (4:1), which is 50% higher than the single phase $SmCo_5$ magnets. Figure 2.2 shows a schematic of a SPS device [42]. (2)

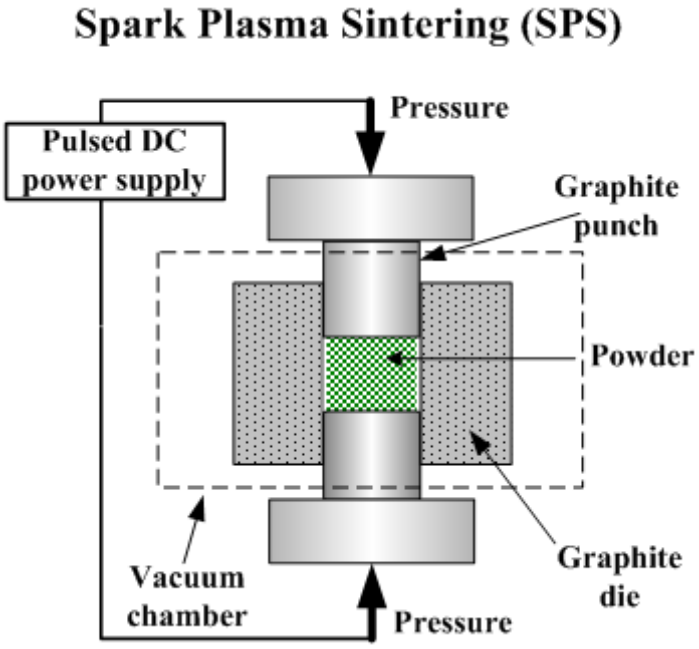

Figure 2.2: A schematic of a SPS device [42].

2.1.2 Polymer-bonded permanent magnets

Polymer-bonded permanent magnets are made by mixing a polymer binder with a metallic powder having permanent magnetism characteristics. In comparison to sintered permanent magnets, polymer-bonded magnets require a much easier production scheme and less time. They can be produced at much lower costs, in comparison to sintering that requires much finer powders' particle size and usually much longer heat treatment. Moreover, they can be produced in almost any shape, which is a technical problematic issue for sintered magnets [43]. On the other hand, due to the presence of a non-magnetic polymer portion in the polymer-bonded magnets; they usually offer lower magnetic properties in comparison to the sintered ones.

Nowadays, polymer-bonded magnets have a great industrial importance as they are used in important applications as in automotive applications and electronics. Moreover, the production of the polymer bonded magnets is growing and it is expected to further replace sintered magnets in many applications. Continuous development is on the way to produce polymer-bonded magnets of better magnetic properties and compression strength. The market of polymer-bonded magnets is expected to reach $2.5 billion by 2025 in comparison to $194 million in 1997 [44].

Compression moulding and injection moulding are the most common methods to produce bonded magnets for the industrial applications. In the compression moulding approach, the magnetic powder is coated with the binder, the mix is then compacted at

high pressures and dried. The process provides the possibility to use more magnetic to plastic powders and hence to produce magnets of better magnetic properties than the ones from injection moulding. On the other hand, injection is being used to produce more complex shapes that cannot be produced by compression. In injection moulding, a liquefied mix of the magnetic powder with a thermoplastic binder is fed to a mould of a required shape, where it hardens.

2.1.3 Coating on permanent magnets

Permanent magnets are usually coated in order to provide corrosion resistance; especially for Nd-Fe-B, and/or for chipping and medical purposes. Magnets can be coated with various options depending on the composition of the magnet itself and the applications required. Ni-Cu-Ni is the most commonly used coating for permanent magnets; due to its high protection resistance and working temperature and a relatively low price. However, various other coatings are used in the industry, e.g. Zn, Ni, Ni-Cu and epoxy. Table 2.1 shows a comparison for the coatings usually found on the magnets in terms of protection resistance, thickness and maximum working temperature [45]. The application of Ni-Cu-Ni coating alone presents about 8% of the total cost for the production of the magnets. The coating is usually carried out by a series of electrodepositions of the coating metals. Figure 2.3 shows an example of the coating on Nd-Fe-B magnets, the total thickness of the coating is around 20 μm [46].

Table 2.1: Types of coating usually applied on permanent magnets [45].

Surface treatment	Typical thickness (μm)	Colour	Remarks	Recommended max. temperature
Ni-Cu-Ni	10-20	Silver (semi-bright)	Superior resistance to humid atmosphere	200 °C
Zn	8-20	Silver blue	Excellent resistance to salt spray	160 °C
Ni-Cu-Sn	15-20	Silver (semi-bright)	Superior resistance to humid atmosphere	160 °C
Ni-Cu	10-20	Gold shining	Temporary treatment	-
Ni-Cu-epoxy or single epoxy	15-25	Black	Excellent climatic and salt spray resistance	120 °C
Passivation	0.1-0.3	Silver grey	Temporary protection	240 °C

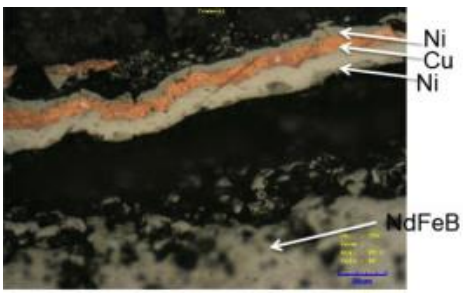

Figure 2.3: Confocal laser microscope image of cross section Ni-Cu-Ni layer on Nd-Fe-B [46].

2.2 Permanent Magnets Market and Recycling Options

2.2.1 REE and Co: economic importance and prices insatiability

Since the first successful separation of the REE for the application in the nuclear field around 1950, they gained huge industrial impact due to their magnetic, luminescent, chemical and electrochemical properties [47]. This permits their use in a wide spectrum of important applications, such as in catalysts, fertilizers, optoelectronics, pharmaceutical, magnets and semiconductors, Figure 2.4 [48]. This reflects the technical and economic importance of the REE. But, the highest reserves of the elements are found in China, which produces about 95% of the world production of REE. The market of applications of Co metal is also wide, basically being used in batteries and superalloys besides many other industrial applications, such as in magnets and adhesives, Figure 2.5 [49]. Co supplies are highly concentrated in the Democratic Republic of the Congo, which currently produces about 65% of its worldwide production. This means inequivalent control for the supply of those very economically and industrially important elements and a possibility for a monopoly of their resources, as previously happened in 1980s where the prices of the Co element increased by about 500% [50] and also in 2011 where some of the REE prices were increased by about 700% [51].

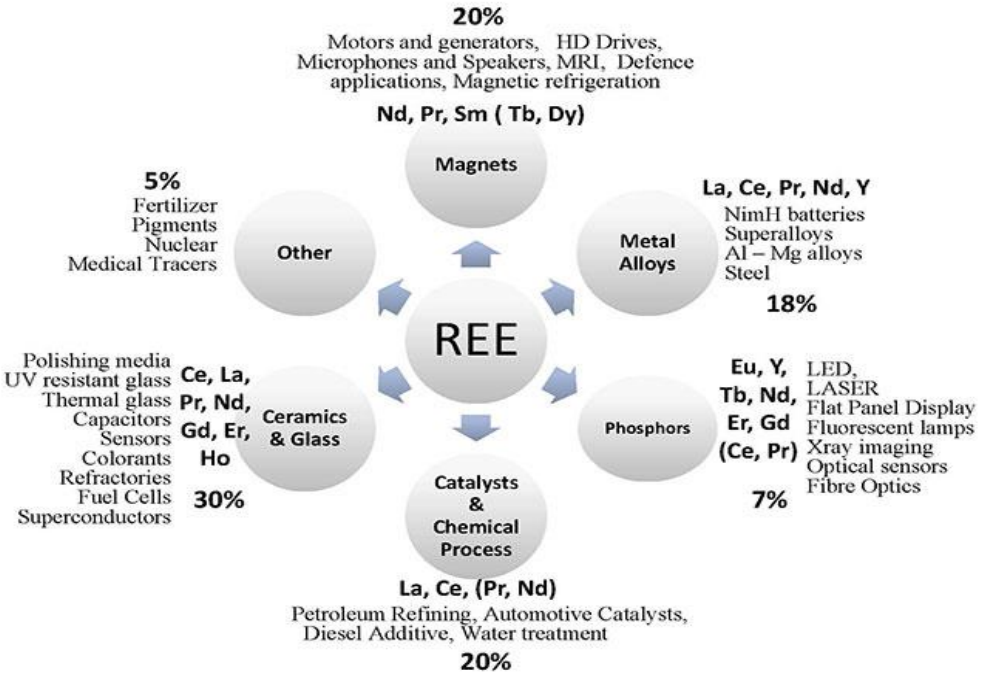

Figure 2.4: Applications of REE before 2014 [48].

2.2.2 Production market and applications

The importance of permanent magnets lies in the fact that they are used in widespread technical applications as in aerospace, automotive and electronic applications. Appendix A shows some examples about the functions of permanent magnets in some industrial devices. The market of permanent magnets nowadays is dominated by Nd-Fe-B magnets with more than 60% of production. Ferrite, Sm-Co and Alnico, come later with percentages of production of about 34%, 3% and 1%, respectively [22]. This scheme is expected to further change in the future for the favor of REE-permanent magnets, even though ferrite and Alnico are cheaper, due to the better properties of the former. Figure 2.6 [52] shows an example of the expected growth of the REE-permanent magnets market in the US and their attributed applications. The increase was predicted to be around 100% in less than 10 years which reflects the technological usage of the magnets. The previous study also

expects that Sm-Co magnets would have a bigger market share in the near future, basically due to the instability of the REEs in Nd-Fe-B magnets. Moreover, Sm-Co magnets provide much better corrosion stability and coercivity values, and this makes them incomparable for high temperature applications.

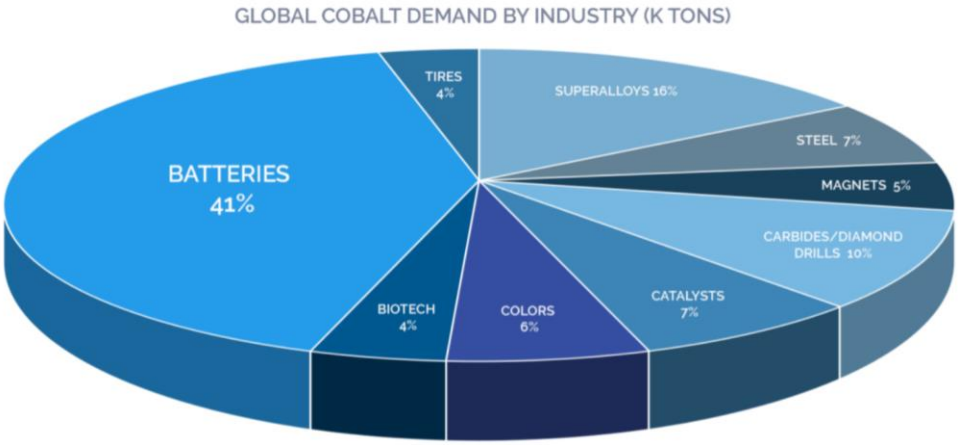

Figure 2.5: Applications of Cobalt element, 2016 [49].

The market of permanent magnets production is highly controlled by China as they have the largest resources of REE. In 2007, it was calculated that China alone produces more than 60% of the worldwide sintered and bonded permanent magnets. Europe comes in the second place with 8.6% followed by Japan with 8%. Europe produces as little as 3% of the worldwide produced Nd-Fe-B [44].

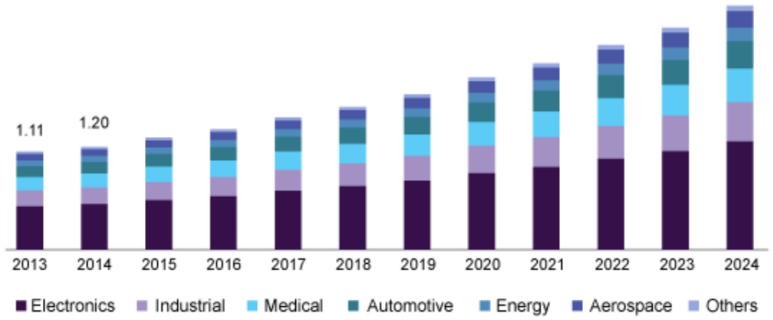

Figure 2.6: 10 years predication of REE-permanent magnets' market and their applications size in USA (USD Billion) [52].

2.2.3 Recycling options

In the last three reports of the European Commission (in 2011, 2014 and 2017), Co and most of the REE were identified as the most critical elements for Europe, this due to their technical importance and their big supply risk as previously explained [53], [54], [55]. The European Commission proposed three solutions for that problem; to recycle REE and Co compounds, to substitute the elements in their industrial compounds or to open new mines for them. Among the previous, recycling option is the most suitable in terms of time, cost and environmental aspects. REE-permanent magnets, namely Nd-Fe-B and Sm-Co, were defined as first candidates for the recycling, as they alone consume more than 20% of the worldwide produced REE and also they contain a very high amount of Co, this is beside their economic impact. This was reflected by the creation of many European fully-

funded projects on the recycling of permanent magnets as REMANENCE [56], EREAN [48], MAG-DRIVE [57] and DEMETER [58], the latter is the umbrella for this thesis.

2.2.3.1 Indirect recycling

Indirect recycling route includes the dissolution of the elemental components of the magnet mostly by dilute acids. After the dissolution, the elements are separated from the solution and precipitated, then they can be proceeded to be used in new magnetic materials or in other applications. Xu et al. [59] used sulphuric acid to leach Sm ion from Sm-Co magnetic scrap of a particle size of 200 mesh at 80 ^{o}C for 1 hour. After precipitation with oxalic acid, Sm-oxalate was roasted to form Sm-oxide with total Sm recovery of 96%. Jingjing et al. [60] used dilute hydrochloric acid (2-4 M) at 80 ^{o}C for leaching. The disadvantages of the indirect recycling are the hazards associated with the use of chemicals for extraction, the time and cost required for the extraction of the elements from the magnets and reprocessing them again to produce new products, the difficulties in detaching and handling the magnets from their assemblies, the requirement to grind the magnet before leaching and the difficulties in handling the magnetic powders.

2.2.3.2 Direct recycling

Direct recycling involves the use of magnets and magnetic scraps as raw materials for the production of new magnets after the conversion to recycled powder, which takes the cycle of magnets production again. There are also some problems that are being faced for the direct recycling of the permanent magnets; as the magnets are usually magnetized and embedded in the products, the presence of coating materials on the magnets' surface and the high oxidation content of the magnets in comparison to the fresh cast alloys. Melting and HD will be compared here as examples for the direct recycling route.

2.2.3.2.1 Melting

The material to be recycled is melted under Ar atmosphere. Most of the oxides in the material's microstructure tend to float on the top of the melt, since it has a lower molecular weight than the base alloy. The oxide layer is then removed from the top of the melt, where the rest is being cast. The cast is then reprocessed again to produce permanent magnets, through milling, pressing and sintering. The main problem of the melting route is that more than 30% of the material is being discarded when removing the oxide layer, moreover, the process needs special machinery and labour work for melting and casting.

2.2.3.2.2 Hydrogen decrepitation

The use of HD process for the recycling of permanent magnets involves the same steps as its use in preparation of fresh magnets (as described for Nd-Fe-B), except hydrogen gas is applied on the sintered magnets to be recycled. The produced decrepitated powder can be then processed for the production of recycled magnets. Recently, Walton et al. reported the possibility to use the HD process for the recycling of Nd-Fe-B magnets from end-of-life products, where 90% of the magnetic properties of the original magnet have been recovered after recycling [46]. With the proper optimization of the conditions of HD, it is possible to process all the decrepitated powder to magnets production without discarding any part of it. However, HD has the disadvantage of the possibility for the need of high pressures as will be discussed for Sm-Co compounds. HD can also be used as a first step for the magnets crushing in the indirect recycling route. However no literature is known to apply HD as a crushing procedure and a preference for other crushing techniques, such as hammering is shown.

2.2.3.2.3 The presence of coating residues

The presence of the coating material on the magnets to be recycled represents a technical problem for the removal before the recycling step, as the presence of the coating residuals would act as a contamination source which would differ the microstructure of the recycled magnets. This would lead to a decrease in the magnetic phases and changing the coercivity mechanisms with negative effects on the values of B_r and the coercivity of the recycled magnets, respectively. For example, when applying HD for the recycling of Ni-Cu-Ni-coated

sintered Nd-Fe-B magnets by Walton et al. [46]. After decrepitation of the magnets by a pressure of 10 bar and sieving of the decrepitated powder to remove the coating particles, a concentration of less than 330 ppm of Ni contamination was found in the magnetic sieved portion. This results in a 10 % drop of the magnetic properties of the recycled magnets prepared from the latter in comparison to the original one.

2.3 Sm-Co Magnets and Their Properties

2.3.1 $SmCo_5$

$SmCo_5$ has a hexagonal structure with a space group Pb/mnm, Figure 2.7. $SmCo_5$ exhibits a very high K and thus a high anisotropy field of 31.840 kA/m. Industrially produced magnets show a high ${}_iH_c$ value of 1592-2400 kA/m. The theoretical value of the $(BH)_{max}$ of $SmCo_5$ is 244.9 kJ/m^3 but industrially they usually have a $(BH)_{max}$ of 130-160 kJ/m^3. $SmCo_5$ magnets also show a high T_C value of 750 ^{o}C and low α = -0.05%/^{o}C and β = -0.5%/^{o}C, which allow them to be used in high temperature applications. They show a B_r value of 0.8-0.96 T [25], [27], [28].

The sintering mechanism for $SmCo_5$ magnets is a liquid phase sintering of the Sm-rich phases with compositions close to Sm_2Co_7 and Sm_5Co_{19}. The sintering process starts with the rearrangement of the liquid phases between the particles followed by solid phase solution and precipitation, which leads to the formation of the solid skeleton as a result of coalescence. Chemical heterogeneity is introduced through grain boundaries which hinders their growth during the sintering process [15]. Figure 2.8 shows the phase diagram of the binary Sm-Co compounds [61].

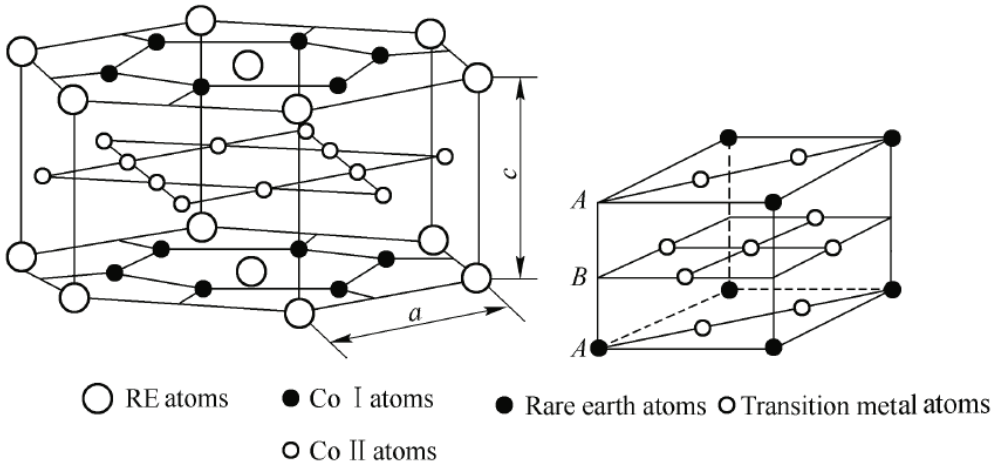

Figure 2.7: The $CaCu_5$ hexagonal crystal structure showing the position of Sm and Co in the cell for $SmCo_5$ [25].

2.3.1.1 Microstructure, magnetic structure and microchemistry

The microstructure of the $SmCo_5$ magnets consists of a matrix $SmCo_5$ phase, other ferromagnetic phases (Sm-Co), oxides (Sm-O), a recently reported carbide (Sm-Co-C) and pores [62],[63],[64]. Szmaja et al. used scanning electron microscopy (SEM), energy dispersive X-ray (EDX) and magnetic force microscopy (MFM) to study the morphology and microstructure of $SmCo_5$ [64]. In MFM, the magnetic structure of the material's surface is constructed by the scanning of a magnetized sharp tip on the surface of the sample and the detection of the interaction between the tip and the sample. Figure 2.9 shows the backscattered electron (BSE) image of the magnet. By recording the EDX spectra from small areas, they identified four different regions; 1- Dark-grey region corresponding to the main $SmCo_5$ matrix phase, 2- Light-grey regions: a mixture of Sm_2Co_7 and Sm_5Co_{19} phases, 3- Brightest regions of a small size: Sm-rich phase and Sm-oxides, 4- Black spots corresponding to pores. Figure 2.10 shows the MFM in the thermally demagnetized state of the magnet at the surface perpendicular to the magnetization alignment axis. The magnetic structure consists of domains of a few micrometer widths which form a maze pattern at the surface. The branching pattern of the maze depends on the crystal structure of the magnet and the available easy axes. The maze pattern consists of regions of different brightness according to the interaction with the magnetic tip during the scanning process; 1- The main maze: imaged as dark due to the reverse of the magnetization of the tip during scanning by the stray fields of the main domains each time when passing from one domain to a neighbouring domain (i.e. at the domain walls). 2- Reverse domains (reverse spikes): which are relatively small regions (1-2 μm) having a small stray field which is insufficient to demagnetize the tip and they are imaged as bright regions which means that they have an opposite magnetization to the main domains. It has been shown [65] that there are fine curved strips of 10-200 nm present at the surface perpendicular to the alignment axis which is believed to be associated with the reduction of the magnetostatic energy close to the specimen surface. The MFM image of this fine structure (Figure 2.11) shows that they have different grey shades which means that the magnetostatic interaction between them and the tip was nonperturbing and they are located at different depths.

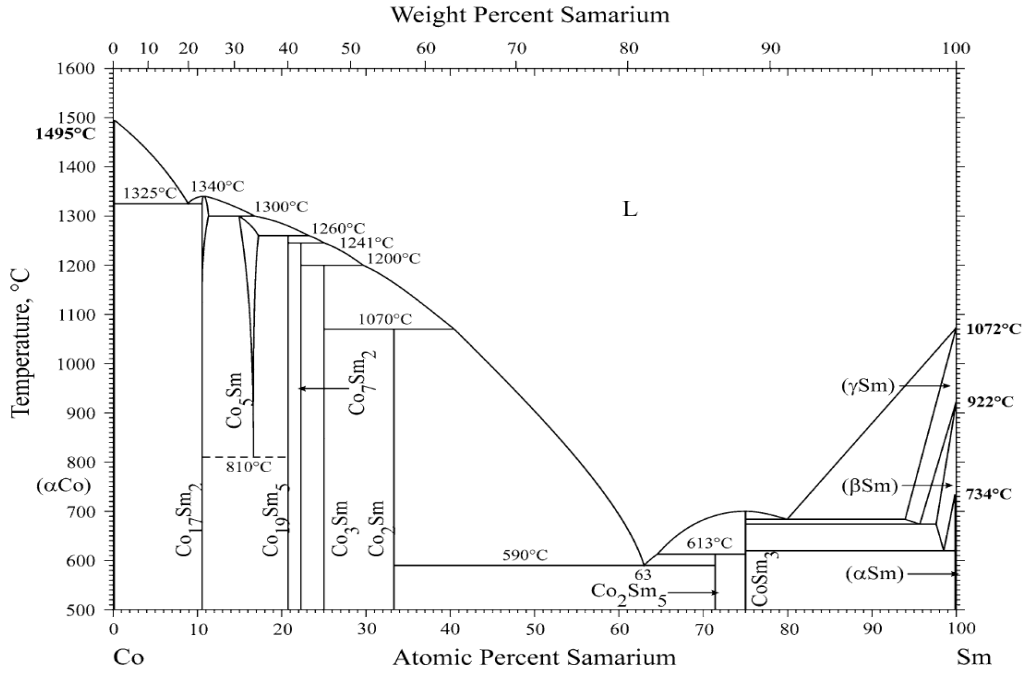

Figure 2.8: Sm-Co phase diagram [61].

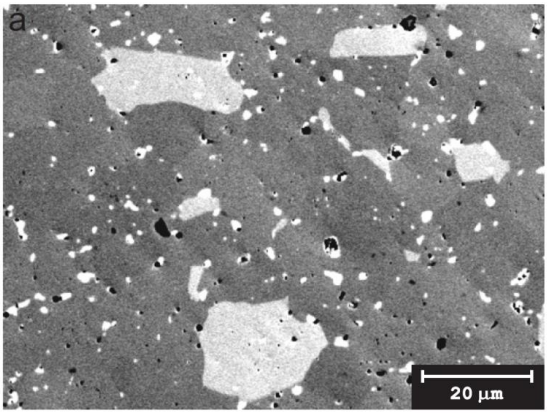

Figure 2.9: BSE image of a sintered $SmCo_5$ magnet [64].

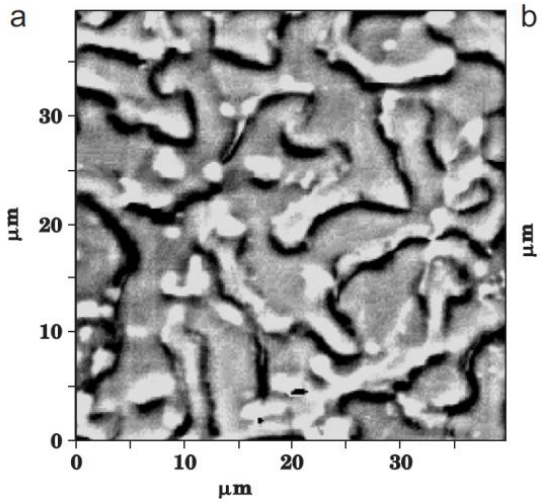

Figure 2.10: MFM image of a sintered $SmCo_5$ magnet (tip-specimen separation is 350 nm) [64].

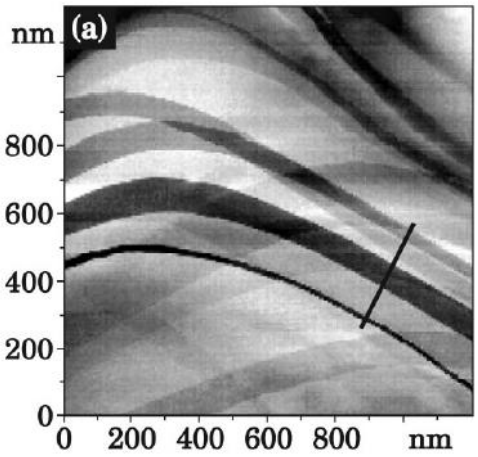

Figure 2.11: High resolution MFM image of the fine strips in a sintered $SmCo_5$ magnet (tip-specimen separation is 50 nm) [65].

2.3.1.2 Effects of process parameters

2.3.1.2.1 The effect of the sintering temperature

Das [66] studied the influence of the sintering temperature on the magnetic properties of $SmCo_5$ having about 37.1 wt.% Sm. Table 2.2 shows the magnetic properties for the magnets sintered at different temperatures from 1102 °C to 1132 °C. At 1102 °C or lower there was poor shrinkage during sintering and the magnetic properties were very low. At 1132 °C, deterioration of the magnetic properties was observed. It is shown that a small change in the sintering temperature, as low as 4 °C, would have a great influence on the properties. All the samples showed the presence of $SmCo_5$ and Sm_2Co_7 phases, and increasing the temperature of the sintering has the effect of increasing the grain size for $SmCo_5$ phase which reduces the coercivity value. Talijan et al. [67] studied the influence of the sintering regime on the stability of the $SmCo_5$ by measuring the intensity of its diffraction peaks. They mentioned that for sintering at 1100 °C, the produced samples have low mechanical properties while a thick oxidised zone is observed when sintering at 1180 °C, which has the effect of deteriorating the magnetic properties, consistent with the former. Note: the exact required temperature can also vary from one furnace to another, as there is usually an offset from the applied temperature and this has to be taken into consideration.

2.3.1.2.2 The effect of the heating rate of the sintering process

de Campos et al. [68] studied the relation between the microstructure of $SmCo_5$ and the resultant B_r. They showed that decreasing of the heating rate during sintering from 75 °C/min to 10 °C/min has the effect of increasing the degree of particles alignment and consequently the increase of the densification and the B_r of the magnet. The grain size from the two heating rates experiments was more or less the same, which is about 6 μm to 7 μm. Another reason for increasing the B_r at a lower heating rate may be caused by the oxidation of Sm_2Co_7 and the formation of $SmCo_5$ and oxides, where increasing the ratio of $SmCo_5$ has the effect of increasing the B_r. Oxygen fraction was measured to be 0.039 and the Sm_2Co_7 fraction as 0.060 for the sample heated at a rate of 10 °C/min in comparison to 0.028 and 0.080, respectively, for the sample heated at a rate of 75 °C/min.

Table 2.2: The effect of the sintering temperature on the magnetic properties of $SmCo_5$ [66].

Sintering Temp. (°C)	B_r (kG - T)	$_iH_c$ (kOe - kA/m)	$_bH_c$ (kOe - kA/m)	$(BH)_{max}$ (MGOe - kJ/m^3)
1102	6.0 - 0.60	3.00 - 234	2.8 - 223	6.50 - 51.7
1107	7.7 - 0.77	27.5 - 2188	7.6 - 605	15.0 – 119
1111	7.7 - 0.77	22.5 - 1790	7.4 - 589	14.4 – 115
1116	7.9 - 0.79	30.0 - 2387	7.1 - 565	15.1 – 120
1120	7.8 - 0.78	24.0 - 1910	7.1 - 629	14.8 – 118
1124	8.1 - 0.81	19.5 - 1552	6.9 - 549	15.1 – 120
1132	8.4 - 0.84	1.60 - 128	1.6 - 128	10.0 – 78.0

2.3.1.2.3 The effect of Sm content

de Campos et al. [68] showed that hyperstoichiometric Sm content would have the effect of increasing the Sm_2Co_7 volume fraction and thus a decrease in the B_r value. Figure 2.12 shows the effect of increasing the volume fraction of the Sm_2Co_7 phase on lowering the B_r for two samples sintered at 1130 °C and 1150 °C. It was also observed that the percentage of pores in the sample increases with increasing Sm content which is accompanied by a decrease in the density and B_r. It was indicated that in addition to the effect of decreasing

the density and the magnetic phases ratio with increasing the porosity content, pores sites also introduce a demagnetizing field in the magnet with a further negative effect on the B_r value. On the other hand, Martin et al. [69] and Gessinger et al. [70] showed that hyperstoichiometric Sm content is required to obtain high coercivity.

Kumar [71] mentioned that a slightly hypostoichiometric Sm contents have the effect of increasing the B_r. However, precipitation of Sm_2Co_{17} might occur, which has the effect of vast deterioration of the coercivity. In the industry, it is usually preferred to work with hyperstoichiometric Sm content to avoid any contamination of the Sm_2Co_{17} phase.

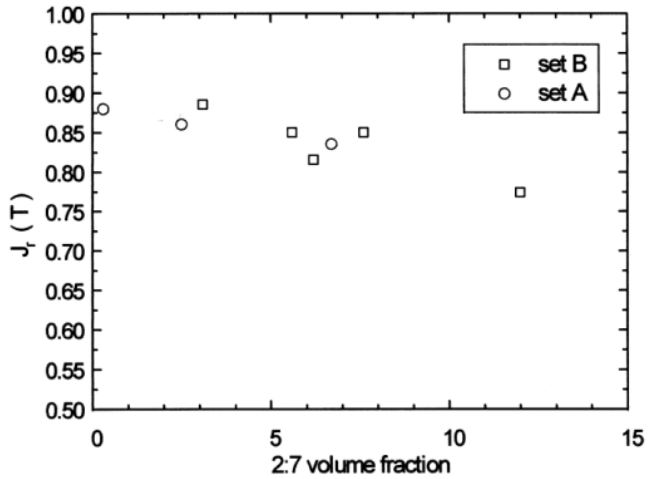

Figure 2.12: Remanence (J_r) vs. volume fraction of the Sm_2Co_7 (2:7) phase. Set A (sintered at 1130 °C), set B (sintered at 1150 °C) [68]. Note B_r here is represented as J_r.

2.3.1.2.4 The effect of the heat treatment regime

The optimization of the heat treatment regime is crucial in achieving a high coercivity value. de Campos et al. [72] showed that the post heat treatment of sintered samples at 850-900 °C results in increasing the $_iH_c$ of $SmCo_5$ from 0.1-0.5 T to 2.5-3 T due to the elimination of defects at the atomic level. Transmission electron microscopy (TEM) image (Figure 2.13) showed that there was no second phase of Sm_2Co_7 precipitated at the grain boundaries of the $SmCo_5$ phase which was believed before to be the reason for increasing the coercivity upon heat treatment at 850-880 °C [73]. They showed that heat treatment at 750 °C is not sufficient for coercivity enhancement. On the other hand, Rabenberg [74] has mentioned that $SmCo_5$ can be transformed to Sm_2Co_{17} by the replacement of Sm atom with a pair of Co atoms at every third position in the lattice. By replacement of Co atom with Sm atom in the mixed plane for every third layer of the $SmCo_5$ structure, Sm_2Co_7 phase can be generated. He showed that $SmCo_5$ phase decomposes to Sm_2Co_{17} and Sm_2Co_7 phase by the eutectoid reaction when heat treated below 750 °C for a long time. On the contrary, the former showed that even 25 days of heat treatment at 750 °C was not sufficient for the phase transformation to occur and there was no evidence of the eutectoid decomposition of $SmCo_5$. However, it was shown that a change in the lattice parameters of the $SmCo_5$ phase has occurred due to the treatment and they suggested that $SmCo_5$ converted to $SmCo_{5+x}$ and $SmCo_{5-x}$ giving Sm or Co rich clusters, which has the effect of decreasing the coercivity. The decrease in coercivity after heat treatment at 750 °C was previously believed to happen due to the formation of the Sm_2Co_{17} phase. It was mentioned that the occurrence of Sm_2Co_{17} phase in some samples may be due to the oxidation of the $SmCo_5$ phase to Sm_2O_3 and Sm_2Co_{17} and not due to the eutectoid decomposition.

den Broeder et al. [75] studied the relation between the coercive force and the microstructure of $SmCo_5$ magnets by the observation of the magnetic domains using polar Kerr effect after heat treatment. Table 2.3 shows the coercivity force value and its mechanism for different samples which were heat treated at different temperatures. Heat treatment at 700 ^oC enhances the easy nucleation of reverse domain and the coercivity for these samples is determined mainly by the pinning of domain walls at the grain boundaries. Heat treatment at 900 ^oC results in difficult nucleation of reverse domains and strong pinning of domain walls by the grain boundaries and consequently high coercivity. Increasing the heat treatment to 1120 ^oC has the effect of weakening the pinning of the domain walls and the coercivity for this sample depends mainly on the difficult nucleation of reverse domains and it shows a moderate value. The nucleation of reverse domains was concluded to depend on the precipitation of Sm_2Co_{17} which can serve as sites for the nucleation reverse. They mentioned that the pinning strength upon the heat treatment temperature is due to various aspects, suh as chemical gradient, local disorder and segregation of solute impurities.

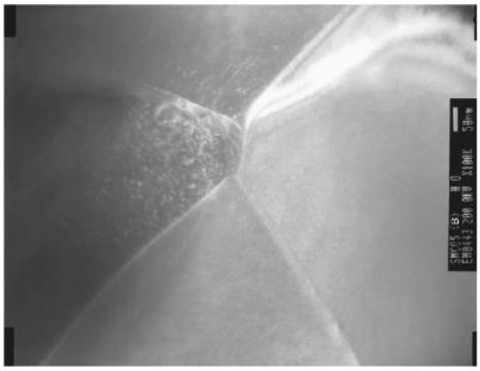

Figure 2.13: TEM microstructure for $SmCo_5$ at the grain boundaries [72].

Table 2.3. Coercivity and its mechanism for $SmCo_5$ heat treated at different temperatures [75].

Heat treatment (^oC)	700 After quenching from 1120	700 After quenching from 900	900	1120
Coercive force	Very low	Intermediate	High	Low
Nucleation	Easy	Easy	Difficult	Difficult
Pinning at grain boundaries	Weak	Moderate	Strong	Weak

2.3.2 Sm_2Co_{17}

Sm_2Co_{17} can exist in one of two different symmetries, i.e. hexagonal and rhombohedral with a space group of P63/mmc and R$\bar{3}$m, respectively, by a substitution of each third REE atom in the basal plane by a pair of Co atoms in the $SmCo_5$ crystal structure. Figure 2.14 shows the Th_2Zn_{17} rhombohedral crystal structure [25]. Sm_2Co_{17} shows low K of 4.2 MJ/m^3 but relatively high $_iH_c$ of 450-1300 kA/m. The B_r value of Sm_2Co_{17} is in the range of 0.9 T to 1.2 T. This phase shows the highest known T_c of 850 ^oC and the lowest β of -0.3 %/^oC and α of -0.03 %/^oC among other REE-permanent magnets [25], [28], [29].

Different additives, such as Fe, Cu and Zr, are usually added to Sm_2Co_{17} for further improvement of T_c, temperature coefficient and magnetic properties. The $(BH)_{max}$ of Sm_2Co_{17} magnets is 150-280 kJ/m^3. In the magnets industry, two types of Sm_2Co_{17} can be found, traditional and novel. Novel Sm_2Co_{17} can service at a higher temperature than traditional Sm_2Co_{17}. The main difference between the two types is the Sm and Fe contents which modify the microstructure and the microchemistry.

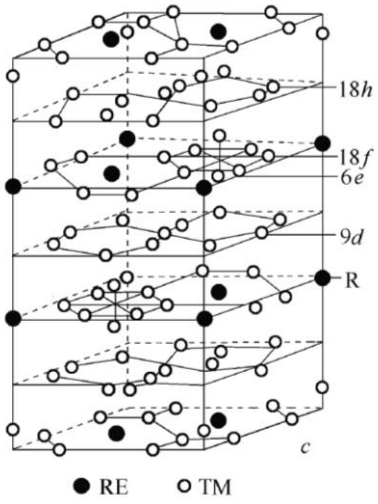

Figure 2.14: The Th_2Zn_{17} crystal structure of Sm_2Co_{17} [25].

2.3.2.1 Structure and magnetic properties evolution

Okabe et al. [76] studied the microstructures and magnetic domain structures of sintered Sm_2Co_{17} with the chemical composition of $Sm(Co_{0.720}Fe_{0.200}Cu_{0.055}Zr_{0.025})_{7.5}$. They used four samples prepared via different regimes. Sample 1 was sintered at 1478 K (~1205 ^{o}C) for 2 h, solution treated at 1363 K (~1090 ^{o}C) for 1 h and then quenched. Sample 2 was obtained by heating the sample 1 to 1093 K (~820 ^{o}C) at a rate of 6.83 K/min and rapidly quenched. Sample 3 was obtained by heating the sample 1 to 1093 K at a rate of 6.83 K/min, isothermally aged at 1093 K for 6 h and rapidly quenched. Sample 4 was produced by heating the sample 1 to 1093 K at a rate of 6.83 K/min, isothermally aged at 1093 K for 6 h, cooled to 643 K (~370 ^{o}C) at a cooling rate of 0.5 K/min (step aged) and then quenched to room temperature. Figure 2.15 shows that the coercivity and the maximum energy product increase drastically for sample 4 (after step aging). Figure 2.16 shows the bright field TEM image and electron diffraction patterns for sample 2 and sample 4. Both samples show a cellular structure of the Sm_2Co_{17} rhombohedral (2:17 R) phase as the cell interiors, mainly consist of $Sm_2(Co, Fe)_{17}$ with Th_2Zn_{17} type structure and $SmCo_5$ hexagonal (1:5 H) phase at the boundaries, composed of $Sm(Co, Cu)_5$ with $CaCu_5$ type structure. A third phase of thin planar plates, which is rich in Zr (Z or lamellar phase), is perpendicular to the c axis and it is composed of $Zr(Co, Fe)_3$ with a Be_3Nb structure. It can be observed that step aging results in an increase in the cell size without a change of the cellular and crystal structures of the two main phases; 2:17 R and 1:5 H. Figure 2.17 shows the scanning transmission electron microscope (STEM) images and the EDX elemental mapping of sample 3 and 4. It is shown that Z phase and 1:5 H phase have a lower Fe content, Z phase has a higher Zr content and 1:5 H phase has a higher Cu content. It can also be seen that the step aging leads to an increase in the segregation of the Cu atoms to the 1:5 H boundaries. Lorentz microscopy was used for the 4 samples (Figure 2.18) in the demagnetized state. The domain walls for the step aged sample show a zig-zag structure along the cell boundary and so it has been concluded that the increase in coercivity for

sample 4 is due to increasing the Cu content in the cell boundary by step aging, which in turn has the effect of increasing the pinning behaviour of the 1:5 H phase.

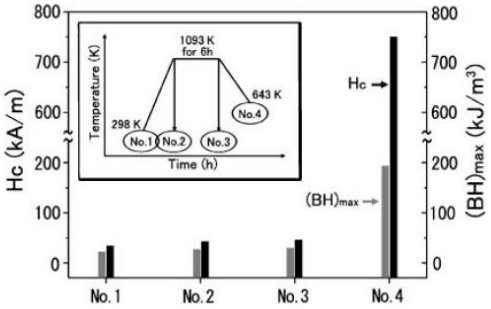

Figure 2.15: The effect of heat treatment on the magnetic properties of the four samples of $Sm(Co_{0.720}Fe_{0.200}Cu_{0.055}Zr_{0.025})_{7.5}$ [76]. Note ${}_bH_c$ is represented as H_c.

Zhang et al. [77] used sintered magnets of composition of $Sm(Co_{bal}Cu_{0.06}Fe_{0.015}Zr_{0.027})_{6.4}$ to study the microstructure, microchemistry evaluation and coercivity with heat treatment. The sample was heat treated by homogenization at 1160-1190 °C, step aged at 700-850 °C for 5 min to 24 h and then quenched to room temperature directly or after slow cooling to 400-700 °C at the rate of 0.5-1 °C/min. After homogenization, the sample has a featureless 2:17 hexagonal (2:17 H) cell interior. Isothermal aging for 5-30 min results in the precipitation of the 1:5 H phase and the formation of the cellular structure. After 2 h of aging, a uniform lamellar (Z phase) and cellular structure are formed with increasing in the cell size and density of the lamellar phase with time up to 24 h (Figure 2.19). Figure 2.20 shows the effect of isothermal aging with time. Fe atoms segregate from the cell boundaries to the interior with a contrary behaviour for the Cu atoms. Cu content increases drastically in the cell boundary by subsequent slow cooling to 400 °C. Finally, the 2:17 R cells are richer in Co and Fe while poorer in Cu and Zr, 1:5 H phase is richer in Cu and poorer in Fe and Zr and the lamellar phase is richer in Zr and poorer in Fe. They mentioned that the slow cooling process is mandatory for the segregation of Cu atoms to the cell boundaries in high amount and consequently increases the coercivity (Figure 2.21). Increasing the aging temperature from 700 °C to 850 °C has the effect of increasing the boundary width, and lamellar density which leads to increase in coercivity. It was mentioned that irrespective of the aging temperature, a zig-zag structure at the domain walls is formed due to the increase in the Cu content. The Cu content is responsible for the wall pinning behaviour. Gopalan et al. [78] reported that the presence of a large gradient of Cu in the 1:5 H phase has the effect of enhancing the coercivity and that a uniform Cu distribution would lead to a sample with low coercivity.

2.3.2.2 The relation between Fe, Cu and Zr content and the final properties

2.3.2.2.1 The effect of Fe content

Liu et al. [79] studied the effect of Fe content on the coercivity, B_r and T_c of Sm_2Co_{17} with a chemical composition of $Sm(Co_{bal}Fe_xCu_{0.078}Zr_{0.033})_{8.3}$, where x equals 0, 0.1, 0.17 and 0.244. Figure 2.22 shows the effect of increasing the Fe content on the magnetic properties of the magnets. Sample with x=0.1 has the maximum ${}_iH_c$ of more than 40 kOe (~3183 kA/m). They explained these results as Fe of that content acts as a stabilizer for 2:17 R in the presence of Cu during the aging step and it prevents the formation of Co-Cu solid solution. On the other hand, increasing the Fe content reduces the anisotropy field and T_c. Perkins et al. [80] mentioned that the anisotropy constant decreases from 6.7×10^7 to 4×10^7 erg/cm^3 and the T_C from 1200 K (~927 °C)to 1138 K (~856 °C) by increasing the x from 0 to 0.244 in the $Sm_2(Co_{1-x}Fe_x)_{17}$ alloys. The microstructure studies of samples with

different Fe content showed that the average cell size and the cell size distribution and density of lamellar phase are almost the same.

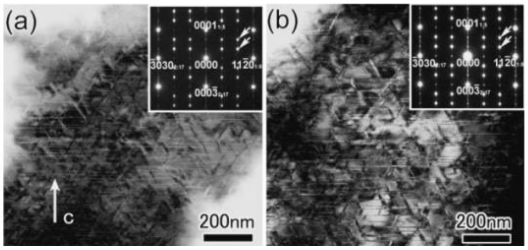

Figure 2.16: (a), (b) Bright-field images and selected-area electron diffraction patterns obtained from specimens 2 and 4, respectively [76]. Sample composition: $Sm(Co_{0.720}Fe_{0.200}Cu_{0.055}Zr_{0.025})_{7.5}$.

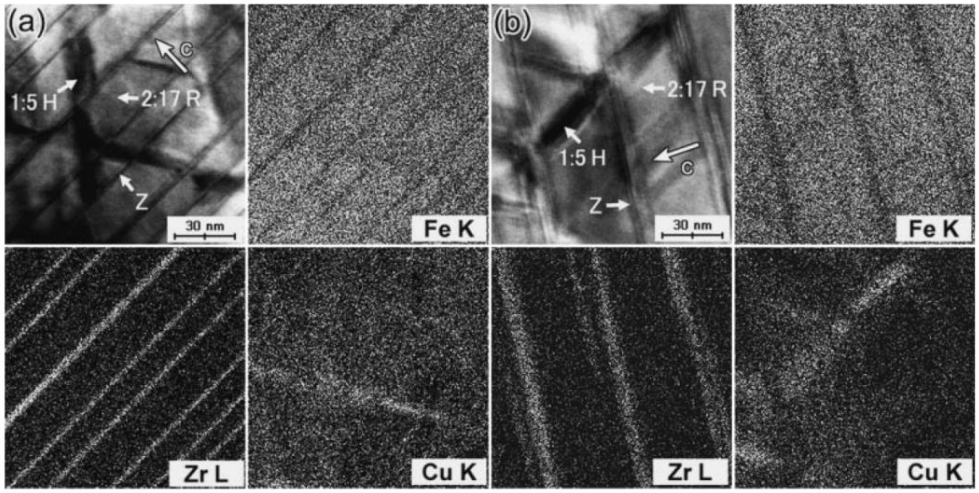

Figure 2.17: STEM images (a, b) and EDX elemental mapping images for samples 3 and 4, respectively [76]. Sample composition: $Sm(Co_{0.720}Fe_{0.200}Cu_{0.055}Zr_{0.025})_{7.5}$.

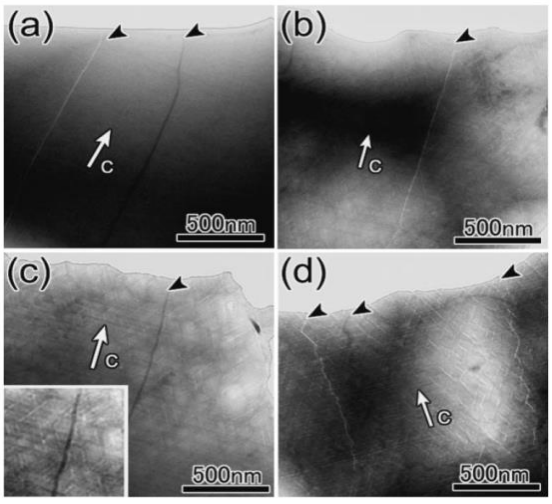

Figure 2.18: (a), (b), (c), (d) Lorentz microscope images for samples 1, 2, 3, and 4, respectively. Sample composition: $Sm(Co_{0.720}Fe_{0.200}Cu_{0.055}Zr_{0.025})_{7.5}$. White and black arrows indicate the c-axes and domain walls, respectively [76].

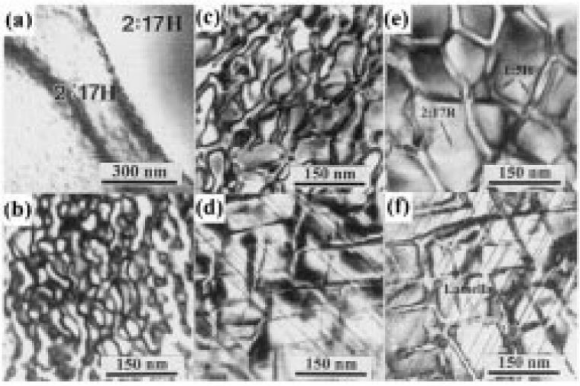

Figure 2.19: Evolution of the TEM microstructure in $Sm(Co_{bal}Cu_{0.06}Fe_{0.015}Zr_{0.027})_{6.4}$ samples: (a) Homogenized at 1180 °C followed by quenching to room temperature; (b) Aged at 830 °C for 15 min followed by quenching to room temperature. (c), (d) Aged at 830 °C for 2h followed by quenching to room temperature, showing the cellular structure and lamella phase superimposed on the cellular structure, respectively. (e), (f) Aged at 830 °C for 24 h followed by quenching to room temperature, showing the cellular structure and lamella phase superimposed on the cellular structure, respectively [77].

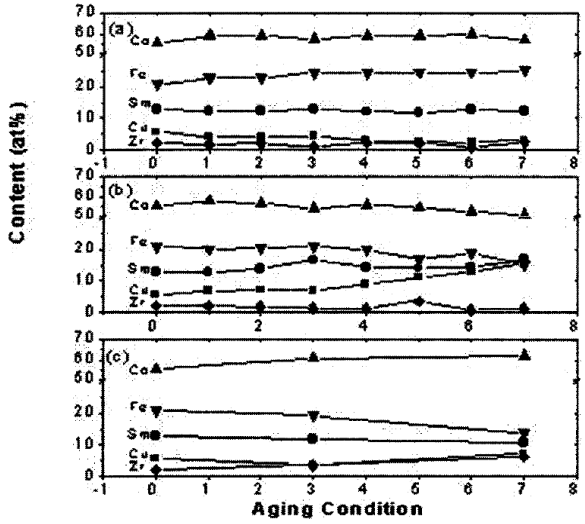

Figure 2.20: Development of microchemistry in $Sm(Co_{bal}Cu_{0.06}Fe_{0.015}Zr_{0.027})_{6.4}$ samples aged at 830 °C: (a) cell interior, (b) cell boundary; (c) lamellar phase. 0, 1, 2 and 3 represent the initial state, 30 min, 2 h and 24 h aging followed by quenching to room temperature, respectively. 4, 5, 6 and 7 represent 24 h aging followed by a subsequent slow cooling to 700 °C, 600 °C, 500 °C and 400 °C, respectively [77].

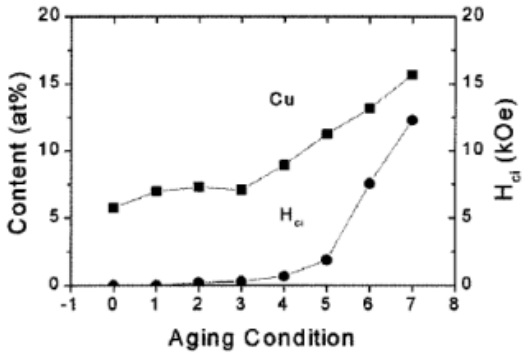

Figure 2.21: Changing of the 1:5 Cu content and coercivity with aging for $Sm(Co_{bal}Cu_{0.06}Fe_{0.015}Zr_{0.027})_{6.4}$. The samples followed the same heat treatment as in Figure 2.15 [77].

2.3.2.2.2 The effect of Cu content

Wang et al. [81] studied the effect of Cu content on the coercivity and domain structure of $Sm(Co_{bal}Fe_{0.1}Cu_xZr_{0.033})_{6.9}$, (x = 0.07, 0.10, 0.13). After sintering, the samples were heat treated by annealing at 1190 °C, aged at 810 °C and then slowly cooled (0.5 °C/min) to 400 °C or 600 °C, and finally quenched to room temperature. Figure 2.23 shows the variation of domain structures and coercivity for the magnets at different temperatures. For the samples with x = 0.07 and the one with x = 0.1, which is quenched from 600 °C, the coercivity shows a relatively direct relation with temperature (abnormal behaviour). The samples which show abnormal temperature dependence have a domain structure of a strip shape which is typical for ferromagnets with easy-axis anisotropy and the Cu content is nearly homogeneous in the 1:5 H phase. The pinning of the domains for those magnets occurs near the interface between 2:17 R cell phase and 1:5 H cell boundary phase. On the other hand, samples with normal coercivity behaviour have narrower and more additional domains. The pinning of those magnets occurs as the domain wall is pinned into the 1:5 H cell boundary phase, where a gradient of Cu content exists.

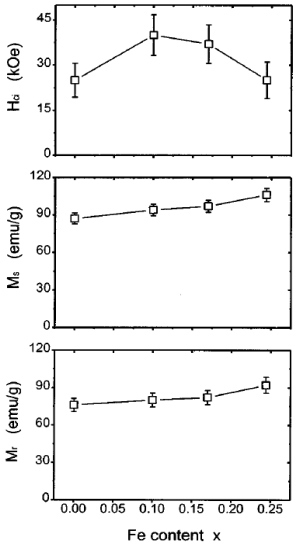

Figure 2.22: Intrinsic coercivity, saturation magnetization (M_s) and remanence for $Sm(Co_{bal}Fe_xCu_{0.078}Zr_{0.033})_{8.3}$ magnets [79]. Note ${}_iH_c$ and B_r are represented as H_{ci} and M_r.

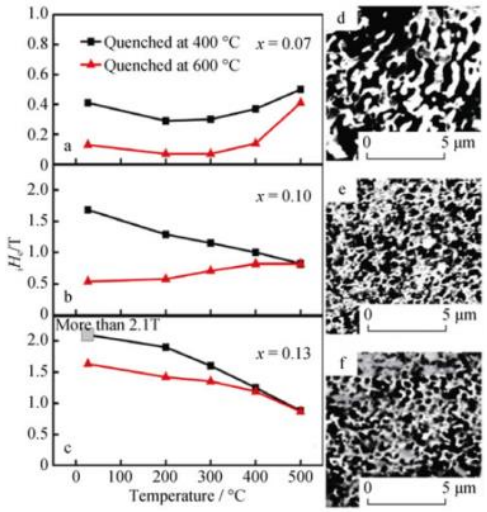

Figure 2.23: ${}_iH_c$ at different temperatures for Sm $(Co_{bal}Fe_{0.1}Cu_xZr_{0.033})_{6.9}$ and the corresponding domain structures for the samples quenched from 400 °C [81].

2.3.2.2.3 The effect of Zr content

Tang et al. [82] used a different concentration content of Zr element to study the variation of the microstructure and magnetic properties of $Sm(Co_{bal}Fe_{0.1}Cu_{0.088}Zr_x)_{8.5}$, x=0–0.1. The variation of the content of the Zr greatly affects the saturation magnetization and coercivity of the produced magnets (Figure 2.24). Zr element is necessary for the formation of the lamellar phase (Figure 2.25). Table 2.4 shows the effect of Zr content on the cell size, thickness of the boundary phase and density of the lamellar phase. Increasing the Zr content above x=0.08 leads to the formation of a considerable amount of $SmCo_3$ and Sm_2Co_7 which is accompanied by a decrease in coercivity. When the Zr content is very low (lower than 0.01), the lamellar phase cannot be observed. Increasing the Zr content further is accompanied by the formation of the lamellar phase which acts as a path for the segregation of the Cu to the boundary phase and enhances the domain wall pinning and coercivity. Therefore, the 2:17 R cell size is shown to decrease with the increase in the Zr content.

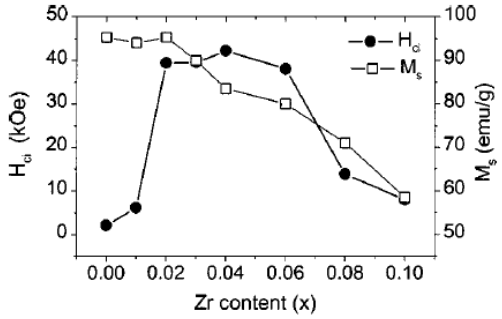

Figure 2.24: Intrinsic coercivity and saturation magnetization of $Sm(Co_{bal}Fe_{0.1}Cu_{0.088}Zr_x)_{8.5}$ [82]. Note ${}_iH_c$ is represented as H_{ci}.

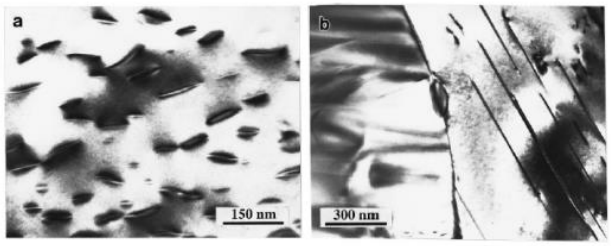

Figure 2.25: TEM micrographs of $Sm(Co_{bal}Fe_{0.1}Cu_{0.088}Zr_x)_{8.5}$ samples with x=0 (left) and 0.1 (right) [82].

Table 2.4: Influence of Zr content on the microstructure of $Sm(Co_{bal}Fe_{0.1}Cu_{0.088}Zr_x)_{8.5}$ samples obtained from the TEM images [82].

X	0	0.01	0.04	0.08	0.10
Cell size (nm)	...	120	100	35	...
Cell boundary's thickness (nm)	...	10.5	11	10	...
Lamellar phase's density (1/nm)	...	0.03	0.061	0.062	...

2.4 HD of Sm-Co Compounds

HD is a size-reduction technique, where the material under investigation breaks into smaller particle sizes due to hydrogen absorption. The mechanism of the hydrogen absorption can be explained as follows; first, hydrogen gas is physically adsorbed on the material's surface. After the application of the required activation energy, the adsorbed hydrogen molecule is broken into hydrogen atoms (chemical adsorption). This is followed by the diffusion of the atoms into the interstitial sites of the material and the formation of the hydrides with the material's phase(s). There are many factors to be considered when performing HD, i.e., the chemical composition and the microstructure of the material, the hydrogen pressure, the temperature, the pressure cycling, and the presence of an external effect as rotation, vibration, or magnetic field. Different phases in the material have different affinities to hydrogen absorption, and depending on the distribution and the concentration of the phases with higher affinity for hydrogen absorption in the microstructure of the material, the fracture process due to HD can be intergranular, transgranular, and/or due to ductile failure [83]. (3)

HD is a well-defined technique for the preparation of Nd-Fe-B magnets and it has been applied industrially for more than 20 years [84], [85]. The as-cast alloy reacts with hydrogen under atmospheric pressure to form smaller friable particle size powder which is then jet milled to produce powder suitable for the production of the magnets. It was calculated that when using HD on the as-cast alloys before the milling step, there a 25% cost reduction is achieved in comparison with milling without performing HD on the as-cast alloys [86]. In comparison with Nd-Fe-B alloys, Sm-Co alloys have shown to have a much higher thermal stability, and more severe conditions of pressures and temperatures are required for the decrepitation or the dissociation of the $SmCo_5$ and Sm_2Co_{17} phases [87]. As a result, hydrogen gas is not industrially used either for the preparation nor for the recycling of Sm-Co compounds (3). The previously reported literature on the HD on Sm-Co compounds will be described in order to give a background for the work performed.

2.4.1 $SmCo_5$

2.4.1.1 HD of $SmCo_5$

Shortly after Strnat and his colleagues discovered the magnetocrystalline anisotropy in Sm-Co compounds [13], Zijlstra et al. [88] studied the reaction of hydrogen gas with $SmCo_5$. They showed that $SmCo_5$ absorbs about 2.5 mol of hydrogen at a pressure of 20 atm at room temperature in an exothermic reaction. They mentioned that upon hydrogen absorption, the $SmCo_5$ hexagonal structure is converted to an orthorhombic structure. This causes the disintegration of the starting material (decrepitation). The original hexagonal structure was shown to be recovered by desorbing the previously absorbed hydrogen, simply by relieving the hydrogen pressure (note: time is an important factor for the hydrogen relieving, 24 h is recommended to insure complete desorption). One year later, van Vucht et al. [89] and Kuijpers and van Mal [90] showed that the final hydrogen concentration in the material depends on the pressure applied and the reaction time, where saturation of the $SmCo_5$ with hydrogen to form $SmCo_5H_3$ was possible by reacting crushed 50 μm particle sizes of $SmCo_5$ alloy with hydrogen gas of 100 bar for 2 days. Li et al. [91] compared between the phase transformation for the hydrogenation and nitridation of $SmCo_5$ alloys. In contrast to hydrogenation, upon nitridation, the $SmCo_5$ alloy was converted into an amorphous structure. (3)

2.4.1.1.1 The effects of temperature and chemical composition on the HD of $SmCo_5$

It was shown [91] that increasing the temperature generally has a negative effect on the hydrogen absorption and the decrepitation reaction for the $SmCo_5$ alloys, where, for example, a pressure of 45 bar led to the absorption of a very low fraction of hydrogen of less than 0.5 mol at 100 ^{o}C, in comparison to that at room temperature. Kuijpers and van Mal [90] studied the absorption–desorption isotherm of the $SmCo_5$-H systems (after activation under 50–60 atm of hydrogen) at different temperatures up to 80 ^{o}C. Increasing

the applied temperature results in increasing the pressure required for the hydrogen absorption. Plateaux were observed in the isotherms which confirm the existence of a two-phase region upon hydrogen absorption. Those two phases were identified to be of a hexagonal solid-solution alpha phase, and a crystalline hydride orthorhombic beta phase with a higher hydrogen content. This behaviour is in contrast to the hydrides of Sm_2Fe_{17}-H_x, $Nd_2Fe_{14}B$-H_x, and Sm_2Co_{17}-H_x ($0 \leq x \leq 5$), which are only solid-solution interstitial hydrides with no defined plateau pressure [90]. It is also shown that the difference in the pressures between absorption and desorption plateaux increases at higher temperatures. (3)

Raichlen and Doremus [92] studied the effects of the concentrations of Sm and Co on the hydrogen absorption. They used different compositions of $SmCo_5$ alloys having a Sm content in the range of 15.1–18 at.% (31.1–35.9 wt.%). The alloys were crushed and activated under 100 atm of hydrogen for 2 days. They showed that the alloys with a Sm content of ≤ 15.1 at.% (31.1 wt.%) do not form hydrides under the mentioned pressures and the Sm content has to be higher than 31.1 wt.% for the material to absorb hydrogen. This phenomenon was explained as being due to the presence of traces of the non-hydriding Sm_2Co_{17} in the alloys with a low Sm content, which causes mechanical strains which prevent the volumetric expansion of the $SmCo_5$ phase. It was calculated that the $SmCo_5$ phase formed a hydride of composition of $SmCo_5H_{2.6}$ for all the alloys with Sm content of > 31.1 wt.%. (3)

Harris [83] observed the same effect of Sm content increasing the enhancement of the hydrogen absorption and decrepitation. He used two alloys of compositions of $SmCo_5$ and $SmCo_{4.8}$. The microstructure of $SmCo_{4.8}$ has a fine microstructure with intergranular Sm_2Co_7, whereas $SmCo_5$ was found to have a coarser microstructure. $SmCo_{4.8}$ showed to have greater affinity for the decrepitation and results in smaller particle size after decrepitation in comparison with decrepitation of $SmCo_5$ under the same hydrogen pressure. It was found that the Sm_2Co_7 phase tends to form hydride at lower pressures than the one required for the $SmCo_5$ phase. The same author therefore explained that, for the $SmCo_{4.8}$, the hydrogen absorption starts with intergranular absorption of the Sm_2Co_7, which is in addition to forming partial expansion in the material microstructure due to the hydrogen absorption itself, facilitates the hydrogen absorption of the $SmCo_5$, and plays the role of reducing the hydrogen pressure required for the decrepitation. Therefore, he proposed the process for $SmCo_5$ compounds' decrepitation to be intragranular followed by transgranular cracking. (3)

Apostolov et al. [93] studied the hydrogen reaction of the Sm_2Co_7 compounds. They showed that Sm_2Co_7 absorbs hydrogen easily under a pressure of 1 bar, 70 °C. They mentioned that, although the hydrogen absorption causes lattice expansions, there are no structural changes upon hydrogen absorption. Cao et al. [94] studied the lattice expansions of Sm_2Co_7 alloys upon hydrogen absorption. They calculated the pressure-a composition isotherm for the Sm_2Co_7-H between 75 °C and 180 °C. Besides the alpha solid-solution phase, two distinguishable beta and gamma phases were formed. Beta phase with composition of Sm_2Co_7H (0.33–0.43 wt.% H_2) with lattice expansion in the c direction and gamma phase with a composition of Sm_2Co_7H (0.51–0.67 wt.% H_2) with lattice expansion in the a direction. Christodoulou et al. [95] studied the reaction of Sm metal with hydrogen. They showed that bulk and powder Sm metal react exothermally with hydrogen under 1.47 bar and 300–525 °C, and the high temperature was required for the gas to penetrate into the oxide layer on the surface of the metal. Upon cooling to room temperature, the rhombohedral Sm metal after hydrogen absorption is converted into a face-centered cubic SmH_{2+x} ($0 \leq x \leq 0.63$) symmetry, where the hydrogen occupies the octahedral and the tetrahedral sites in the Sm element. These studies confirm Harris' [83] hypothesis that Sm and Sm-rich phases absorb hydrogen gas at a lower pressure than the $SmCo_5$ and their presence in the alloy's microstructure will reduce the hydrogen pressure required to initiate the absorption reaction. (3)

2.4.1.2 Polymer-bonded magnets made of the decrepitated powder

Harris [83] compared between the magnetic properties of polymer-bonded magnets made out of milled powder and HD powder produced under a pressure of 50–700 bar. The HD powder was passed through a rotating vane before mixing with the bonding material. The magnetic properties for the bonded magnets prepared from the HD powder were generally inferior to the ones made out of the milled powder; he hypothesized that this is mainly due to the higher reactivity of the HD powder and thus the higher affinity for oxidation. He showed the effect of increasing the applied hydrogen pressure on the B_r and ${}_iH_c$ of the bonded magnets. It was shown that the ${}_iH_c$ increases with the increasing pressure of hydrogen, where ${}_iH_c$ value of 970 kA/m was obtained at 700 bar, whereas the B_r first decreases at a pressure range of around 50–150 bar and then increases with no further improvement beyond 330 bar (about 0.48 T). He also showed that superior magnetic properties were obtained for the magnets made from decrepitated $SmCo_{4.8}$ in comparison with $SmCo_5$, as the particle size from the first alloy is smaller with a more uniform distribution. (3)

2.4.1.3 Sintered magnets made of the decrepitated powder

Harris et al. [96] in 2011 filed a patent for the recycling of sintered magnets, among different magnets, they reported the decrepitation of sintered $SmCo_5$ under low hydrogen pressure. However, they did not report the use of the decrepitated powder for the production of new magnets. (3)

2.4.2 Sm_2Co_{17}

2.4.2.1 HD of Sm_2Co_{17}

Evans et al. [97] used 0.2 g of crushed Sm_2Co_{17} binary alloy (without Fe, Cu, and Zr addition) to study the hydrogen absorption–desorption isotherm at 200 ^oC, 12 atm. Only the alpha phase has been formed under the latter conditions with lattice parameters' expansion, where it was concluded that higher pressures of hydrogen are required for the formation of the beta hydrides. Similar to the $SmCo_5$ alloys, they observed that there is no significant difference between the hydrogen absorption and desorption isotherms. They mentioned that the Sm_2Co_{17} alloys have a lower affinity for hydrogen absorption in comparison with $SmCo_5$, where they showed that it was not possible to perform decrepitation for such alloys at room temperature even under higher pressures and at least a temperature of 120 ^oC was required to observe hydrogen absorption and the weight change. (3)

The magnetic properties of the Sm-Co magnets have been shown to increase with the addition of Fe, Cu, and Zr [98]. Harris [83] and Kianvash and Harris [99] used three different chemical compositions of the as-cast alloys: $Sm(Co_{0.671}Cu_{0.080}Fe_{0.222}Zr_{0.025})_{8.92}$, $Sm(Co_{0.674}Cu_{0.096}Fe_{0.216}Zr_{0.014})_{7.55}$, and $Sm(Co_{0.660}Cu_{0.100}Fe_{0.220}Zr_{0.020})_{7.37}$ to study the hydrogen absorption behaviour. Similar to the Sm_2Co_{17} without the Co, Fe, and Zr addition. It was mentioned that hydrogen absorption for those compositions was not possible at room temperature. They used decrepitation conditions of 200 bar and 200 ^oC. The hydrogen-absorption mechanism was shown to depend on the composition of the used alloy. The decrepitation reaction for the first and third alloys was mainly the intergranular fracture, while the alloy with intermediate Sm content was shown to have a ductile failure in addition to the intergranular absorption, Figure 2.26. All the powders were also shown to have some transgranular cracks after hydrogenation. In contrast to $SmCo_5$, the hydride form of the powder remained, even after exposing the decrepitated powder to air. (3)

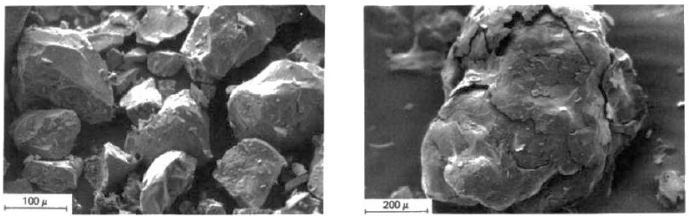

Figure 2.26: HD powder from Sm_2Co_{17} of different chemical compositions; left: alloy A and C, and right: alloy B [83].

2.4.2.1.1 The effects of temperature, chemical composition, and annealing on the HD of Sm_2Co_{17}

Li et al. [100] studied the effects of Sm content and temperature on the hydrogen absorption of five different arc-melted Sm_2Co_{17} alloys with compositions of $Sm(Co_{0.65}$-$Fe_{0.25}Cu_{0.08}Zr_{0.02})_z$, where Z = 5.0, 6.1, 7.4, 9.3, 12; (A, B, C, D, E, respectively). Under conditions of 10 bar and room temperature, only the three samples with the highest Sm content (A, B, and C) were shown to absorb hydrogen. The hydrogen uptake was found to depend on the Sm content, where after saturation for 20 h, the amounts of the absorbed hydrogen were 0.75 wt.%, 0.51 wt.%, and 0.3 wt.% for the A, B, and C samples, respectively. (3)

Those authors also showed the effects of temperature on the HD for the previously mentioned samples at a pressure range of 1–1.24 bar, using a powder of 0.5 mm particle size. As expected, they showed that the initial hydrogenation temperature decreases with the increasing content of Sm, which is also accompanied with the increasing temperature range of the hydrogenation. For example, ingot A was shown to absorb hydrogen at the range of 185–288 °C, while for the ingot E the temperature range was 235–297 °C. (3)

Li et al. [101] used the powders with chemical compositions of $Sm(Co_{bal}Fe_xCu_{0.053}Zr_{0.02})_{7.84}$, (x = 0.2,0.3,0.4,0.5) to study the effects of Fe on hydrogenation and dehydrogenation under a low pressure of 4 bar, and at room temperature. Those authors showed, for the alloy with x = 0.2, it was not possible for the sample to absorb any significant amount of hydrogen at the applied pressure. In contrast, the powder with Fe contents of x = 0.3, 0.4, and 0.5 was shown to absorb about 0.15 wt.% of hydrogen. They attributed the enhancement of the hydrogen absorption upon increasing the Fe content to two reasons; (1) Fe has a larger atomic radius than cobalt which will result in expanding the 2:17 lattice which enhances the hydrogen diffusion. (2) Fe has a lower electronegativity in comparison with cobalt and so, the electronegativity difference for Fe–H is higher than Co–H with decreasing the activation energy required for the Fe–H bond. The previous conclusion of Fe enhancing the hydrogen absorption is also confirmed by Nakamura et al. [102] as they showed that Sm_2Fe_{17} alloys absorb hydrogen gas very easily at a temperature of 250 °C under an atmospheric pressure of hydrogen. (3)

Following the previous study by Li et al. [101], Ming et al. [103] studied the effects of Fe content and annealing treatment on hydrogenation behaviour of $Sm(Co_{bal}Fe_xCu_{0.068}Zr_{0.034})_{7.33}$, (x = 0.237, 0.251, 0.265) as-cast alloys at 3 bar, and at room temperature. Only the alloys with Fe contents of x = 0.251 and 0.265 were shown to absorb hydrogen. Studying the microstructure has permitted them to reach another conclusion for the improvement of the hydrogen absorption upon increasing the Fe content. The authors showed that increasing the Fe content increases the distribution and refinement of the easily decrepitated $SmCo_5$ and Sm_2Co_7 phases, which have the effect of enhancing the decrepitation affinity. To study the effect of the heat treatment on the hydrogen absorption, the three alloys were heat treated at 1190 °C. After the heat treatment, all the alloys with different compositions absorbed hydrogen under the above-mentioned conditions. The amount of hydrogen absorbed in the heat-treated alloys was also shown to increase with the increasing Fe content. They studied the microstructures

after the heat treatment, where it was shown that for the alloy with x = 0.237, in contrast to the other two alloys, there was replacement of some Co atoms by Fe atoms in the 2:17 phase, which was ascribed to be the reason for enabling the hydrogen absorption for the alloy with the lowest Fe content. The previous conclusion was also confirmed by the decrease in the amount of the absorbed hydrogen for the heat-treated alloys with x = 0.251 and 0.265 in comparison with the as-cast alloys without heat treatment. (3)

2.4.2.2 The magnetic properties for the hydrogen-treated Sm_2Co_{17}

The presence of hydrogen in the microstructure of the powder has been shown to be a reason for the drop in the coercivity, but even so, the c axis anisotropy persists, and the powder could still be aligned. The hydrogen in the alloy's microstructure can be easily removed by heating the powder at 200 °C before further processing. In order to compare between the magnetic properties of the hydrogen decrepitated powder, Isnard et al. [104] in 1992 used four different compositions of $Sm(Co_{0.671}Cu_{0.080}Fe_{0.222}Zr_{0.025})_{8.92}$, $Sm(Co_{0.66}Cu_{0.10}Fe_{0.22}Zr_{0.02})_{7.37}$, $Sm(Co_{0.676}Cu_{0.053}Fe_{0.25}Zr_{0.02})_{7.5}$, and $Sm(Co_{0.65}Cu_{0.05}Fe_{0.28}Zr_{0.02})_{7.67}$ annealed sintered samples to be decrepitated under 10–200 bar; sometimes, heating to 200 °C was necessary. They calculated the hydrogen uptakes for the samples to be in the range of 1.85–2.2 H atoms $f.u.^{-1}$. Increasing the Sm content resulted in increasing the hydrogen uptake. As previously mentioned, the coercivity after decrepitation has decreased in comparison with the annealed samples, but after degassing and heat treatment, coercivity comparable to the annealed ingot was achieved again for the four alloys. (3)

Zakotnik et al. [105], [106] used a gravimetric Hiden Intelligent Gravimetric Analyzer, 0.1 g of sintered $Sm(Co_{0.69}Fe_{0.21}Cu_{0.068}Zr_{0.019})_{7.49}$ under a pressure of 10 bar, at room temperature to study the hydrogen absorption. They showed that hydrogen content of 0.23 wt.% was achieved at around 10 bar, and 48 h were required to reach saturation with the production of flake-like particles due to the onion skin fracture. The HD powders were shown to have a lower B_r of 14% in comparison with the freshly prepared powders. They studied the effect of the degassing temperature on the magnetic properties of the powders. The sample recovered its original B_r after degassing under vacuum at a temperature range of 150–300 °C, with a complete restoration of the 2:17 phase, where increasing the degassing temperature had the result of decreasing the B_r value. (3)

2.4.2.3 Sintered and polymer-bonded magnets of the decrepitated powder

Evans et al. [97] compared between the magnetic properties of polymer-bonded magnets prepared using the powders produced via the milling route and the HD route. The composition of the used alloy was $Sm(Co_{0.671}Cu_{0.080}Fe_{0.222}Zr_{0.025})_{8.92}$. The decrepitation reaction was performed under a pressure of 300 bar to produce a particle size of 400 μm. Then, the decrepitated powder was slightly smeared to 100 μm and degassed to remove the hydrogen gas from the powder's microstructure. For the milling route, the alloy was milled to an average particle size of 40 μm. Even then, the HD powders have a higher particle size than the milled powder, the bonded magnets prepared from the HD powder were shown to have better demagnetization loop shapes, higher $_iH_c$, and improved elevated temperature stability in comparison to the ones from the milled powders. This was attributed to the intergranular fracture for the HD powder, and to the fact that the particles are single crystals with lower mechanical deformation, and so the HD particles are more coherent with less strain. (3)

Taking the previous explanation into consideration, it is obvious that the chemical composition and the microstructure of the used alloy will affect the magnetic properties of the produced magnet as different microstructures will produce powders with different morphologies. They showed that, for the bonded magnets from the alloy with a composition of $Sm(Co_{0.674}Cu_{0.096}Fe_{0.216}Zr_{0.014})_{7.55}$, the magnet prepared by the HD powder

has lower magnetic properties in comparison with the magnet prepared by the milled powder. (3)

Kwon et al. [107] used a combination of decrepitation and vibration ball milling for the production of sintered magnets. The $Sm(Co_{0.65}Fe_{0.23}Cu_{0.10}Zr_{0.02})_{7.1}$ alloy was decrepitated at 200 °C, and 20 bars for 2 h which was shown to result in both intergranular and transgranular failures. The decrepitated powder was then milled under nitrogen atmosphere for 3 h. Vacuum desorption for the hydrogen gas from the powder was performed at 300 °C before the sintering step. They used sintering and heat treatment conditions as follows: (1) sintering at 1190 °C for 1 h under an argon gas atmosphere, (2) solution treatment at 1160 °C for 1 h, (3) quenching into liquid argon, (4) isothermally aging at 820 °C from 0 to 35 h, and (5) multiple step aging. The produced magnets were comparable to the Sm_2Co_{17} commercial magnets in terms of the magnetic properties (Table 2.5). (3)

Li et al. [100] used the decrepitated powder from $Sm(Co_{0.65}Fe_{0.25}Cu_{0.08}Zr_{0.02})_z$ after 10 h reaction at 10 bar for the production of sintered magnets. The decrepitated powder was jet milled to a particle size of 4–5 μm before the sintering step. Confirming the previously mentioned results, the produced magnet was shown to have very promising magnetic properties of $B_r = 1.12$ T and $(BH)_{max}$ of 226 kJ/m³. (3)

Table 2.5: Comparison between ${}_iH_c$, B_r and $(BH)_{max}$ for the Sm_2Co_{17} magnets prepared from milled and HD powders.

Magnet manufacturer	${}_iH_c$ (kOe – kA/m)	B_r (kG – T)	$(BH)_{max}$ (MGOe – kJ/m³)
(REC-26)TDK - $Sm(Co_{0.69}Cu_{0.07}Fe_{0.22}Zr_{0.02})_{7.2}$ [108]	~15 – 1194	~9.9 – 0.99	~27 – 215
(R-26H) ShinEstu Chem. $Sm(Co_{0.726}Cu_{0.050}Fe_{0.199}Zr_{0.025})_{7.48}$ [109]	~13.5 – 1074	~10.6 – 0.11	~27 – 215
Kwon et al. [107] work - $Sm(Co_{0.65}Cu_{0.1}Fe_{0.23}Zr_{0.02})_{7.1}$	7 to 23 – 557 to 1830	10.5 - 0.11	25 - 199

Chapter 3

Materials and Methods

3.1 Materials

Table 3.1 shows the materials that have been used in this study, their functions and properties.

Table 3.1: Materials used in the study.

	Starting material	Function	Particle size, volume or shape	Composition (wt.%) or structure	Image
1	Sm	To be used after decrepitation as an addition for the preparation of CVS-ed and SPS-ed recycled magnets.	Blocks of 1 cm^3	99.5% pure	
2	As-cast $SmCo_5$ rich in Sm (book moulded)	To be decrepitated and to study the properties of the decrepitated powder.	Blocks of 1 cm^3	42.7% Sm, 57.3% Co	
3	As-cast $SmCo_5$ rich in Co (book moulded)	To be decrepitated and to study the properties of the decrepitated powder.	Blocks of 1 cm^3	34.3% Sm, 65.8% Co	Similar to raw 2
4	Sintered $SmCo_5$	To be recycled by strip casting and by decrepitation with CVS and SPS, and polymer-bonded magnets production.	Cylinders of about 0.16 cm^3	36.3% Sm, 63.3% Co, 0.4 % O	

Table 3.1: Continued.

	Starting material	Function	Particle size, volume or shape	Composition (wt.%) or structure	Image
5	Ni-Cu-Ni-coated sintered $SmCo_5$	To remove the coating on the magnets by leaching or HD.	Cylinders of about 0.16 cm^3	34.36% Sm, 63.23% Co, 4.74% Ni, 0.36% Cu, 0.4% O	
6	Fresh $SmCo_5$ powder	To be used for the preparation of CVS-ed and SPS-ed magnets.	4-20 μm	36 % Sm, 63.8 % Co and 0.2 % O	
7	As-cast Sm_2Co_{17} rich in Sm	To be decrepitated and to study the properties of the decrepitated powder.	Blocks of 1 cm^3	29.8 % Sm, 46.1 % Co, 16.0 % Fe, 5.10 % Cu, 2.90 % Zr	Similar to raw 2
8	As-cast Sm_2Co_{17} rich in Co	To be decrepitated and to study the properties of the decrepitated powder.	Blocks of 1 cm^3	24 % Sm, 50.1 % Co, 17.4 % Fe, 5.5 % Cu, 3.0 % Zr	Similar to raw 2
9	Sintered Sm_2Co_{17}	To be recycled by strip casting and by decrepitation with CVS and SPS, and polymer-bonded magnets production.	Cylinders of about 0.19 cm^3	25.4% Sm, 49.1% Co, 17.1% Fe, 5.4% Cu, 2.8% Zr, 0.3 % O	
10	Ni-Cu-Ni-coated sintered Sm_2Co_{17}	To remove the coating on the magnets by leaching or HD.	Cylinders of about 0.19 cm^3	24.8% Sm, 48.1% Co, 17.04% Fe, 5.4 % Cu, 2.84% Zr, 1.49% Ni, 0.3 % O	

Table 3.1: Continued.

	Starting material	Function	Particle size, volume or shape	Composition (wt.%) or structure	Image
11	Fresh Sm_2Co_{17} powder	To be used for the preparation of CVS-ed and SPS-ed magnets.		25.4% Sm, 49.2% Co, 5.4% Cu, 2.8% Zr, 17.1% Fe, 0.1 % O	
12	H_2	To be used for the decrepitation of Sm-Co compounds.	Gas	>99.999% pure	
13	Polyamide 12 (PA12)	To be used for the preparation of polymer-bonded magnets.	Powders, less than 20 μm	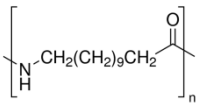	
14	Cu	To be used as an addition for the preparation of a recycled sintered Sm-Co magnet.	Powders, less than 20 μm	99.5% pure	
15	Ni				
16	Co				
17	Fe				
18	Nitric acid (HNO_3)			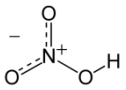	
19	Bromine (Br_2)			Br-Br	
20	Ethanol			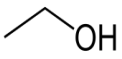	
21	Dimethylformamide (DMF)	To be used for coating removal on the magnets' surface.	Liquid (>99 % pure)	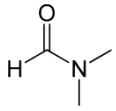	
22	Ethyl acetate (EtOAc)			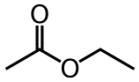	
23	Methyl acetate (MeOAc)			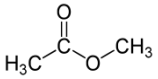	
24	Ethylene glycol (EG)			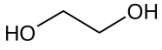	

3.2 Methods and Equipment

3.2.1 Decrepitation process

3.2.1.1 Rotating equipment

The rotating technique was used to facilitate the decrepitation of $SmCo_5$ magnets. 200 g of the $SmCo_5$ magnets was put in a 100 mL stainless steel jar with a lid, which enables evacuation to 0.05 mbar and gas filling up to 15 bar (Figure 3.1). Three cycles of evacuation and refilling with Ar were carried out before the final evacuation to ensure the removal of oxygen. Finally, the jar was filled with hydrogen gas to different pressures of 1 bar, 2.5 bar, 4 bar and 9.5 bar. The jar was then rotated in a planetary ball mill for 3h at 250 rpm to perform the decrepitation reaction. Every 15 min, the rotation was stopped and the jar was filled with hydrogen gas to the starting pressure; to compensate for the hydrogen absorbed by the material. The produced powder after decrepitation was taken inside a glove box with a protective atmosphere, i.e. oxygen concentration less than 10 ppm. The decrepitated powder was left for at least 1 day before further processing, to ensure the complete desorption of the absorbed hydrogen. The rotating equipment was not used for the decrepitation of sintered Sm_2Co_{17} magnets due to the high pressure required for the magnets; usually higher than 15 bar is needed for the latter.

Figure 3.1: Scheme of decrepitation by rotating equipment; the magnets decrepitated are inside the jar to be put in the rotating equipment.

3.2.1.2 Stationary equipment

The stationary equipment (Figure 3.2) was used for the decrepitation of as-cast $SmCo_5$ alloys, as-cast Sm_2Co_{17} alloys, Sm metal, sintered $SmCo_5$ magnets and sintered Sm_2Co_{17} magnets. The material for decrepitation was put in the small tube (1), the chamber (2) was closed using the lid (3), and a vacuum lower than 10 mbar was introduced after purging the jar with Ar as described in 3.2.1.1. The time, temperature and the hydrogen pressure of the reaction depend on the material under investigation. The equipment was designed to be able to withstand a hydrogen pressure of 60 bar and an applied temperature of up to 800 ^{o}C. The decrepitated powder was then handled in the same way as for the ones from the rotation, described above.

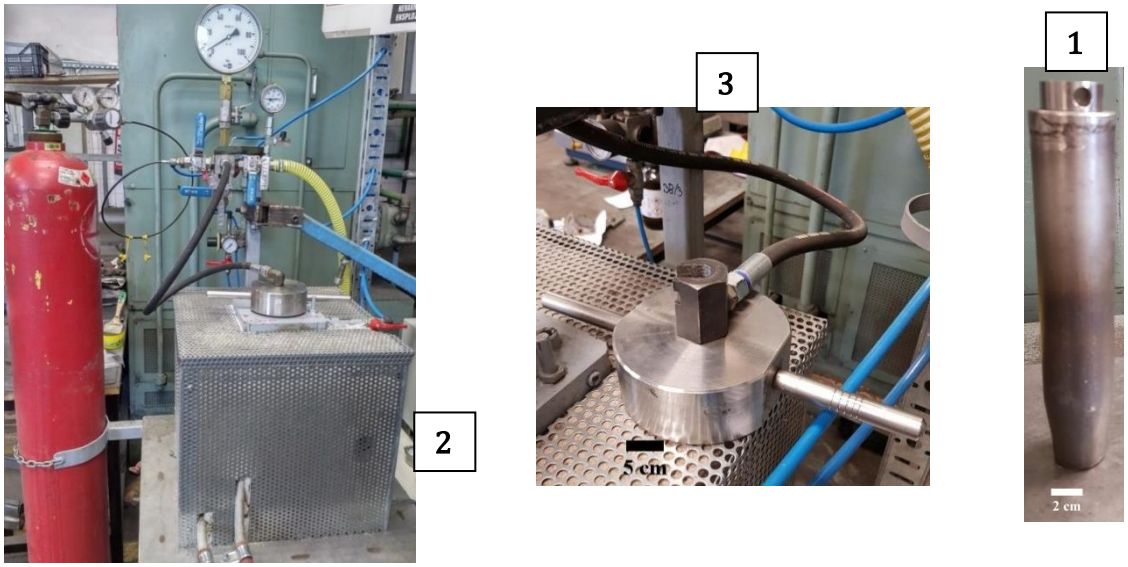

Figure 3.2: The stationary equipment used for the HD of Sm-Co compounds. (1) decrepitation tube, (2) water-cooled chamber and (3) closing lid connected with a valve for vacuum and pressure introduction.

3.2.2 Strip casting

Sintered magnets of $SmCo_5$ and Sm_2Co_{17} were put in a crucible where they were melted by induction under a protective atmosphere with oxygen content of less than 0.2 %. The melt was then left for about 2 min to allow the oxide component to float on the top. The crucible containing the melt was then tilted slowly to avoid the above oxide layer from pouring, and the clean-melt underneath was poured into a tundish with an orifice from which it is delivered to a fast rotating-planar-water-cooled Cu alloy wheel, where it solidifies instantly to thin friable strips-flakes of a thickness less than 0.2 mm. Figure 3.3 shows the components of the furnace used.

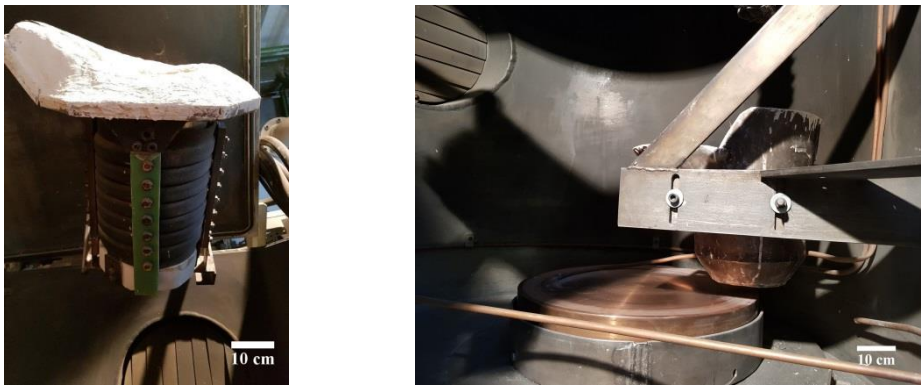

Figure 3.3: The melting crucible (left) and the receiving tundish with the rotating wheel (right) used for the strip casting of Sm-Co material.

3.2.3 Jet milling

All the materials to be used for sintered magnets production were milled using a jet mill with nitrogen atmosphere. Milling is performed with no grinding media included. The grinding action is caused by a compressed-nitrogen-gas from two nozzles on the wall of the mill-body, which causes attrition and collisions of the particles against each other. A third nozzle placed at the bottom is responsible for levitation of the milled particles, Figure 3.4. Particle size of the feed material should be in the range of 150-800 µm. The produced particle after milling was in the range of 4-20 µm by using a nitrogen pressure of around 6 bar for milling. The milled powders were handled only inside the glovebox.

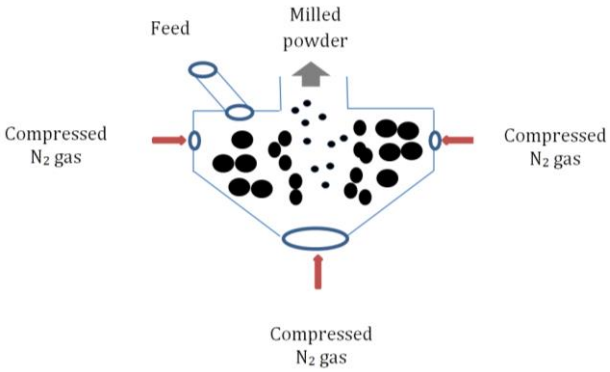

Figure 3.4: Schematic for the jet milling of coarse powder by the compressed N_2 gas and the exclusion of the milled powder.

3.2.4 Homogenization of the powders mix

The powders to be mixed were weighed as for the desired ratio and put in a plastic container inside the glove box, the container was sealed to avoid oxidation. The powders were then mixed in a turbula mixer for 2 hours to ensure homogenization. The plastic containers were opened only inside the glovebox.

3.2.5 Powders alignment and compaction

The powders to be conventionally sintered or to be used for polymer-bonded magnets production were first packed in silicon moulds of a volume of 8 cm^3 to reach a density of about 3 g/cm^3, inside a glovebox. The mould was sealed in a plastic bag to avoid oxidation during further processing. For the production of anisotropic magnets, the powders were aligned using a 3 T magnetic field. The aligned and packed powder was then cold-isostatically pressed at a pressure of 2500 bar to produce green compacts suitable for the sintering experiments. The applied pressure in isostatic pressing is uniform in all directions, which helps form a uniform density and keep a good alignment of the powder.

3.2.6 Conventional sintering

The conventional sintering and heat treatment for the produced green compacts were carried out in a built-in-house furnace. Temperature up to 1600 ^oC can be applied, and vacuum down to 0.05 mbar can be achieved. The furnace can also work under different gases' partial pressures with controlled heating and cooling rates. The sintering and heat treatment profiles used to produce all the conventionally sintered $SmCo_5$ and Sm_2Co_{17} mentioned with and without the additions in the thesis are shown in Figure 3.5 and Figure 3.6, respectively.

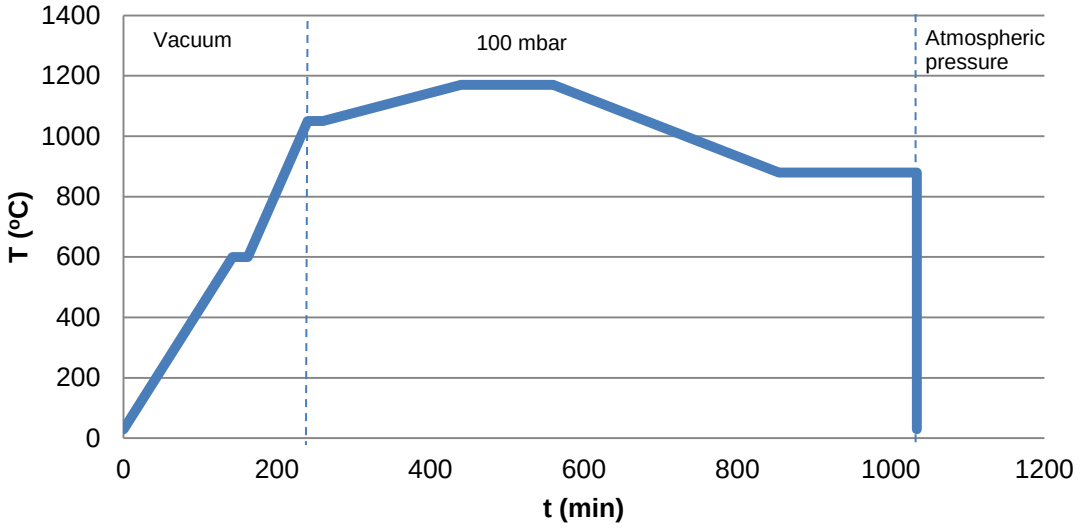

Figure 3.5: The sintering and heat treatment profiles (conventional) for the milled $SmCo_5$ powder, sintering temperature; 1170 °C.

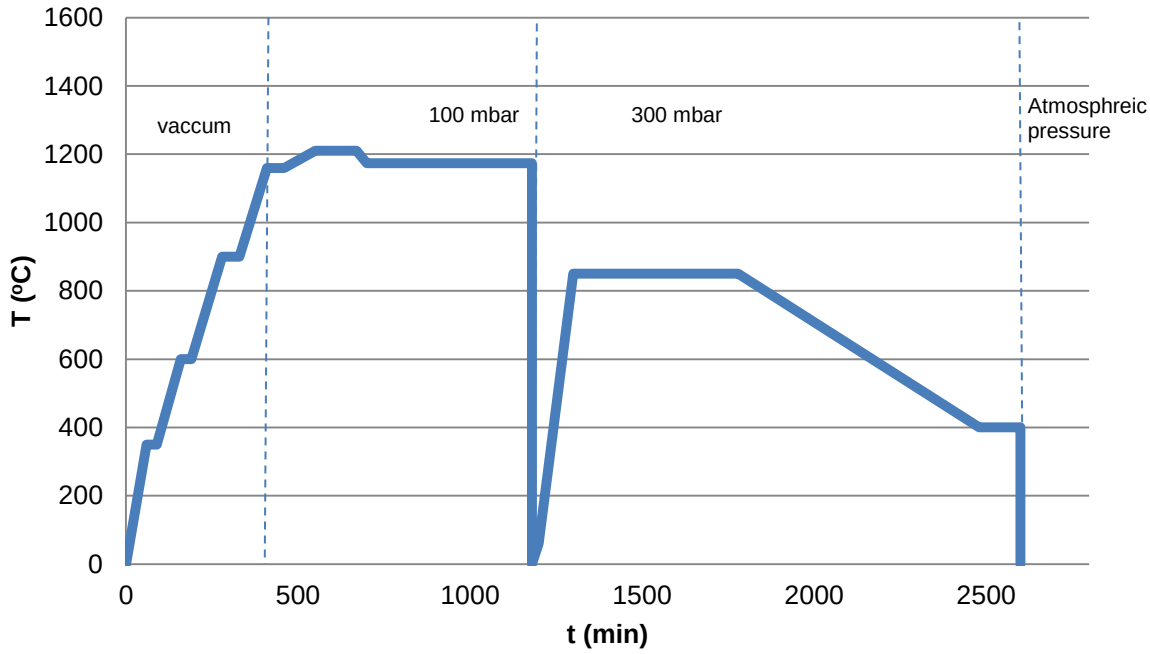

Figure 3.6: The sintering and heat treatment profiles (conventional) for the milled Sm_2Co_{17} powder, sintering temperature: 1210 °C.

3.2.7 Preparation of anisotropic polymer-bonded magnets

The powders used for the production of polymer-bonded magnets were produced by the decrepitation of sintered $SmCo_5$ and Sm_2Co_{17} magnets in the stationary equipment. The decrepitated powder was sieved and only the <125 μm fraction was used for the production of bonded magnets. The aligned and pressed green compact of the magnetic powder with PA 12 binder was heated under atmospheric pressure to a temperature of 200 °C for 1 min to melt the binder. Approximately 80% magnetic powder to 20% PA12 by volume was used which accounts for about 4 wt.% PA 12. The heated compact was taken out of the furnace for cooling and hardening. The produced cylindrical magnets in rod shapes were demagnetized by applying a series of reverse magnetic fields and then ground and cut (using a diamond based materials) in water media to produce discs

suitable for further measurements. The magnet rods and the final disc samples are shown in Figure 3.7.

Figure 3.7: The Sm-Co polymer-bonded rods and final disc, the discs have a diameter of 1 cm.

3.2.8 Spark plasma sintering

The SPS was used to prepare only isotropic magnets, using the decrepitated powder. Inside the glove box, 3 g of the milled powder was put in a 10 mm inner diameter graphite die. The die was then handled in air for less than 5 min to be put in the SPS machine, where in between, the powder inside the die was pressed by a hydraulic press to 5 bar. The SPS sintering parameters were 800-1000 ^{o}C sintering temperature, and a heating rate of 50 ^{o}C/min. The sample was kept at the sintering temperature for 1 min where the applied pressure was 80 MPa (800 bar). After evacuation of the SPS chamber to 0.05 mbar, partial pressure of 200 mbar Ar was kept during sintering to reduce the Sm evaporation. Only for SPS sintered Sm_2Co_{17} magnets, a heat treatment step was further applied to enhance the magnetic properties. The heat treatment profile was the same as the one applied to conventional sintered Sm_2Co_{17} magnets, as shown in Figure 3.5; starting from the portion at 300 mbar partial pressure. The sintering experiments were done using SPS 25 series, model 615, Fuji electronic industrial CO., LTD.

3.2.9 Coating removal

Ni-Cu-Ni-coated Sm-Co magnets were soaked in 10 mL of the liquid solution for coating leaching in a 50 mL glass container. The solution was stirred at 500 RPM using a magnetic rod, at room temperature. An intake sample of 0.1 mL of the reaction was taken at 5-min time interval to be analysed by atomic emission spectroscopy for the metallic components.

3.2.10 Analysis methods

3.2.10.1 Particle size analysis

HELOS/BR, Sympatec was used for the particle size analysis of dry powders in the range of 0.1 µm - 875 µm. The diffraction patterns of a laser beam passing through the previously dispersed particles were measured, where the angle of the diffracted laser was related to the size of the powders, as it is inversely proportional to the particle size. About 1 g of the sample was used for the measurement.

3.2.10.2 Elemental analysis on solids and powders

Eltra ON 900 oxygen/nitrogen determinator was used for the oxygen measurements in the samples. 0.2-0.3 g of the sample was put in a graphite crucible. The crucible provides the carbon to be bound with the oxygen in the sample. The sample is melted in He

atmosphere, and the amount of the produced CO gas is measured and related to the starting amount of the sample, to calculate the concentration of the oxygen content.

Perkin Elmer Optima 5300 DV, inductively coupled plasma atomic emission spectrometer (ICP-OES) was used to analyse Sm, Co, Cu, Fe, Ni and Zr. 0.5 g of the sample to be analysed was digested with 50 mL of the aqua regia solution (3 HCl/ 1 HNO_3). 1 mL of the digested solution was then diluted 100 times and analysed for elemental identification. After excitation with plasma of a temperature of 6000-1000 K, the characteristic emission wavelength and its intensity were used for the qualitative and quantitative identification for the metals in the sample, respectively.

3.2.10.3 Density measurements

The densities of the solid samples were measured by using the Archimedes' principle. The weights of the samples were measured in air and in distilled water and the density was calculated as weight in air/(weight in air − apparent immersed weight in water).

.

3.2.10.4 XRD analysis

PANalytical X'Pert pro multi-purpose diffractometer was used for the crystallography measurement. An X-ray beam, produced by using Cu element, is diffracted through the sample with a scanning range of 30^o to 70^o, the angles and the intensities of the diffracted beam from the material are then measured. About 0.5 g of 300-50 μm of the sample was packed in a 1 cm diameter sample holder, which is then exposed to air during the measurements. X'Pert HighScore Plus program was used for the qualitative identification of the peaks.

3.2.10.5 Magnetic properties measurements

The demagnetization curves for the sintered samples were measured by Magnet-Physik's permagraph with a maximum applied field of 1500 kA/m. An opposite magnetic field is applied on the previously magnetized sample and the polarization of the sample is measured to draw the second quadrant of the hysteresis loop. The instrument requires a symmetric sample with two faces parallel to each other.

3.2.10.6 Microstructure and energy-dispersive X-ray analysis

3.2.10.6.1 Scanning electron microscopy analysis

3.2.10.6.1.1 Samples preparation

For powders, a small fraction of the powder was sprinkled on a carbon tape, the sample was then blown with air to remove the excess unstuck powder on the tape.

For bulk solid samples, the samples were mounted in an epoxy, the latter was mixed with a suitable hardener. The mounted samples were then ground using a series of silicon carbide grinding sheets having a grit size from P240 to P1200. To be suitable for a microstructure study, the samples were polished using clothes polishing sheets and a polycrystalline diamond polishing paste (3 μm and ¼ μm). Struers Tegrapol-15 machine was used for grinding and polishing. During the preparation steps, the samples were continuously checked by the Nikon Eclipse E600POL optical microscope to ensure the grinding efficiency and the scratches removal.

3.2.10.6.1.2 Carbon coating

To avoid charging of the sample from the electron beam when performing the microstructure analysis, less than 10 nm carbon coating was applied using BAL-TEC SCD 005. The carbon coating is applied by evaporation using a heated carbon thread due to an applied electric potential under vacuum.

3.2.10.6.1.3 Etching

A mixture of chromium oxide (4 g) and sodium sulphate (1 g) in 50 mL deionized water was used to etch the sintered samples, by dipping the sample in the solution for around 6

seconds; to enhance the grain boundaries. After etching, the samples were washed with ethanol and dried in a vacuum desiccator for 1 day before the microstructure analysis.

3.2.10.6.1.4 Microscopes

The microstructure analysis for the powders after decrepitation was carried out by the Helios NanoLab™ 650 scanning electron microscope, whereas Jeol JSM-7600F scanning electron microscope with In-Lens thermal field emission electron source and Joel JSM-5800 with LaB_6 thermionic emitter were used for solid samples characterizations. An operating voltage of 20 kV was used for both microscopes. The incident electrons from the sources are scanned through the sample and the produced electrons from the interaction of the sample with the incident electrons are collected sequentially. The microscopes can detect backscattered and secondary electrons which are the incident electrons and the sample's produced electrons after the interaction, respectively. Built-in SiLi detectors were used for the detection of the characteristic X-rays of the component phases.

3.2.10.6.2 Transmission electron microscopy analysis

3.2.10.6.2.1 Samples preparation

In order to be suitable for the TEM study, a lamella of thickness less than 100 nm was prepared using the Helios NanoLab™ 650 instrument. The lamella was cut from the solid sample using a focused ion beam and attached on a Cu grid by platinum deposition for further TEM characterization.

3.2.10.6.2.2 Microscopes

Jeol JEM-2010F with a field emission electron source (up to 200 kV) and SiLi detector was used for the transmission electron microscopy analysis. The transmitted electrons are collected continuously and focused to form a magnified image.

Chapter 4

Results and Discussion

4.1 $SmCo_5$

4.1.1 HD of as-cast $SmCo_5$ alloys and Sm metal

Before starting the Sm-Co magnets recycling process, it was useful to test the application of HD on fresh as-cast Sm-Co compounds (book moulded) and Sm metal. This will give insights about the use of the process for the application on the recycling of sintered magnets.

In the industry, it is hard to control the Sm content during the casting process due to Sm evaporation. Therefore, two as-cast compositions are usually prepared for the production of sintered Sm-Co magnets. One of the two alloys to have a higher Sm content than needed for the final magnet (42.7 wt.% Sm was used) and one with higher Co content (34.3 wt.% Sm was used). The Sm content in sintered $SmCo_5$ magnets is usually around 36 wt.%. Both prepared alloys showed to have a density of more than 98% of their theoretical values. Figure 4.1 shows the microstructure of the used alloys, both of them showed to contain the $SmCo_5$ dark-grey phase with the light-grey phase of Sm-rich phases of mainly Sm_2Co_7, as measured by EDX analysis. As expected, the concentration of the latter phase was much higher for the alloy having a higher Sm content.

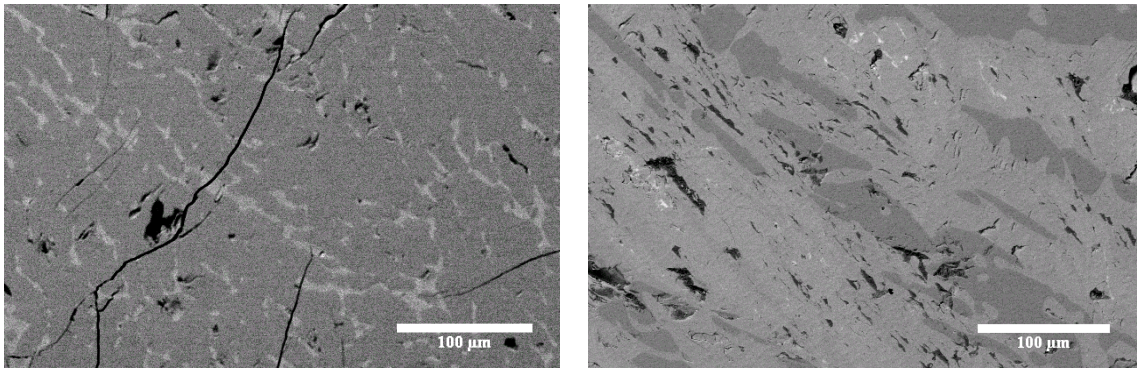

Figure 4.1: BSE images for the as-cast alloys with the composition close to industrial $SmCo_5$ magnets, rich in Co (left) and in Sm (right).

Applying only 1 bar of hydrogen gas at room temperature for 3 h using the stationary equipment was enough for the decrepitation of the two as-cast alloys. The particle sizes of the powders after decrepitation were less than 400 µm for both alloys. The decrepitation for the alloys starts with the absorption of the Sm_2Co_7 phase to the hydrogen gas, as it has a higher Sm content and thus a higher hydrogen absorption affinity as described previously. The presence of continuous and uniform Sm_2Co_7 through the microstructure of the alloys causes the easiness of the decrepitation and a pressure of 1 bar was enough for the fracture of the materials. Figure 4.2 shows the XRD for the alloys before and after HD. The peaks of the Sm_2Co_7 phase decreased in the two alloys after decrepitation due to the hydrogen absorption and oxidation to SmO during the XRD analysis, as clearly seen for the

alloy rich in Sm. Video 1 shows the disintegration of the $SmCo_5$ alloy rich in Sm due to the hydrogen absorption.

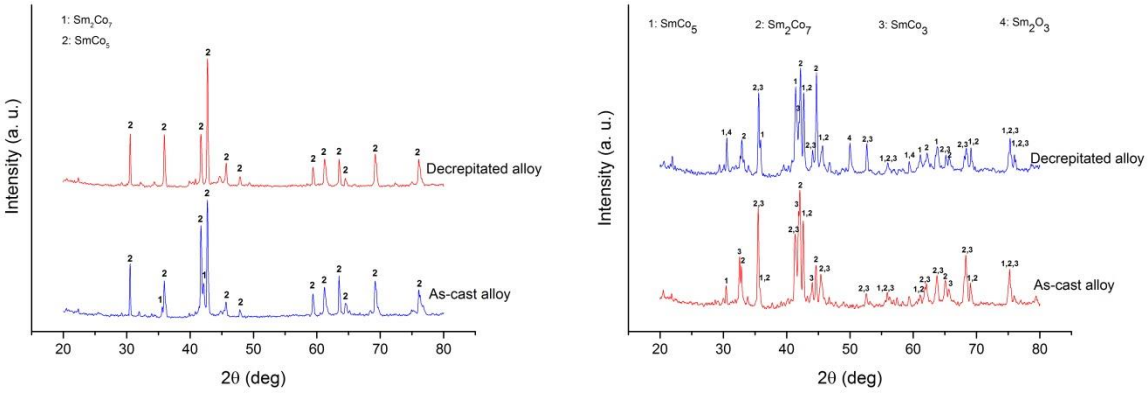

Figure 4.2: XRD patterns of the as-cast $SmCo_5$ alloys rich in Co (left) and rich in Sm (right), before and after decrepitation.

Blocks of Sm metals were also decrepitated to be used for further experiments. The conditions needed for the Sm decrepitation were 2 bar of hydrogen gas and a temperature of 400 °C for 3 h. Heating was required for the decrepitation of the Sm metal, to activate the hydrogen to penetrate the formed oxide layer on the metal surface. By applying the previously mentioned conditions, the produced material showed to contain large friable aggregates. The produced aggregates are easily disintegrated by hand to a fine particle size lower than 100 µm. This means that not all the Sm metal converted to Sm-hydride during the decrepitation, which is an efficient way of reducing the oxidation in further steps, as Sm-hydride is known to be more reactive to oxidation than Sm metal itself. The produced powders was milled to a particle size less than 20 µm, to be used as an addition for the sintering of the recycled powder as will be described later.

4.1.2 HD for the recycling of $SmCo_5$ magnets: conventional sintering

4.1.2.1 Decrepitation by using the rotating equipment

$SmCo_5$ sintered magnets were shown to be easily decrepitated by applying a hydrogen pressure of 1 bar, 2.5 bar, 4 bar or 9.5 bar for 3 hours, room temperature in the rotating equipment to produce powders lower than 200 µm. Figure 4.3 shows the produced decrepitated powder.

Figure 4.3: The jar containing the produced powder after applying HD on sintered $SmCo_5$ in the rotating equipment. Scale bar and the full experimental setup in Figure 3.1.

4.1.2.2 Decrepitation in the stationary equipment

$SmCo_5$ magnets showed also to be successfully decrepitated by applying a pressure of 5 bar of hydrogen, room temperature in the stationary equipment, without rotation. But as the kinetics for the decrepitation was slow, at least one day was needed for the complete decrepitation of the 1 kg magnets used for the experiment. Figure 4.4 (right) shows the decrepitated powder, where it is shown that there was still a very large particle in the 100 mm range, even after the 1 day experiment. However, those particles are friable due to the hydrogen absorption and were easily reduced in size. Figure 4.4 (left) shows the fracture in the structure of the magnets by the hydrogen absorption.

Figure 4.4: The fracture in the magnet structure due to the hydrogen absorption (left – scale bar for similar magnets in Table 3.1), and the decrepitated powders by using the stationary equipment (right).

The stationary equipment was used to prove that it is possible to perform decrepitation for $SmCo_5$ sintered magnets without the rotation effect; however, higher pressures and longer times were required for the reaction completion. It was decided to continue the sintering experiments using the product from the rotating equipment as much lower hydrogen pressure and time were required in comparison to the stationary experiment.

4.1.2.3 Decrepitation mechanism and the properties of the decrepitated powders

The SE images of the powders after decrepitation from the rotating equipment, produced by different pressures at 1 bar, 2.5 bar, 4 bar and 9.5 bar, are shown in Figure 4.5. For all pressures, there is a large distribution of particle sizes, with the presence of very fine particles, lower than 300 nm. The upper particle size of the decrepitated powder throughout the samples was less than 200 μm. By definition, HD is always accompanied by the presence of cracks in the decrepitated powders due to hydrogen absorption in the microstructure of the material. The presence of the rotating force had the effect of decreasing these cracks and the production of smaller particle sizes; however, some cracks were still visible in the powders. (1)

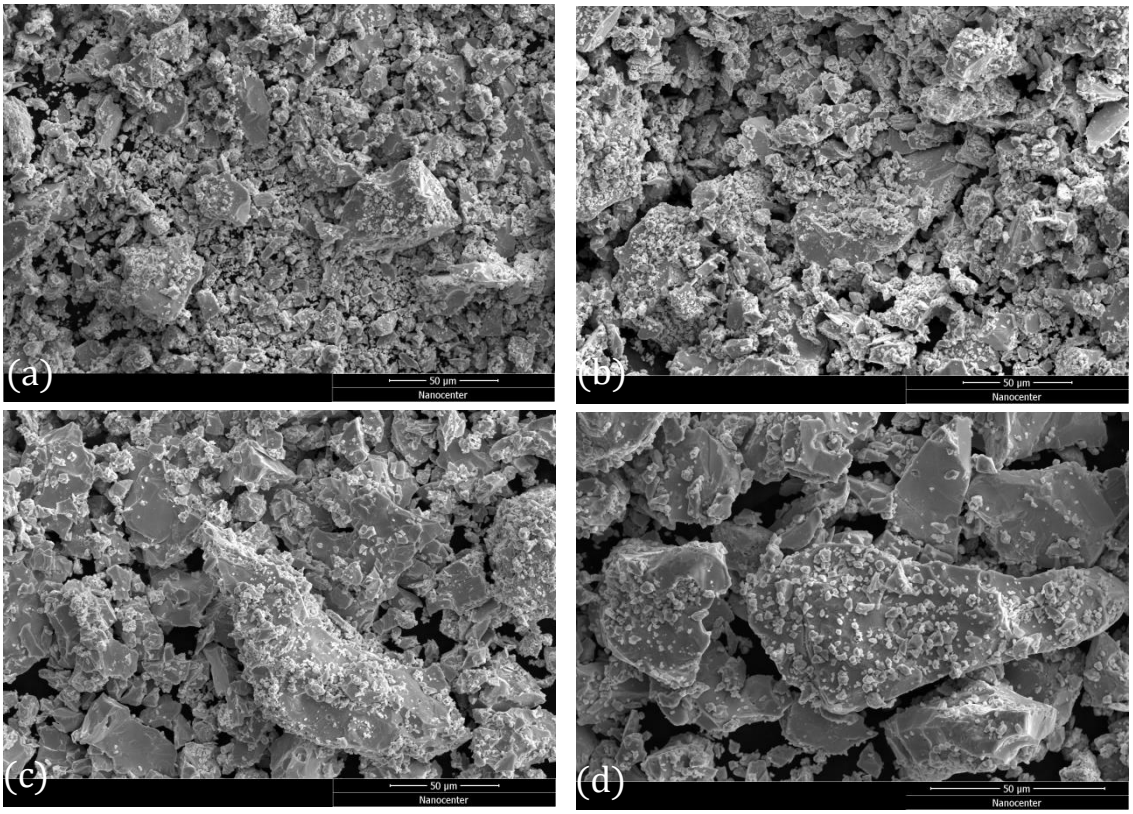

Figure 4.5: SE images of the decrepitated powder of a sintered $SmCo_5$ magnet using the rotating equipment, the applied pressures were 1 bar, 2.5 bar, 4 bar and 9.5 bar for (a), (b), (c) and (d), respectively.

Figure 4.6. shows the XRD patterns for the starting magnet and the decrepitated powders. It is shown that the patterns for the magnet and the powders after decrepitation by different pressures are very similar. The HD reaction starts by the hydrogen reaction with the Sm_2Co_7 and other Sm-rich phases of a low concentration, with the formation of Sm-hydrides and Co-rich phases. This is confirmed by the disappearance of the Sm_2Co_7 peak in the decrepitated powders. Sm-hydrides could not be identified because of the low concentration and the oxidation to form Sm-oxides during the preparation and the measurement steps. Hydrogen is also absorbed in the interstitial sites of the $SmCo_5$ matrix phase. As described earlier, when the hydrogen pressure above the magnet is relieved, the interstitially absorbed hydrogen is relieved from the $SmCo_5$ structure. The decrease in the intensity of some peaks of the $SmCo_5$ phase after decrepitation indicates that in addition to the interstitial hydrogen absorption, a small portion of $SmCo_5$ is dissociated by hydrogen gas to form Sm-hydrides and Co-rich phases. (1)

4.1.2.4 Preparation of recycled magnets and their properties

As the XRD patterns and the microstructures were similar for all the decrepitated powders from different pressures, it was expected that the magnets produced from any mentioned powder would have the same properties. The powder produced from decrepitation at 4 bars was selected for further sintering experiments. (1)

Two different compositions were prepared to produce recycled magnets, 1- 100% milled recycled powder (Recycled), 2- 98.5 wt.% milled recycled powder + 1.5 wt.% milled decrepitated Sm (Recycled+Sm). After conventional sintering, the measured density for the Recycled and the Recycled+Sm magnets was 8.33 g/cm^3 and 8.35 g/cm^3, respectively, which is slightly higher than the density of the original magnet of 8.28 g/cm^3. For comparison, Figure 4.7 shows the BSE images of the original magnet before decrepitation and the recycled magnets. The microstructure of the original magnet has

been recovered after recycling. By using EDX analysis, it was measured that the original and the recycled magnets consist of the $SmCo_5$ matrix phase, Sm_2Co_7 phase which is shown as light grey regions distributed randomly along the matrix phase, small brightest regions of Sm-rich phases and Sm-oxides. As shown in Figure 4.7, the Sm_2Co_7 phase content in the Recycled+Sm magnet was much higher than in the other two sintered magnets, due to the added Sm content in the former. During the re-sintering process, the oxygen content has been increased from 0.37 wt.% in the original magnet to about 0.48 wt.% in the recycled magnets.

Figure 4.8 shows the SE images of the original and the Recycled magnet after etching. After recycling, there is a refinement in the microstructure. This can be explained due to the presence of nano-size particles in the recycled powders after decrepitation, which are not present in the powder used to prepare the original magnet. The original magnet was produced by a non-decrepitated powder of a particle size of 4-20 μm. (1)

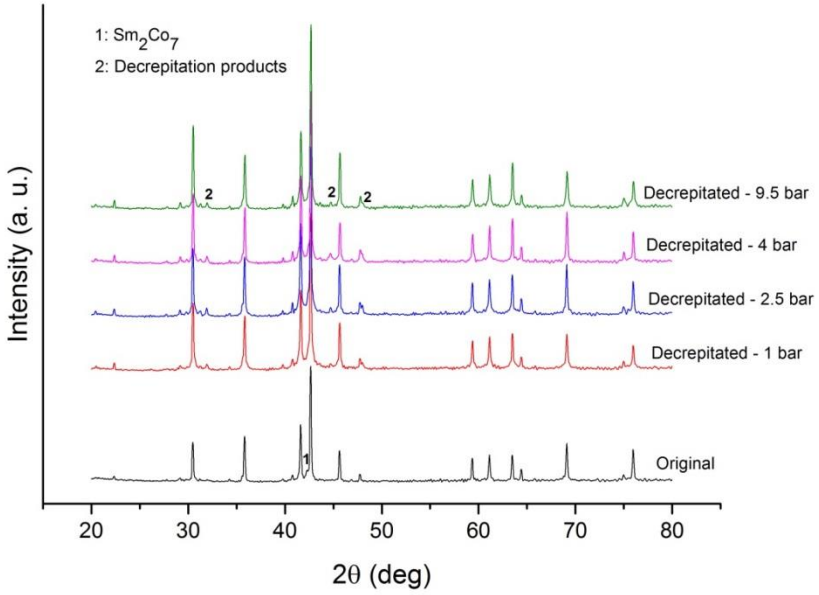

Figure 4.6: XRD patterns for the original magnet and the decrepitated powders by 1-9.5 bar. All the unmarked peaks related to the $SmCo_5$ phase. The Sm_2Co_7 phase has disappeared after decrepitation with the appearances of new phases of Sm-hydrides, Sm-oxides and Co-rich phases.

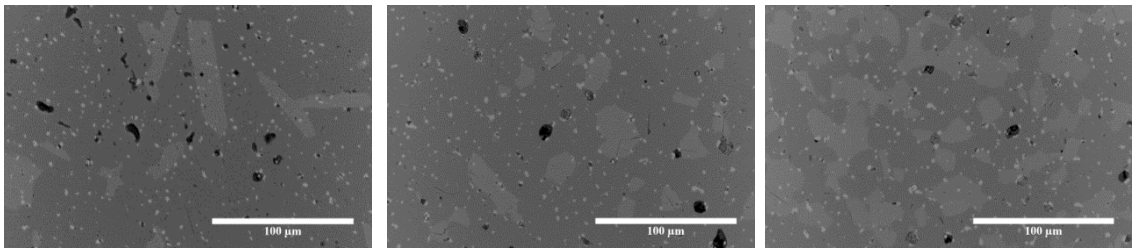

Figure 4.7: BSE images for the original magnet (left) and the recycled magnets; Recycled (middle) and Recycled+Sm (right). All magnets consist of the $SmCo_5$ matrix phase, Sm_2Co_7 light grey clusters with bright regions of Sm-rich phases and Sm-oxides, and pores.

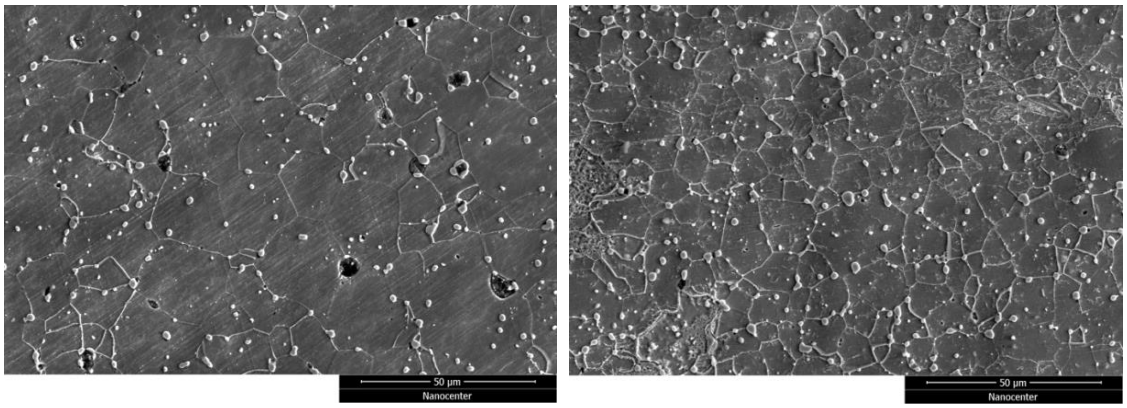

Figure 4.8: SE images for the etched original magnet (left) and the Recycled magnet (right). In comparison to the original magnet, there is microstructure refinement for the magnet after recycling. (1)

Fig. 4.9 shows the demagnetization curves for the original and the recycled magnets, Table 4.1 shows a comparison between their magnetic properties. The B_r for the Recycled magnet and the Recycled+Sm magnet were 0.94 T, 0.93 T, respectively, in comparison to 0.91 T for the original magnet. The slight increase in B_r may be explained as the presence of a nano-particle size in the recycled powders increase the alignment and compaction of the powder which results in an increase in B_r, this is also confirmed by the microstructure refinement and the increase in density of the recycled magnets. Moreover, the recycled magnets were compacted by isostatic pressing, where the original magnet was prepared by axial pressing. The use of isostatic pressing is known to be a reason for the B_r enhancement when compared to axial pressing. The presence of a knee in the demagnetization curve of the Recycled+Sm magnets can be related to the increase of the Sm_2Co_7 phase ratio in comparison to the original and the Recycled magnets. As a result of B_r enhancement, the $(BH)_{max}$ of the Recycled magnet was 171.1 kJ/m^3 and 162.0 kJ/m^3 for the Recycled+Sm in comparison to 156.92 kJ/m^3 for the original magnet.

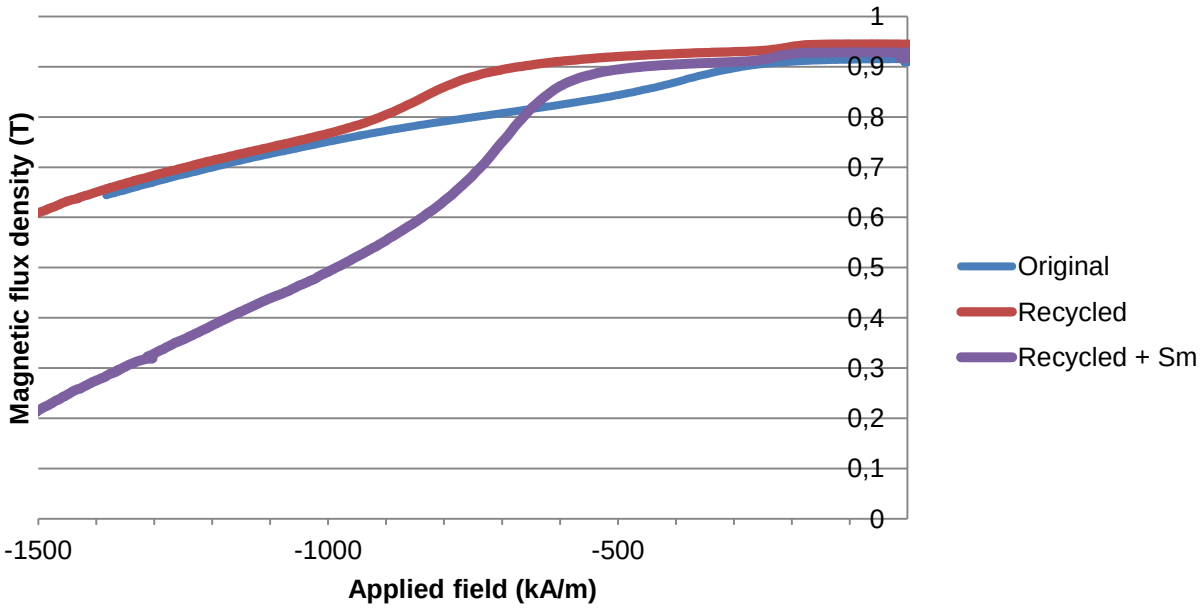

Figure 4.9: The demagnetization curves for the original and the recycled magnets by applying a reverse magnetic field *H*.

Table 4.1: Comparison between the magnetic properties for the original and recycled $SmCo_5$ magnets by HD, ${}_iH_c$ for all the magnets is >1500 kA/m.

	B_r [T]	${}_bH_c$ [kA/m]	$(BH)_{max}$ [kJ/m^3]
Original	0.91	645.1	156.8
Recycled	0.94	709.6	171.1
Recycled+Sm	0.92	656.8	162.0

4.1.3 SPS sintering for the decrepitated powder

Figure 4.10 shows the demagnetization curves for the SPS samples produced by sintering the milled decrepitated powder (from the 4 bar experiment using the rotating equipment) at 800 °C, 850 °C, 900 °C, 950 °C, and 1000 °C, the rest of the sintering conditions are mentioned in Chapter 3. For SPS experiments, only the Recycled+Sm composition was used; the latter with the Sm addition was chosen to compensate for the Sm evaporation during the sintering process as it is a well-known problem for the sintering for Sm containing compounds in SPS [110]. Table 4.2 shows the magnetic properties, density, and the oxygen content for the magnets. The density has shown to increase with the sintering temperature from 6.86 g/cm^3 at 800 °C to 8.4 g/cm^3 at 1000 °C, which is about 100% of the theoretical density of the magnets. On the other hand, the oxygen content showed to decrease with increasing the sintering temperature, as the densification in SPS involves removing the surface oxide because of the voltage breakdown effect, which means increasing the sintering temperature would lead to more efficient removing of the surface oxygen toward the full densification [32]. (2)

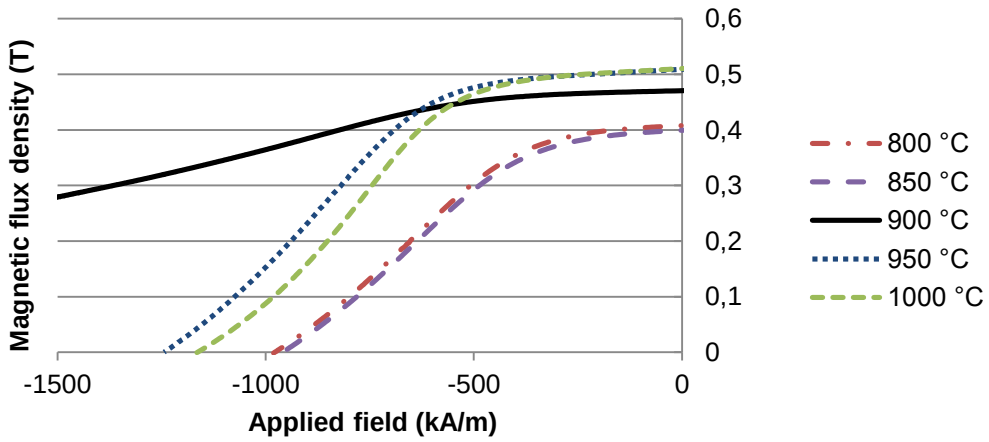

Figure 4.10: The demagnetization curves for the SPS-ed samples sintered at 800–1000 °C. The sample sintered at 900 °C showed the best coercivity. (2)

As expected from the relative relationship between the density and the sintering temperature, the B_r and $(BH)_{max}$ of the samples also showed to increase with the sintering temperature to reach a value of 0.51 T and 50.1 kJ/m^3, respectively, for the sample sintered at 1000 °C. The sample sintered at 900 °C showed a B_r of 0.47 T, which is about 50% of the value for the anisotropic $SmCo_5$ magnets produced industrially, which have a B_r of 0.80–0.96 T [25]. (2)

Table 4.2: Density, oxygen content and magnetic properties of the SPS-ed samples sintered at 800-1000 °C. (2)

Temperature	ρ [g/cm^3]	Oxygen cont. [wt.%]	$(BH)_{max}$ [kJ/m^3]	$_iH_c$ [kA/m]	B_r [T]
800 °C	6.86	1.20	31.9	978.6	0.41
850 °C	7.14	0.76	30.5	960.0	0.40
900 °C	8.11	0.66	43.4	>1500	0.47
950 °C	8.38	0.49	49.8	1243	0.51
1000 °C	8.40	0.47	50.1	1164	0.51

For the samples sintered at lower than 900 °C, due to the incomplete phases formation for those samples and the presence of high oxygen content and large pores percentage, the coercivity value was lower than the one for the industrial conventional sintering $SmCo_5$ magnets, with $_iH_c$ of less than 1000 kA/m. Sintering at 900 °C at the same conditions has the effect of properly densifying the magnet to reach a density of 96% of the theoretical density. The measured $_iH_c$ value for this sample was higher than 1500 kA/m. Increasing the sintering temperature further showed to negatively affect the shape of the demagnetization curve, where the $_iH_c$ value was dropped to 1243 kA/m and 1164 kA/m for 950 °C and 1000 °C samples, respectively. The decrease of the $_iH_c$ upon increasing the sintering temperature is believed to be due to the excessive formation of the Sm_2Co_7, as it will be shown from the microstructure and XRD studies later, and smoothing out of the grain surface, as described by Menushenkov [111] for the decrease in the coercivity of the $SmCo_5$ magnets after heat treatment above 900 °C for CVS magnets with Sm content of 36.4 wt.%. Note that the level of the carbon uptake from the graphite die during the SPS sintering is not enough to drastically change the magnetic properties of the produced magnets, as shown by Mackie [112] for $Sm(Co,Fe,Cu,Zr)_z$. (2)

In order to compare between the SPS and CVS sintering techniques for the production of sintered $SmCo_5$ magnets, Figure 4.11 shows the demagnetization curves at room temperature and 180 °C for the SPS sample produced at 900 °C, as it showed to have the best coercivity among other SPS samples, and a fresh isotropic $SmCo_5$ magnet produced by the CVS route. Table 4.3 shows a comparison between their density, oxygen content, B_r, $(BH)_{max}$, $_iH_c$, and $_bH_c$. At room temperature, the SPS sample showed to have better B_r , coercivity, and $(BH)_{max}$ in comparison to the CVS samples, even though the latter has a better density and lower oxygen content than the former. This is likely to be due to the microstructure refinement after HD due to the large particle size distribution of the decrepitated powders as described earlier. Heating to 180 °C has resulted in a more deterioration effect for the magnetic properties of the SPS sample because of its lower density and higher affinity for the interstitial oxidation. Nevertheless, even at 180 °C, the latter is still showing good properties: B_r of 0.44 T, $_iH_c$ of 1502 kA/m, and $(BH)_{max}$ of 36.4 kJ/m^3, which confirms the applicability of the magnet for high temperature applications as in electric vehicles and space applications. (2)

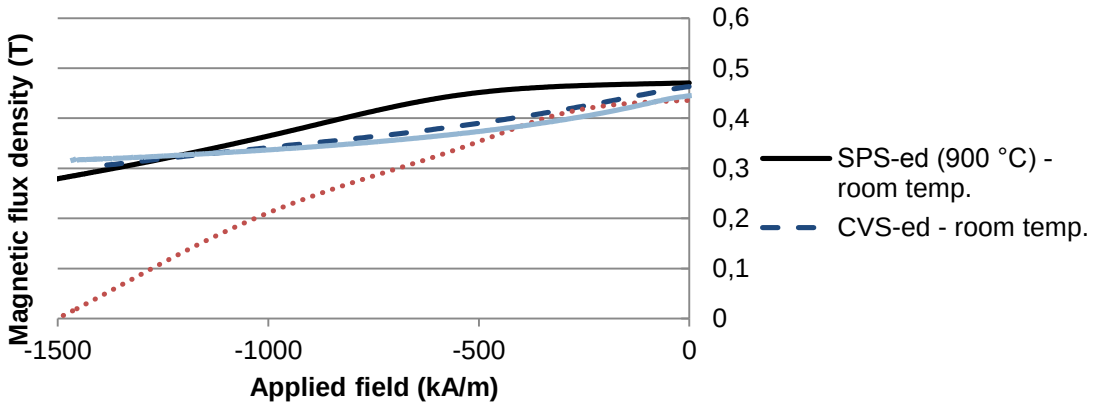

Figure 4.11: Comparison between the demagnetization curves of the SPS-ed sample sintered at 900 °C and the CVS-ed sample; at room temperature and 180 °C. (2)

Table 4.3: Density, oxygen content and magnetic properties of the SPS-ed sample sintered at 900 °C and CVS-ed sample; at room temperature and 180 °C. (2)

	$(BH)_{max}$ [kJ/m³]	$_jH_c$ [kA/m]	$_bH_c$ [kA/m]	B_r [T]	ρ [g/cm³]	Oxygen cont. [wt.%]
SPS-ed (900 °C) - room temp.	43.4	>1500	366.8	0.47	8.11	0.66
CVS-ed - room temp.	38.0	>1500	328.4	0.46	8.25	0.4
SPS-ed (900 °C) -180 °C	36.4	1502	322.4	0.44	-	-
CVS-ed - 180 °C	34.8	>1500	314.2	0.44	-	-

Figure 4.12 shows the BSE images of the CVS sample and the SPS samples sintered at 800 °C, 900 °C, and 1000 °C; Figure 4.13 shows their XRD patterns. The detected phases in the samples by the EDX were as follows: the matrix $SmCo_5$, randomly distributed light grey Sm_2Co_7 phase with a random size, and white small spots which were analysed to be a mixture of Sm-oxides and Sm-rich phases. From the XRD patterns, both the SPS samples at 800 °C and 900 °C showed the presence of small fractions of the Sm_2Co_{17} phase, with a higher concentration in the 800 °C samples. The appearance of Sm_2Co_{17} is due to the increase of the oxygen concentration and the consumption of Sm in these samples and results in the decrease in the $_iH_c$ values for the samples sintered at a temperature lower than 900 °C, as mentioned above. The Sm_2Co_{17} phase has disappeared by increasing the sintering temperature with increasing the percentage of the Sm_2Co_7 phase, where the SPS samples at 1000 °C showed to have Sm_2Co_7 with a higher percentage than other samples, without the appearance of any traces of the Sm_2Co_{17} phase. (2)

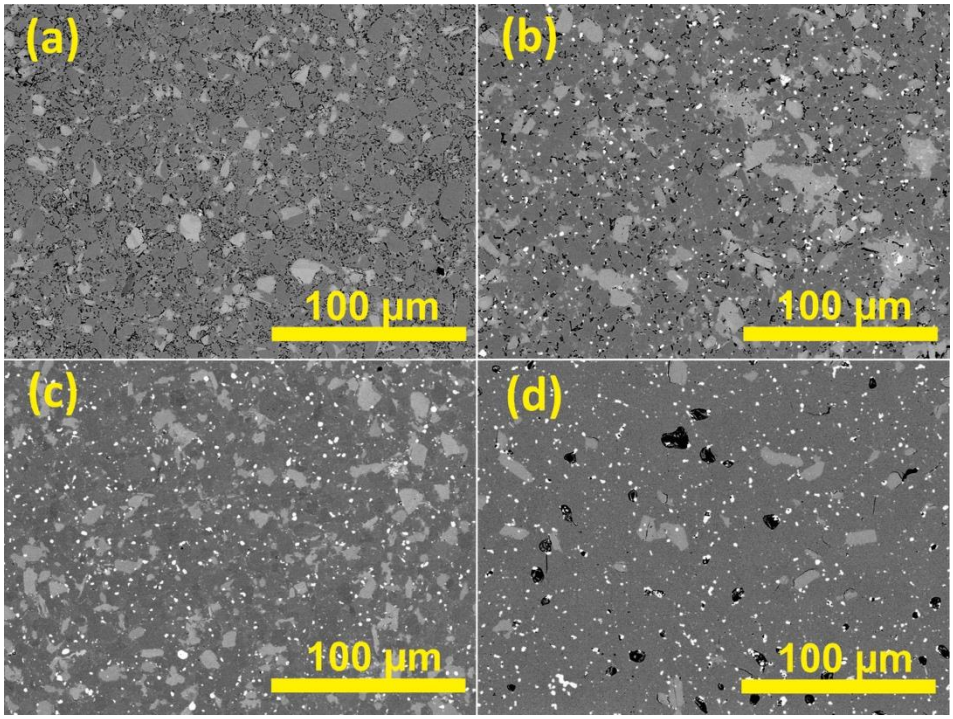

Figure 4.12: The BSE images of the SPS-ed samples sintered at 800 °C (a), 900 °C (b) and 1000 °C (c), and the CVS-ed sample (d). (2)

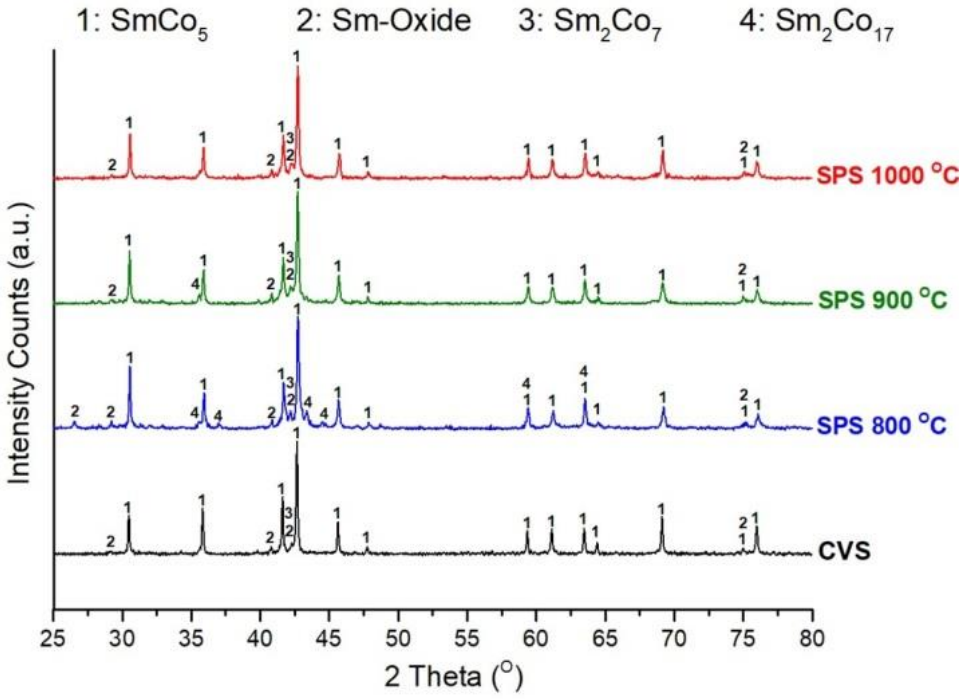

Figure 4.13: The XRD patterns of the CVS-ed sample and SPS-ed samples sintered at 800 °C, 900 °C, and 1000 °C. (2)

4.1.4 Polymer-bonded recycled $SmCo_5$ (anisotropic)

Another possibility for the use of the recycled decrepitated powder produced by applying HD on sintered $SmCo_5$ is to produce polymer-bonded magnets. A pressure of 5 bar for 1 day was applied on the sintered magnets at room temperature in the stationary equipment. Only the size fraction of the decrepitated powder of <125 μm was used to produce polymer-bonded magnets. The percentage of the <125 μm fraction is about 20% of the decrepitated powder, however the decrepitated powder of a larger particle size is friable and can be reduced easily by hand. Figure 4.14 shows the demagnetization curve for the produced magnet. A density value of 4.9 g/cm³ was achieved for the bonded magnets, which is about 70% of the theoretical density of the magnets of 6.9 g/cm³; based on the plastic and metal portions. This can be attributed to the absence of any pressure during the compaction of the magnets in the heating step, as it is the case for injection and compaction moulding. The magnets also showed poor B_r value of 0.45 T and low $_iH_c$ of 249.6 kA/m and $(BH)_{max}$ of 34.3 kJ/m³ which is due to the oxidation of the Sm during the heating step, as the magnets were prepared in air. For Sm_2Co_{17} powder, as it has a lower Sm content and no Sm rich phases, lower oxidation is expected to occur and the magnetic properties of the polymer-bonded magnets are expected to be better in comparison to the one from $SmCo_5$ as will be shown in the next sections.

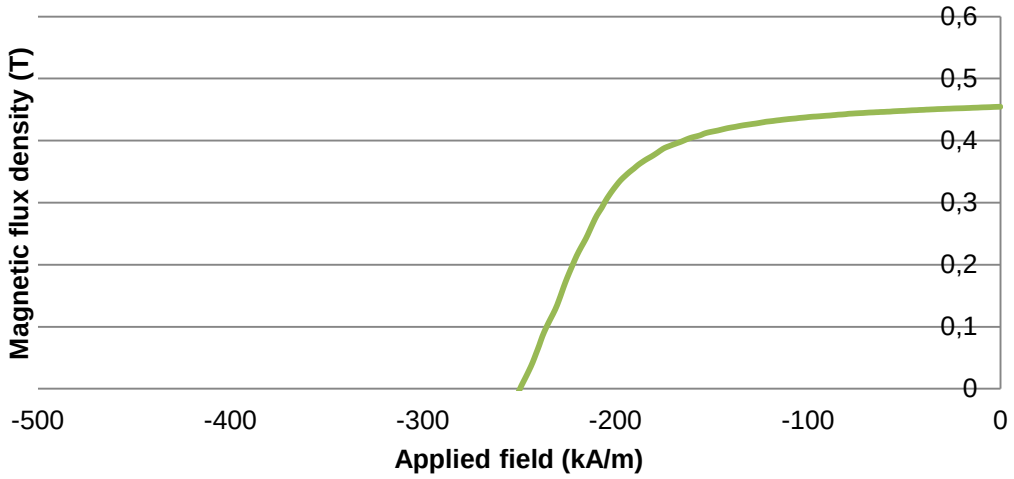

Figure 4.14: The demagnetization curve for the polymer-bonded magnets prepared from decrepitated $SmCo_5$ powder.

4.1.5 Decrepitation of Ni-Cu-Ni-coated $SmCo_5$ magnets

Hydrogen gas was applied on the Ni-Cu-Ni-coated $SmCo_5$ magnets to test the possibility of decrepitation without removing the coating layers. Figure 4.15 shows a cross-section of the Ni-Cu-Ni coating usually applied on Sm-Co magnets. The thickness of the inner Ni layer is around 6 μm , the middle Cu is 2 μm and the outer Ni layer is 12 μm. It was shown that the presence of Ni-Cu-Ni layers does not hinder the decrepitation of the magnets by the rotating equipment and the coated magnets are decreased to the same size of lower than 200 μm by applying a pressure of 1 bar, regardless of the coating. The previous is because the presence of a rotation force would cause some of the surface of the magnet to be exposed to hydrogen due to attrition and collisions. Fig 4.16 shows the produced powder by the decrepitation of coated $SmCo_5$ magnets, the Ni-Cu-Ni coating is shown as silver particles in the brown $SmCo_5$ powder. It was hard to separate the coating for the decrepitated powder produced by the rotating equipment via sieving, as they have similar particle sizes.

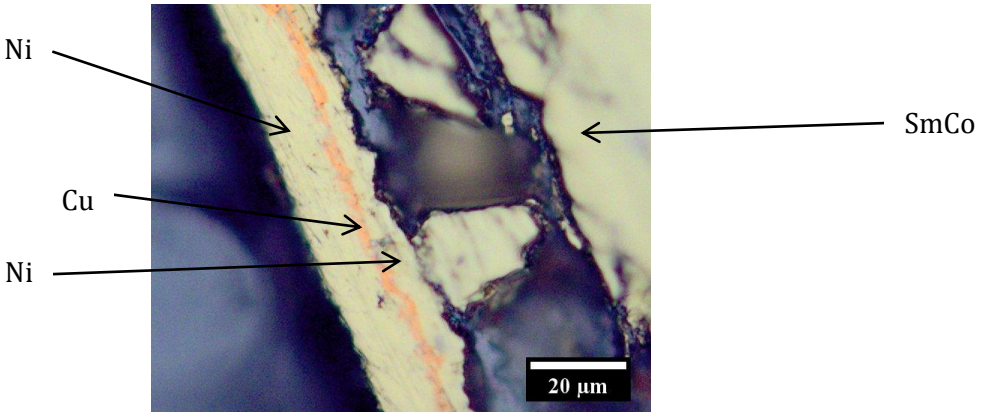

Figure 4.15: Optical microscopy of the three layers of Ni-Cu-Ni usually applied on Sm-Co magnets.

Figure 4.16: The decrepitated powder of coated $SmCo_5$ magnets using the rotating equipment. The coating material appears as silver particles imbedded in the magnet powder.

The stationary equipment was also used for the decrepitation of the coated $SmCo_5$ magnets, where 10 bar for 1 day was needed; in comparison with 5 bar for the uncoated magnets. Figure 4.17. shows the magnets decrepitated by the stationary equipment; most of the coating did not disintegrate and the expansion of the magnet volume due to hydrogen absorption causes the fracture of the coating. The coating layers were sieved, 98 wt.% of the coating material was removed using a sieve size of 250 µm, but also 15 wt.% of the magnets' decrepitated powder was found to be removed alongside the coating.

Figure 4.17: The decrepitated magnet showing the fracture of the Ni-Cu-Ni coating. Scale bar for simliar magnets in Table 3.1.

4.1.6 Chemical dissolution of Ni-Cu-Ni coating on $SmCo_5$ magnets

Another possibility to remove the coating material was by the application of liquid chemical compounds. 2M HNO_3 and 1 vol.% Br/organic systems were investigated to remove the Ni-Cu-Ni coating layers from the surface of the coated sintered magnets. The kinetics for the dissolution of the Ni from the coating on the magnet and Sm and Co elements by the nitric acid reaction are shown in Figure 4.18, the Cu presence in the coating material could not be identified in the intakes from the dissolved solution, probably because its concentration is lower than the detection limit of the ICP-OES, as many small samples were taken; 0.1 mL every 5 min. As there was no available method to accurately measure the concentration of Ni and Cu coating on the magnet that is used for the dissolution experiment, ICP-OES analyses for 5 coated magnets were performed and the concentrations of Ni and Cu were measured. An average concentration of Ni of 24.99 mg/magnet and Cu of 5.07 mg/magnet was calculated for the 5 coated magnets to be used for further measurements. The percentage variation of Ni and Cu of the measurements was also calculated, where it was 10% for Ni and 25% for Cu, and the values were used as error bars on all the next figures for the dissolution of the coating on $SmCo_5$ and Sm_2Co_{17}.

The metals react with the nitric acid with the production of metal nitrate with NO or NO_2 and H_2O. The nitrate salts for all the Ni, Cu, Sm and Co from coating and the magnets are soluble in water, where they have colours of green, blue, yellow and red, respectively. As shown in Figure 4.18, the kinetics of the elements dissolution is slow, where about 90 min was needed for the complete dissolution of the Ni. The presence of the magnet for that long time in the nitric acid solution increases the probability that a fracture in the coating layer would occur and the acid will attack the Sm and Co elements from the magnets instead of the coating, especially in the case of the presence of non-uniform coating layers. This situation occurred many times during our trials. Moreover, increasing the surface of the magnet would result in increasing the time required for the coating removal under the applied experimental conditions, as shown later for Sm_2Co_{17} magnets which have a volume of 0.19 cm^3 in comparison to 0.16 cm^3 for the used $SmCo_5$ magnets. The reaction with nitric acid is also accompanied with the production of NO and NO_2 gases which are known to have many health issues as being carcinogenic and coercive.

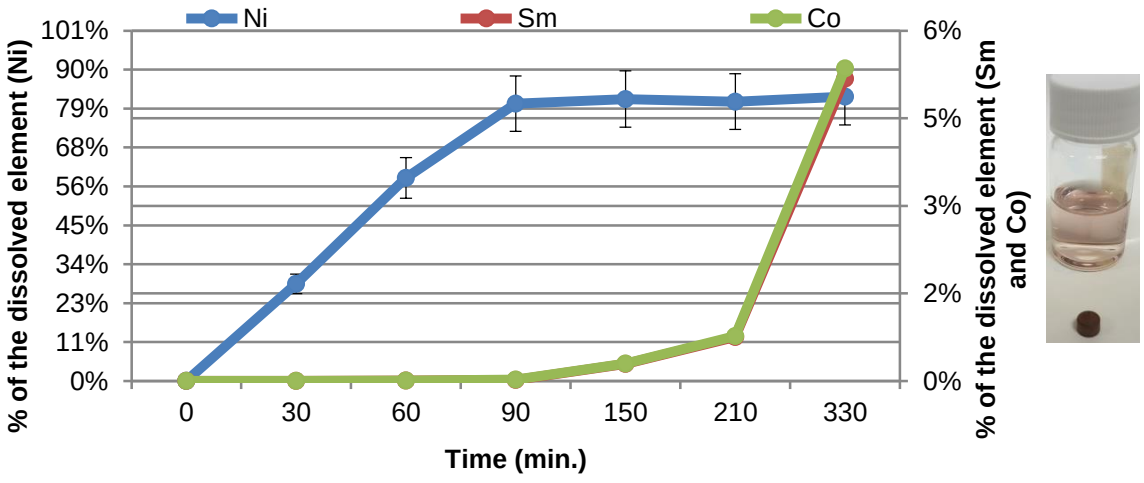

Figure 4.18: The dissolution of Ni, Sm and Co from $SmCo_5$ magnets by 2M HNO_3.

Consequently, other solutions for the coating dissolution of Br/organics were investigated to replace the mineral nitric acid. The Br/organic solutions were previously used efficiently for the leaching and dissolution of various elements, such as Cr, Al and Co [113]. For screening, five solutions of 1 vol.% Br with EG, DMF, ethanol, MeOAC and EtOAC were investigated by the reaction with the magnets for a fixed time of 20 min. Figure 4.19 shows that for DMF and ethanol, almost all the Ni and Cu elements were dissolved, with

the dissolution of 2% of the magnets' elements. The metals react with the bromine in the solution with the formation of metal bromide, while the organic phase acts as a coordinating agent of the ions and so it is expected that increasing the di-electric constant of the organic phase would lead to higher reaction rates and enhancing the elemental dissolution. The results were consistent with the previous expectation, except for EG, which has the highest polarity among the used organics. The previous can be related to the higher viscosity of EG of 16 mPa.s in comparison to other solutions, which is in the range of 0.36 mPa.s to 0.98 mPa.s. The high viscosity of the EG would result in decreasing the diffusion of the elements to form the bromide. The bromides of the Sm, Co, Cu and Ni have the colors of brown, bright green, greyish black and yellow brown, respectively.

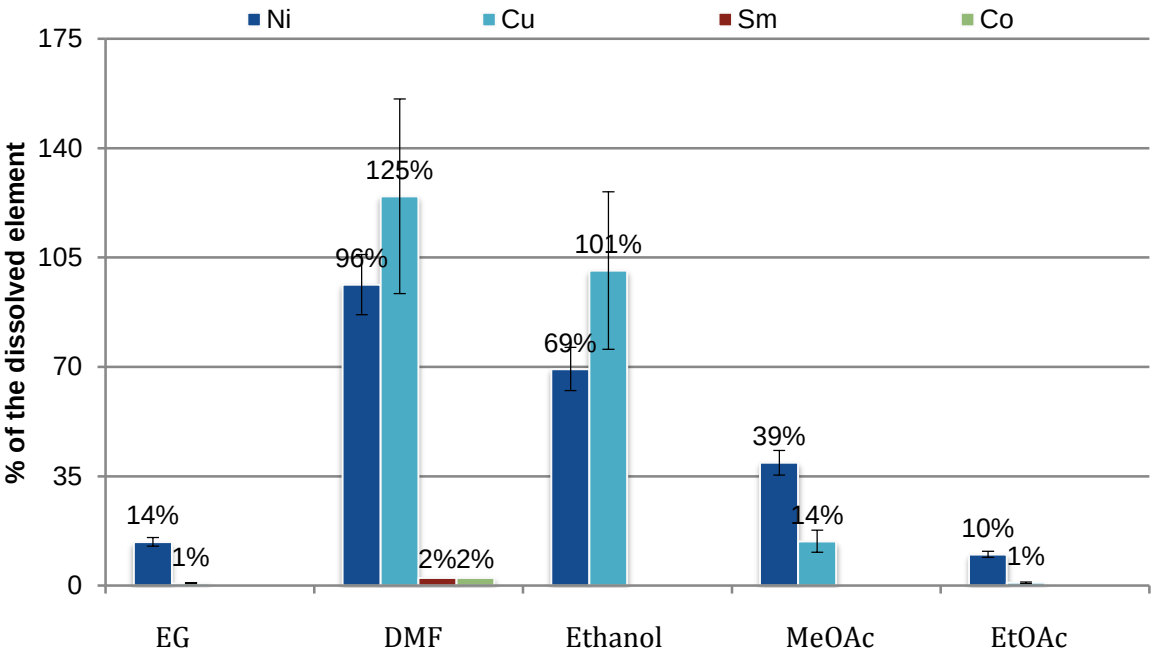

Figure 4.19: The dissolution of Ni, Sm, Co and Cu from $SmCo_5$ magnets by 1 vol.% Br_2/organic in 20 min reaction time. The solvents are arranged in terms of higher polarity from left to right.

Figure 4.20 shows an example for the coating layers being removed by the Br/organic reaction taken at different time intervals, the whole reaction time was 30 min. It is obvious how the coating layers are subsequently removed by using the solutions. Before the complete dissolution of the Ni layer (silver), the Cu layer (pinkish-orange) starts to appear, which is followed by the appearance of the third coating layer of Ni and then the surface of the magnet itself.

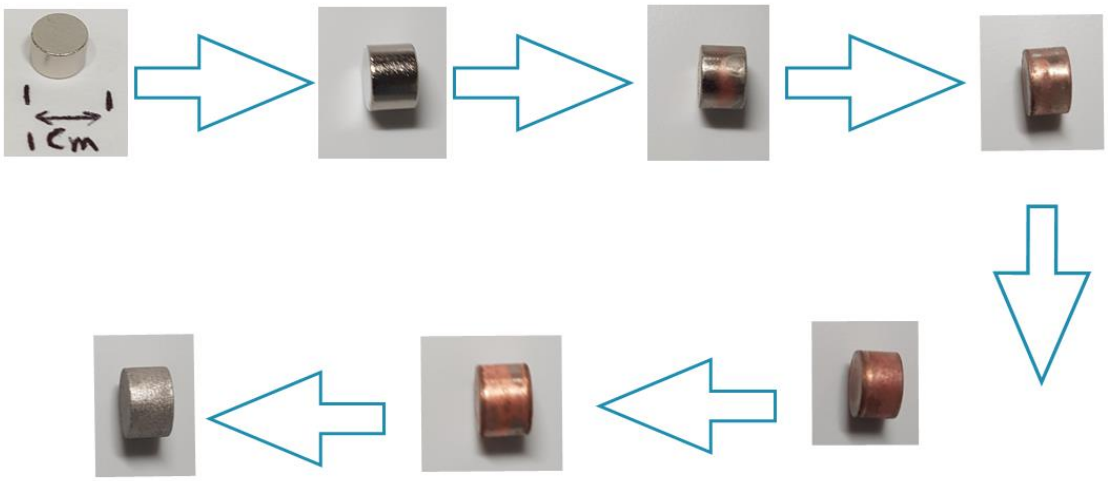

Figure 4.20: Coating dissolution by 1 vol.% Br_2/organic reaction, 30 minutes.

The kinetics of the dissolution of Br/ethanol, Br/DMF and Br/EG were also studied as shown in Figure 4.21, Figure 4.22 and Figure 4.23, respectively. For the complete dissolution of the coating elements on the magnets, 10-15 min were shown to be enough for the DMF solution, 20-25 min for the ethanol solution and at least 4 h in the case of the solution containing EG. Even though DMF is a faster solution, ethanol is recommended for the industrial application because of the health hazards related to the former as shown in appendix A. For both ethanol and DMF solutions, the amount of the dissolution of the magnets was shown to be lower than 1% even after 30 min of reaction.

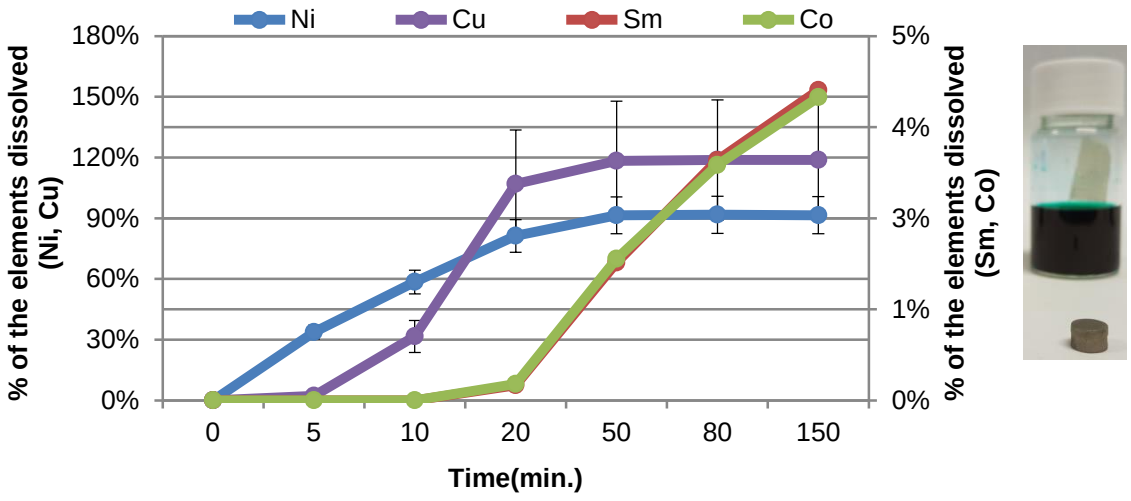

Figure 4.21: The dissolution kinetics of Ni, Sm, Co and Cu from coated $SmCo_5$ magnets by 1 vol.% Br_2/ethanol.

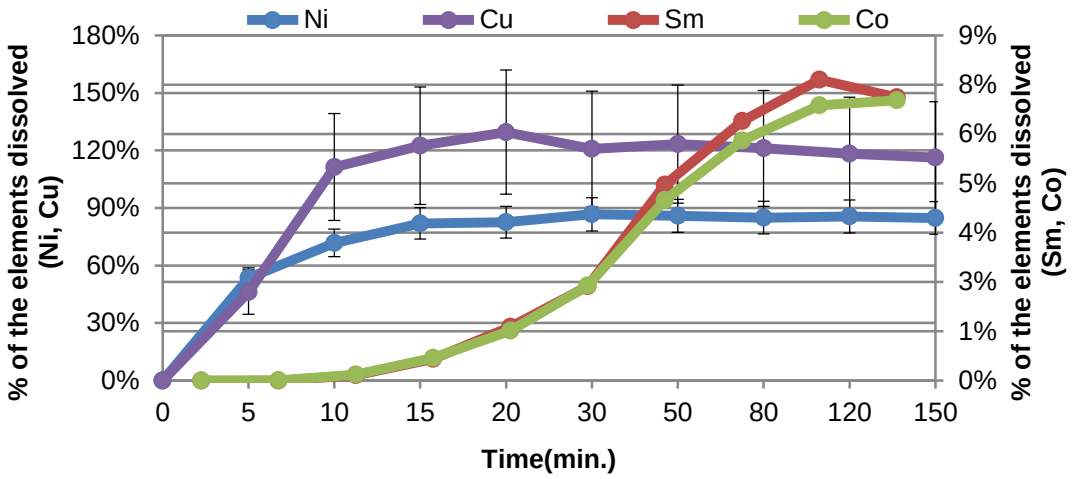

Figure 4.22: The dissolution kinetics of Ni, Sm, Co and Cu from coated $SmCo_5$ magnets by 1 vol.% Br_2/DMF.

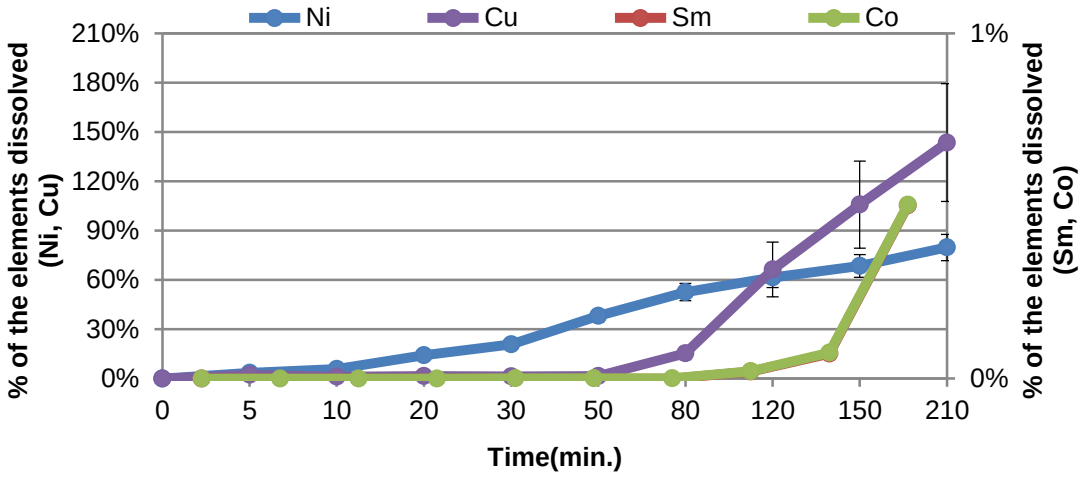

Figure 4.23: The dissolution kinetics of Ni, Sm, Co and Cu from coated $SmCo_5$ magnets by 1 vol.% Br_2/EG.

4.1.7 Properties of $SmCo_5$ with different Ni/Cu addition

In order to test the possibility of having traces of Ni and Cu from coating in the powder to be recycled and to study the effect of those trace impurities on the magnetic properties of the recycled magnets, $SmCo_5$ conventionally sintered magnets were prepared by adding a Ni/Cu (80 wt.%/20 wt.%) of an amount up to 4 wt.% and the influence on the magnetic properties was studied.

For all the samples with 0 wt.%, 0.5 wt.%, 1 wt.%, 2 wt.% and 4 wt.% Ni/Cu, the density was higher than 97% of the theoretical density. The oxygen content was also consistent, and was lower than 0.35 wt.%, which is admissible for the industrial production.

The demagnetization curves are shown in Figure 4.24. Table 4.4 shows the B_r, $(BH)_{max}$ and coercivity values for the magnets. Up to 2 wt.% Ni/Cu, the magnets showed to have good magnetic properties with a similar demagnetization behaviour. The measured $(BH)_{max}$ values were higher than 150 kJ/m³ and ${}_bH_c$ were higher than 640 kA/m. A very small increase in the B_r value from 0.92 T to 0.94 T by the increase in the Ni/Cu content up to 2% was observed, which might be due to the decrease in the Sm_2Co_7 phase content by Ni/Cu increase, as will be discussed in the next section. The presence of the high amount of Sm_2Co_7 in the 0 wt.% Ni/Cu also might be the reason for the small shoulder in its demagnetization curve. For the 4% Ni/Cu magnet, there was a significant decrease in the B_r value to 0.74 T, moreover, ${}_iH_c$ was decreased to lower than 150 kA/m with a very low $(BH)_{max}$ value lower than 24 kJ/m³, which is not suitable for the industrial application of the magnets.

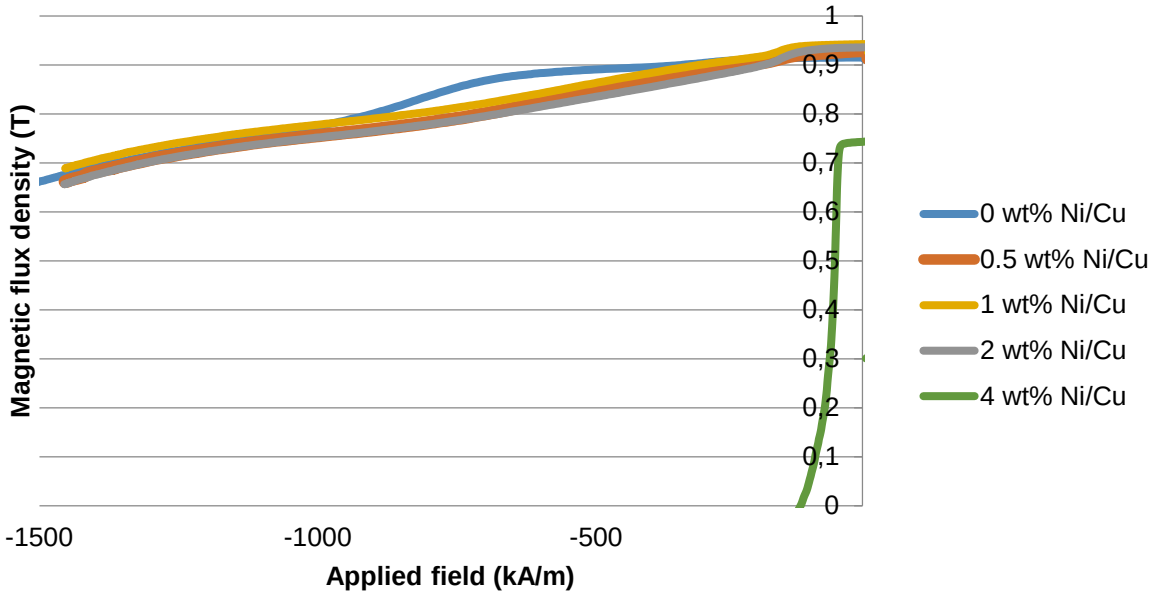

Figure 4.24: The demagnetization curves for the $SmCo_5$ magnets with 0-4 wt.% Ni/Cu content.

Table 4.4: The magnetic properties for the magnets with 0-4 wt.% Ni/Cu content.

	B_r [T]	$_iH_c$ [kA/m]	$_bH_c$ [kA/m]	$(BH)_{max}$ [kJ/m^3]
100 wt.% $SmCo_5$	0.92	>1500	691.8	175.1
99.5 wt.% $SmCo_5$ – 0.5 wt.% Ni/Cu	0.93	>1500	646.0	154.4
99 wt.% $SmCo_5$ – 1 wt.% Ni/Cu	0.94	>1500	660.1	159.3
98 wt.% $SmCo_5$ – 2 wt.% Ni/Cu	0.94	>1500	641.7	150.3
96 wt.% $SmCo_5$ – 4 wt.% Ni/Cu	0.74	132.8	101.3	23.98

The microstructures of the magnets were studied in order to understand the reason for the decrease in coercivity and magnetic properties for the magnets with Ni/Cu content higher than 2 wt.%. Fig. 4.25 shows the BSE images of the magnets with 0 wt.%, 0.5 wt.%, 1 wt.%, 2 wt.% and 4 wt.% Ni/Cu. Table 4.5, Table 4.6 and Table 4.7 show the EDX analysis for the phases in the magnets with 0 wt.%, 2 wt.% and 4 wt.%, respectively. For the magnets with 0-1 wt.% Ni/Cu, the microstructure is similar to the industrially produced $SmCo_5$ magnets as it is mentioned in the literature [62],[63],[64]. The magnets consist of the $SmCo_5$ matrix phase with a random distribution of Sm_2Co_7, Sm-rich phases, Sm-oxides and pores. The concentration of the Sm_2Co_7 phase (light-grey) in the microstructures of the magnets appears to decrease with increasing the Ni/Cu. The Sm_2Co_7 phase was not formed in the magnet with 2% Ni/Cu, however, this magnet was still showing to have good magnetic properties, similar to the samples with a lower Ni/Cu concentration. In some parts of the microstructure of the 2 wt.% Ni/Cu magnet, a new phase of very small fractions (dark grey phase) started to form at the grain boundaries. The distribution of this new phase was shown to increase with the increase in the Ni/Cu. Using the EDX, the composition of the phase has been measured in the sample with 4 wt.% Ni/Cu to be a Co-rich phase with a composition near Sm_2Co_{17}. The fraction of the phase was much higher for the magnet with 4 wt.% Ni/Cu and this is believed to be the reason for losing almost all the magnet's coercivity. It was concluded that the presence of the impurity phase at the grain boundaries and therefore the decrease in the pinning strength is the main reason for the coercivity drop for the magnets with 4 wt.% Ni/Cu.

The EDX analysis for the magnets with 2-4 wt.% Ni/Cu showed that increasing the concentrations of the two elements in the magnets is accompanied by an increase in their concentration in the main phase of $SmCo_5$ matrix. Either of the two elements was detected as forming separate identified phases with either Sm or Co and they only seem to replace some of the Co atoms in the crystal structure of the Sm/Co phases.

The XRD patterns for the samples with 0 wt.%, 1 wt.%, 2 wt.% and 4 wt.% Ni/Cu are shown in Fig. 4.26. It is shown that the peak for the Sm_2Co_7 phase disappeared for the samples with 2 wt.% and 4 wt.% Ni/Cu; as expected from the microstructure study. All other peaks were formed for all samples and they are related to the $SmCo_5$ matrix phase. Increasing the Ni/Cu concentration was accompanied by the presence of some peak shifts, which also confirms the fact of Co substitution in the $SmCo_5$ matrix which causes change in the crystal parameters and therefore peaks shift. As expected, due to the low concentration of the newly formed Sm_2Co_{17} phase in the samples, it was not possible to be detected by the XRD.

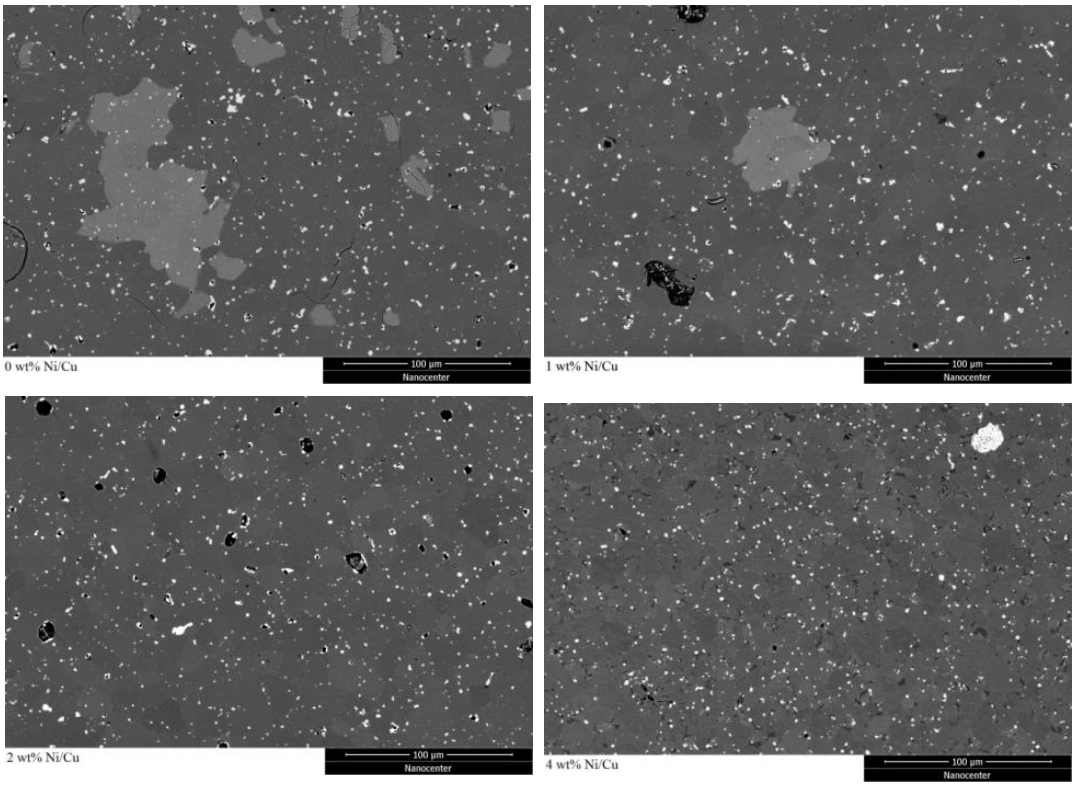

Figure 4.25: The BSE images for the sample with 0 wt.%, 1 wt.%, 2 wt.%, and 4 wt.% Ni/Cu from top left to bottom right, respectively.

Table 4.5: The EDX analysis for the phases in the sample with 0 wt.% Ni/Cu.

	Sm (at.%)	Co (at.%)	O (at.%)
The matrix phase	16.8	81.7	1.5**
The grey phase	22.4	75.9	1.8**
The white small spots*	35.7	11	53.3

Table 4.6: The EDX analysis for the phases in the sample with 2 wt.% Ni/Cu.

	Sm (at.%)	Co (at.%)	O (at.%)	Ni (at.%)	Cu (at.%)
The matrix phase	16.2	80.3	0.9**	2.3	0.3**
The white small spots*	30.7	17.0	52.0	0.3**	0**

Table 4.7: The EDX analysis for the phases in the sample with 4 wt.% Ni/Cu.

	Sm (at.%)	Co (at.%)	O (at.%)	Ni (at.%)	Cu (at.%)
The matrix phase	16	78	1.1**	4.2	0.7**
The dark grey phase	11.2	85.2	0.8**	2.4	0.4**
The white small spots*	36	5	58.5	0.4**	0.1**

* the phase size is small where it is expected that there is signal interference from the surrounding phases

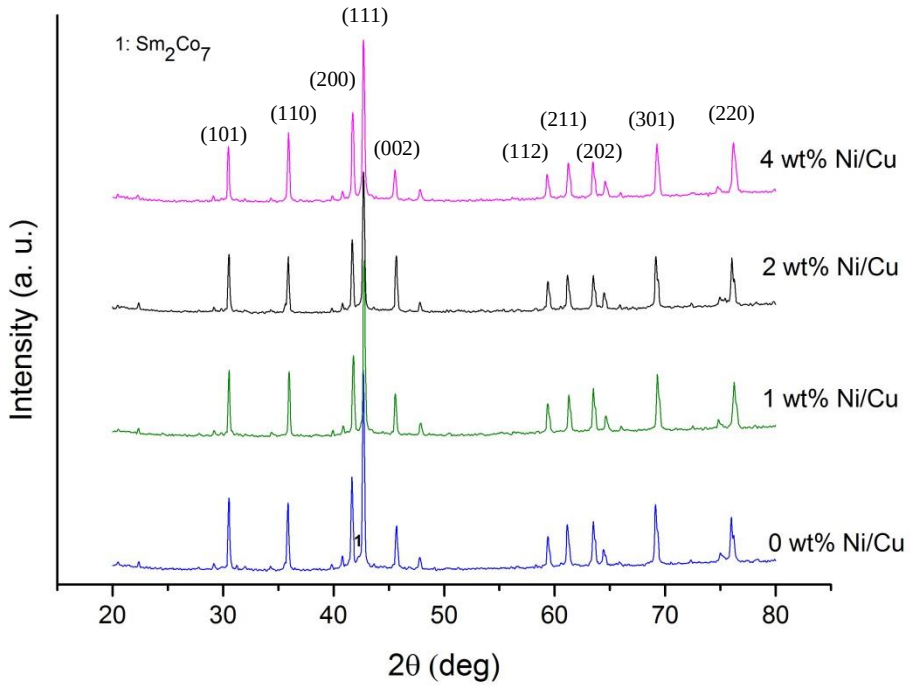

Figure 4.26: XRD patterns for the sample with 0 wt.%, 1 wt.%, 2 wt.% and 4 wt.% Ni/Cu.

4.1.8 Other ways to recycle $SmCo_5$ magnets: strip casting

After the strip casting of the $SmCo_5$ sintered magnets, only 3 kg of strip-cast material was recovered out of 8 kg starting material. This is due to the formation and the discarding of the oxide layer and the stickiness of the molten slag to the walls of the crucible and the tundish as shown in Figure 4.27. The oxygen content of the final strip cast material was measured to be lower than 0.02 wt.%, in comparison to 0.37 wt.% in the starting material.

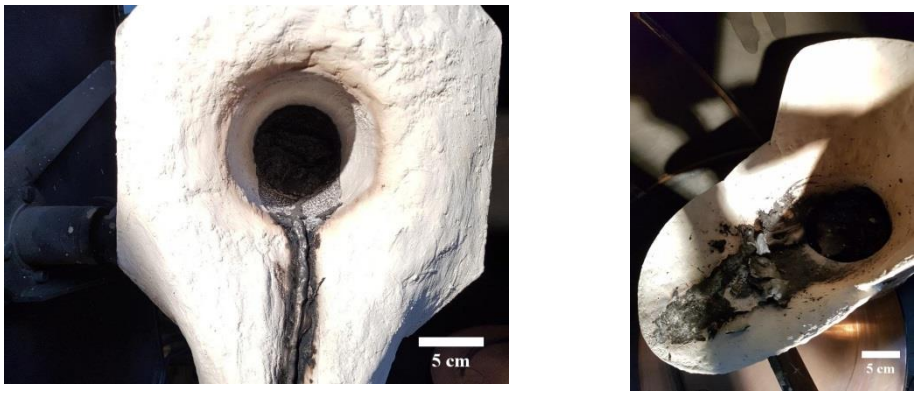

Figure 4.27: The residual molten $SmCo_5$ alloy and its oxide formation after strip casting.

The XRD and microstructure studies of the strip-cast material are shown in Figure 4.28 and Figure 4.29, respectively. The phases formed after strip casting are similar to the ones from the book-mould casting and sintering with the formation of $SmCo_5$ and Sm_2Co_7 phases. Contrary to book-mould cast and sintered $SmCo_5$, where the Sm rich phases are

formed randomly in the microstructure, in strip casting the Sm_2Co_7 phase is formed continuously throughout the grain boundary of the material. Moreover, strip ocasting resulted in the formation of continuous fine grained $SmCo_5$ of about 10 μm, in comparison to 20-30 μm for sintered material and more than 50 μm in the book-mould cast one.

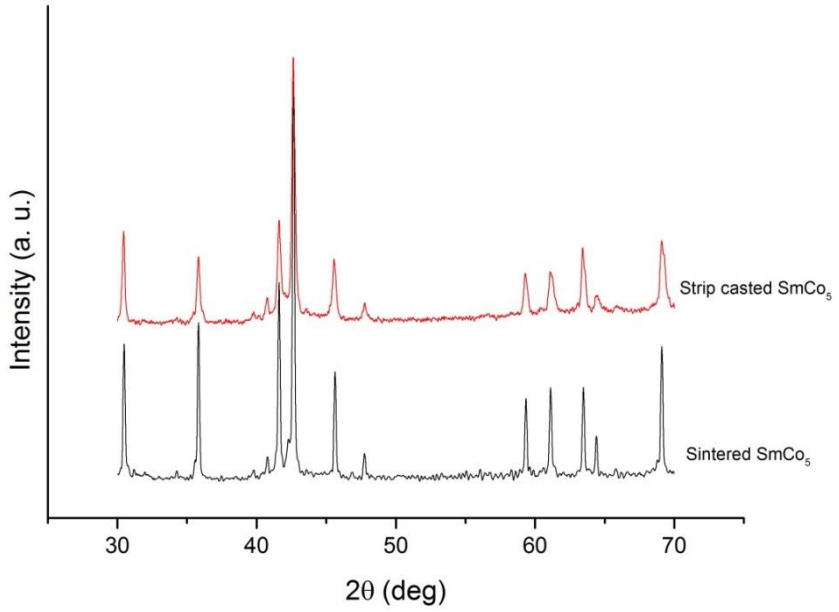

Figure 4.28: The XRD patterns showing the similarity of the phases' composition for the sintered and the strip-cast $SmCo_5$ material, peak identifications in Figure 4.2.

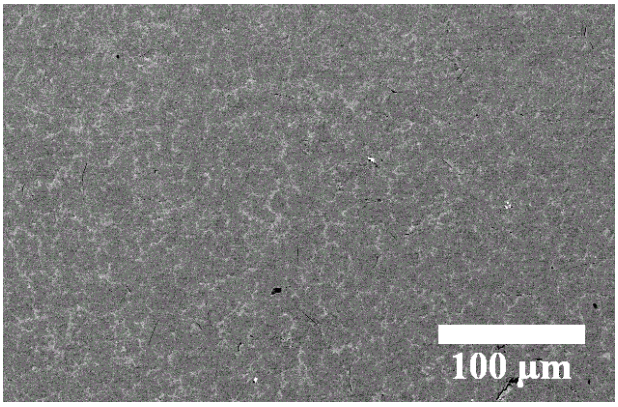

Figure 4.29: BSE of the strip cast produced from sintered $SmCo_5$ magnets, the microstructure composed of fine $SmCo_5$ matrix grains surrounded by Sm_2Co_7 phase.

Due to the low recovery of the material after applying strip casting under the current applied conditions, it was not interesting for us to continue the recycling scheme. However, further experiments are planned to control the strip casting setup to increase the material recovery. It is expected that the magnetic properties of the magnets produced from the crushed and milled strip-cast material will be as good as the ones from the HD route due to the presence of a very fine grain structure. Moreover, HD can also be applied on the strip-cast material. It is expected that when applying HD on the strip-cast material, the hydrogen will react with the Sm-rich phases surrounding the fine grained $SmCo_5$ matrix, with the production of very fine decrepitated powder of a size of less than 50 μm, which will need minimal or no milling before the magnets production.

4.2 Sm_2Co_{17}

4.2.1 HD of as-cast Sm_2Co_{17} alloys

Two as-cast alloys having a chemical composition similar to the industrial produced Sm_2Co_{17} magnets (~25.4 wt.% Sm) were used. One of the alloys with a higher Sm content of 29.8 wt.% and the other with a lower Sm content of 24 wt.%, were tested for the HD. The exact chemical compositions for the two alloys are mentioned in Table 3.1. The densities of the used alloys were more than 98 wt.% of the theoretical densities. The alloys with the higher Sm content showed to be decrepitated easily under a pressure of 1 bar at room temperature for 3 h. The alloy with a lower Sm content required at least 4 bar of hydrogen to start the decrepitation. The particle size of the decrepitated powders was less than 400 µm. The microstructures of the two alloys are shown in Figure 4.30. The XRD patterns for the alloys before and after decrepitation are shown in Fig 4.31. The dark-grey matrix of the alloys was measured to be similar in the two alloys; 25 wt.% Sm, 46.98 wt.% Co, 18.77 wt.% Fe, 3.45 wt.% Cu and 2.41 wt.% Zr for the high Sm alloy and 22.6 wt.% Sm, 52.7 wt.% Co, 20.0 wt.% Fe, 3.66 wt.% Cu and 2.05 wt.% Zr for the low Sm content alloy. The light-grey phase surrounding the matrix was shown to have a higher Sm content of an average of 30 wt.% and a mixture of two phases, rich in Cu and Zr for the two alloys as reported very recently by Zhang et al. [114]. The decrepitation process starts with hydrogen absorption of the light-grey phase, rich in Sm. This explains the fact that the alloy with high Sm is easier to be decrepitated as the concentration of the light-grey phase was higher in that alloy. After decrepitation, the peaks of the Sm-rich phase decreased with the appearance of oxides. Video 2 shows the decrepitation for the high Sm alloy.

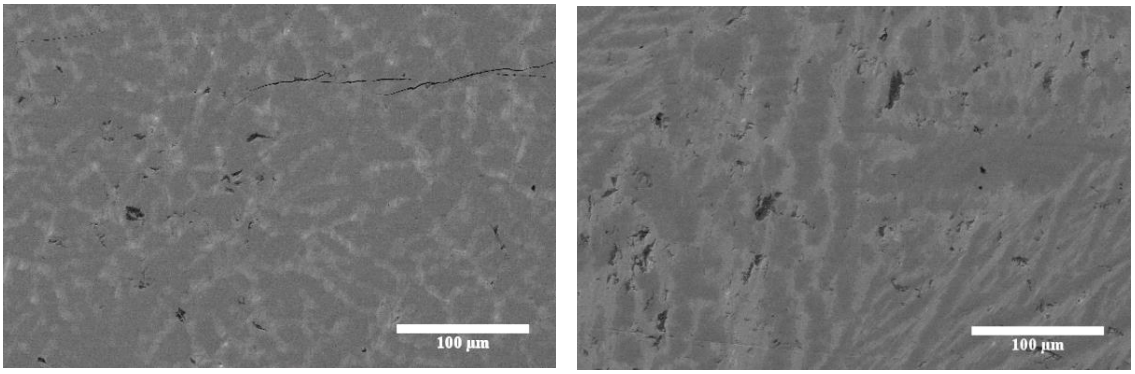

Figure 4.30: BSE images for the as-cast alloys with a composition close to industrial Sm_2Co_{17} magnets, rich in Co (left) and rich in Sm (right).

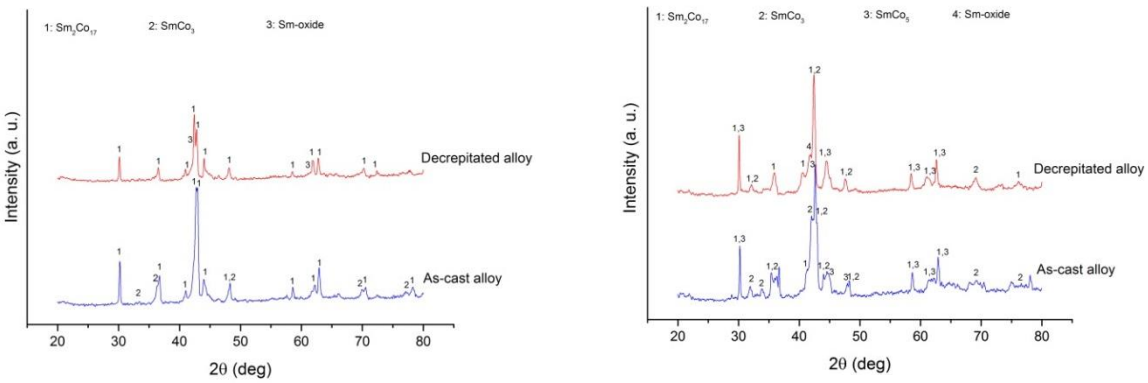

Figure 4.31: XRD patterns for the Sm_2Co_{17} alloys; rich in Co (left) and in Sm (right), before and after decrepitation.

4.2.2 HD for the recycling of Sm_2Co_{17} magnets: conventional sintering

Sm_2Co_{17} magnets contain the lowest REE content among REE-permanent magnets of 25 wt.% in comparison to 36 wt.% for $SmCo_5$ and about 31 wt.% for Nd-Fe-B. This is translated in the microstructure of the conventionally sintered Sm_2Co_{17} magnets, as they do not contain any rich REE phases, which is the case for the $SmCo_5$ and Nd-Fe-B magnets. This would mean that more severe conditions of HD are needed to be applied for Sm_2Co_{17} magnet to absorb hydrogen, as the hydrogen absorption is usually initiated by the REE-rich phases; as explained in the literature chapter.

4.2.2.1 Decrepitation by using the stationary equipment and the effect of the composition of the magnets on the HD process

As a first step, it was useful to study the effect of the change of the chemical composition of the sintered Sm_2Co_{17} magnets on the hydrogen absorption affinity. Seven magnets having a chemical composition close to the industrially produced Sm_2Co_{17} were prepared. They were sintered to be compared in terms of HD and magnetic properties. The exact chemical compositions of the industrially produced (original) and the other prepared magnets are shown in Table 4.8 and their demagnetization curves in Figure 4.32.

Table 4.8: Decrepitation of Sm_2Co_{17} magnets with different compositions (wt.%).

	No.	Sm	Co	Cu	Zr	Fe	10 bar - room temp. - 1day Or 5 bar - 200 °C - 5 h
Original		25.6	49.1	5.4	2.8	17.1	No effect
With more Sm	1	29.1	46.7	5.1	2.8	16.2	Slightly decrepitated
With more Fe	2	25.2	48.7	5.3	2.9	17.9	No effect
	3	24.9	48.2	5.3	2.8	18.7	No effect
With more Fe, less Zr	4	25.1	49.1	5.5	2.2	18.1	No effect
	5	24.8	48.5	5.5	2.1	19.1	Slightly decrepitated
With more Fe, more Cu , less Zr	6	24.8	48.4	5.7	2.1	19.0	Decrepitated
With more Fe, more Sm , less Zr	7	25.6	48.0	5.4	2.1	18.9	Decrepitated

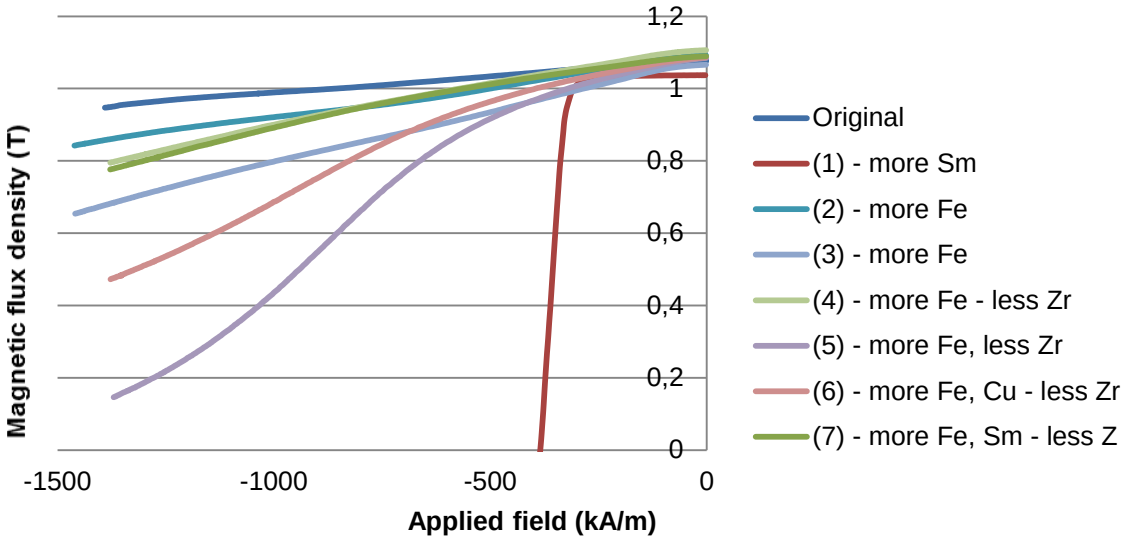

Figure 4.32: Demagnetization curves for the Sm_2Co_{17} magnets with different compositions.

The conditions applied as trial for the decrepitation were 10 bar, room temperature for 1 day or 5 bar, 5h at 200 °C. As shown in Table 4.8, only two compositions were fully decrepitated by the applied conditions. Also the magnets with more Sm (no. 1) and more Fe-less Zr (no. 5) were shown to be partially decrepitated with the production of smaller particles, while there were still some large particles present in the decrepitation products. However, when studying the magnetic properties of all the magnets with different chemical compositions against the serious production original one, all of them were showing much worse magnetic properties as shown in Figure 4.32 and as it is known from literature that a very small change in any element in the composition of the Sm_2Co_{17} magnets or in the sintering regime would lead to a change in the fine structure of the magnets, which change the properties of the magnets. A choice between having good magnetic properties magnets, which are hard to be decrepitated and recycled, or lower magnetic properties magnets, which are easier to be recycled, has to be made. We continued the study with the HD of the industrially produced magnet (original), as it is the most visible for the real application for the magnets in the market even if it needs more severe conditions for the HD.

4.2.2.2 Decrepitation mechanism and the properties of the decrepitated powder

The required decrepitation conditions for the complete decrepitation of the industrially produced magnets were 20 bar, room temperature for 2 days. The coarse-grains and fine-cellular microstructures of the magnets are shown in Figure 4.33. The coarse-grains microstructure consists of the matrix phase with a composition close to $Sm(Co_{0.575}Fe_{0.21}Cu_{0.058}Zr_{0.021})_{8.5}$ (similar to the starting composition) with Sm-oxide white phases distributed randomly. A third phase rich in Zr was observed at higher magnification, having a composition close to $ZrCo_{0.13}Fe_{0.07}$. The Zr-rich phase was observed as contamination in all the conventionally sintered Sm_2Co_{17} magnets as reported by Saravanan et al. [39]. There will be no discussion on this phase as it is reported as contamination and was observed in all the conventionally sintered Sm_2Co_{17} magnets reported in this dissertation, with the same percentage in the microstructure of around 0.5 %. The fine-cellular structure of the magnets consists of $Sm_2(Co,Fe)_{17}$ cell interior (rhombohedral), $Sm(Co,Cu)_5$ cell boundary (hexagonal) and a third phase of $Zr(Co,Fe)_3$ perpendicular to the image plane. $Sm_2(Co,Fe)_{17}$ cell interior was measured to have an average size of 140 nm. The $Sm(Co,Cu)_5$ cellular boundary in the fine structure is the one

which starts the hydrogen absorption of the magnet as it has the highest Sm content in comparison to the other phases. The particle size of the powders after decrepitation was measured to be 250 μm, however the particles were friable and also showed to contain about 10% of very fine powder of less than 32 μm, which can be due to the hydrogen absorption of the cell boundary and the disintegration of the $Sm_2(Co,Fe)_{17}$ cell interior.

4.2.2.3 Preparation of recycled magnets and their properties

The decrepitated powder was milled in a nitrogen atmosphere via jet-milling to a particle size less than 20 μm. The oxygen content after decrepitation and milling was 0.43 wt.% in comparison to 0.24 wt.% in the original magnets. After milling, four different compositions were prepared for the production of sintered recycled magnets without and with the addition of elements of Sm and Cu or fresh Sm_2Co_{17} powder produced by the industrial way of casting and milling, as follows:

- 100% Recycled (Recycled),
- (98.3 %) Recycled + (1.7 %) Sm (Recycled+Sm),
- (98.2 %) Recycled + (1.2 %) Sm + (0.6 %) Cu (Recycled +Sm+Cu),
- 50% Recycled + 50% fresh (Recycled +Fresh).

The reason for choosing those exact compositions and their properties are discussed in the next paragraph.

Figure 4.34 and Table 4.9 show the magnetic properties of the recycled magnets in comparison to the original one before decrepitation, the oxygen content and the density values are also shown. The recycled magnets with only recycled powder (Recycled) showed big deterioration of B_r, $_bH_c$ and $(BH)_{max}$ of 1.03 T, 419.5 kA/m and 161.6 kJ/m^3, respectively, in comparison to 1.10 T, 816.98 kA/m and 226.9 kJ/m^3, respectively, for the original magnets. This can be explained due to the increase in the oxygen content of 0.63 wt.%, in comparison to 0.24 wt.% for the original, with the formation of non-continuous large $Sm_2(Co, Fe)_{17}$ cell interior (average size of 300 nm) and thin inhomogeneous cell boundary $Sm(Co,Cu)_5$ phase as shown in Figure 4.35. Adding milled Sm to the recycled powder (to produce Recycled +Sm) showed to have the effect of increasing the magnetic properties of the Recycled+Sm magnet, as the added Sm compensate for the Sm loss due to the oxidation during the recycling process. By the addition of Sm, the properties of the produced magnet showed to have enhanced B_r, $_bH_c$ and $(BH)_{max}$ of 1.07 T, 739.6 kA/m and 198.2 kJ/m^3, respectively. But as the Recycled+Sm magnet showed to have less coercivity and a more tilted demagnetization curve than the original magnet and as it is known from literature that the main function of Cu in the magnet is to increase the coercivity by enhancing the pinning of the $Sm(Co,Cu)_5$ phase, a third composition was prepared by replacing some of the added Sm with milled Cu to the previous magnet (Recycled+Sm+Cu). The Recycled+Sm+Cu showed to have as good magnetic properties as for the original magnet, even with the high oxygen content of 0.7 wt.%. Another successful recycling composition was to mix fresh milled Sm_2Co_{17} powder with the recycled milled powder (Recycled+Fresh). The addition of fresh powder results in the decrease in the oxygen content to 0.51 wt.% and increase of the metallic elements required for enhancing the magnetic properties, which results in producing a recycled magnet with a potential for industrial applications as it shows to have good magnetic properties with similar values to the industrially produced magnets.

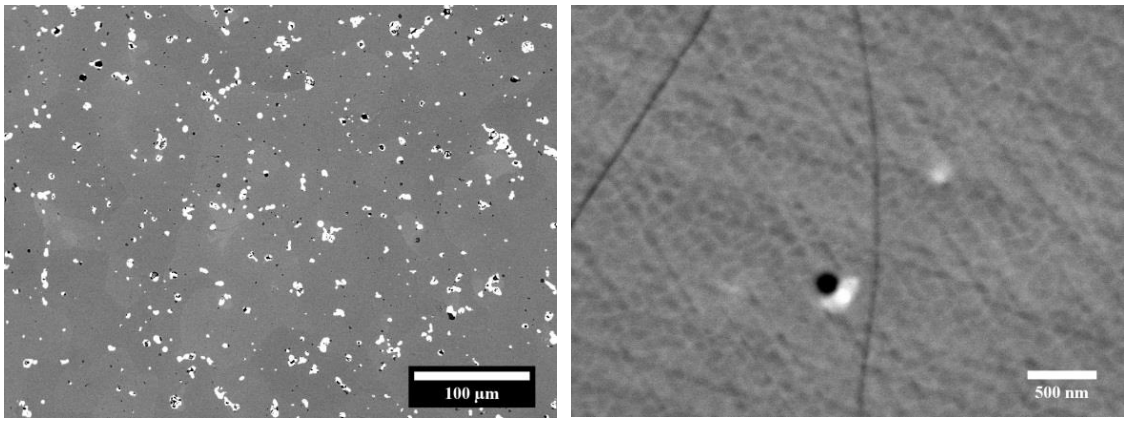

Figure 4.33: The coarse-grains (right) and the fine-cellular (left) microstructure for the original Sm_2Co_{17} sintered magnets used for recycling. The grain structure is mainly composed of the matrix phase (composition close to $Sm(Co_{0.575}Fe_{0.21}Cu_{0.058}Zr_{0.021})_{8.5}$) with Sm–oxides. The fine microstructure has cellular structure of $Sm_2(Co, Fe)_{17}$ cell interior and $Sm(Co,Cu)_5$ cell boundary.

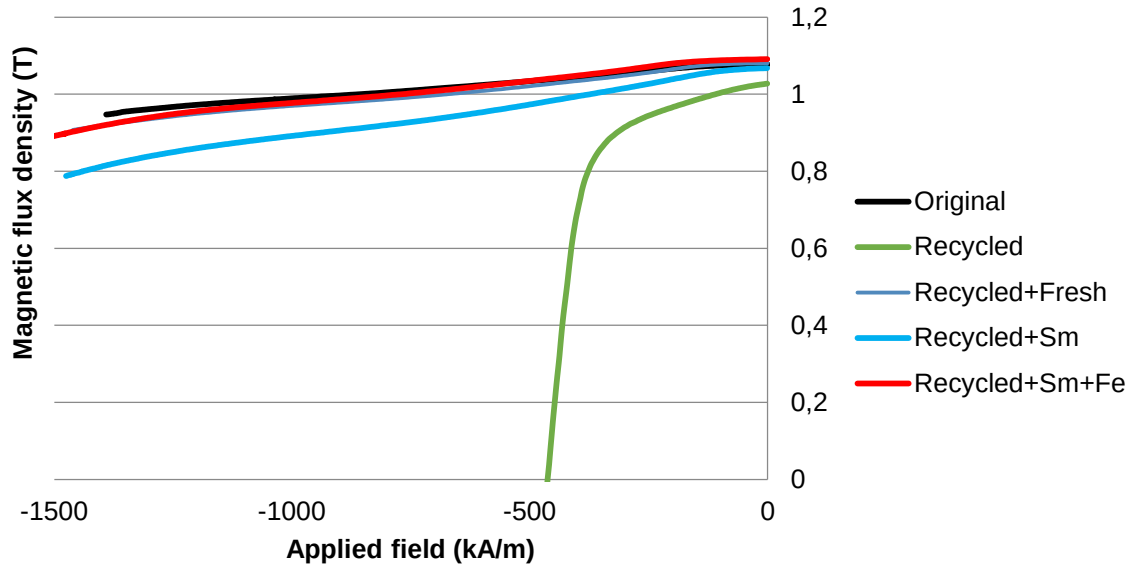

Figure 4.34: Demagnetization curves for the Sm_2Co_{17} magnets before and after recycling by HD.

Figure 4.35 shows the coarse-grains and fine-cellular microstructures for the Recycled, Recycled+Sm, Recycled+Sm+Cu and Recycled+Fresh magnets. The coarse-grain microstructure of all samples shows to contain the same phases as the matrix phase (composition close to $Sm(Co_{0.575}Fe_{0.21}Cu_{0.058}Zr_{0.021})_{8.5}$) with Sm–oxides as measured by EDX. As explained, for the Recycled magnet, there was inhomogeneous formation of the $Sm(Co,Cu)_5$ phase with a large cell phase (300 nm) in comparison to 140 nm for the original magnet (Figure 4.33); with a negative effect of the properties of the former. For the Recycled+Sm sample, the size of the cell decreased to 250 nm and more homogenous $Sm(Co,Cu)_5$ was formed. Moreover with the Cu addition, a more uniform cellular structure

with a more defined cell boundary phase and smaller cell interior of as an average as little as 130 nm was formed. The Recycled+Fresh magnet was showing to have a fine-cellular microstructure, similar to the original and Recycled+Sm+Cu samples with an average cell interior of 180 nm. The previous enhancement in the microstructure by the Sm, Cu and fresh powder addition explains the previous trend of enhancing the magnetic properties of the recycled magnets; putting into consideration that the formation of homogeneous cell boundary with a small cell interior size of less than 200 nm is a key factor for producing high coercivity magnets as described in Chapter 2. This explains the lower magnetic properties of the Recycled and Recycled+Sm magnets.

Table 4.9: Magnets properties before and after recycling of Sm_2Co_{17} by HD.

	B_r [T]	iH_c [kA/m]	$_bH_c$ [kA/m]	$(BH)_{max}$ [kJ/m³]	Oxygen (wt.%)	ρ [g/cm³]
Original	1.10	>1500	8.17.0	226.3	0.24	8.34
Recycled	1.03	462.7	419.5	161.6	0.63	8.31
Recycled+Sm	1.07	>1500	739.4	198.2	0.70	8.33
Recycled+Sm+Cu	1.09	>1500	793.7	218.3	0.70	8.35
Recycled+Fresh	1.08	>1500	786.3	212.8	0.51	8.32

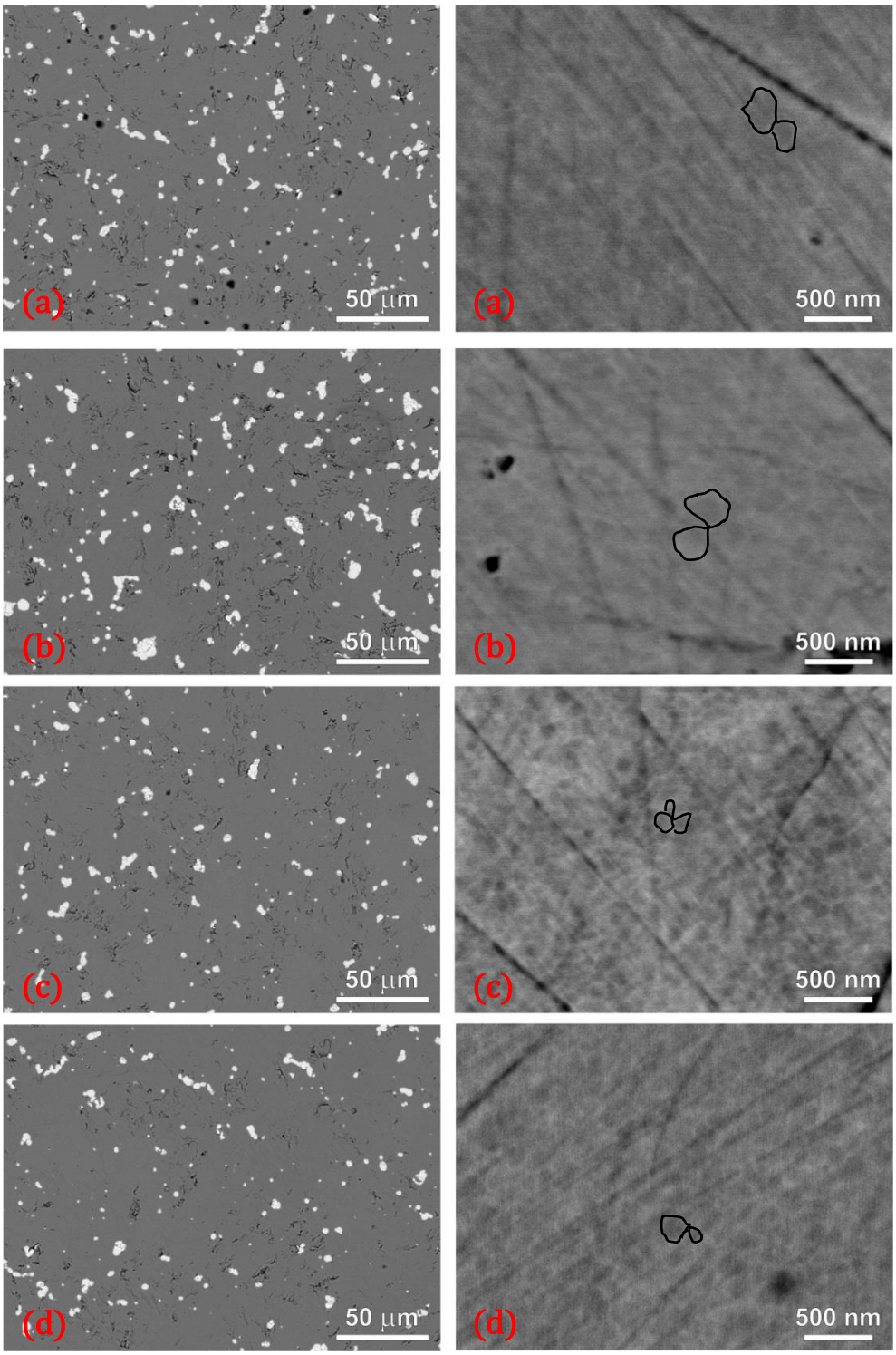

Figure 4.35: The coarse-grains (left) and the fine-cellular (right) microstructure for the recycled Sm_2Co_{17} magnets. From top to bottom are: Recycled (a) , Recycled+Sm (b), Recycled+Sm+Cu (c) and Recycled+Fesh (d). The coarse-grains and cellular structures are similar to the original magnet (Figure 4.33) with a different cell interior size.

4.2.3 SPS sintering for the decrepitated powder

The milled recycled decrepitated Sm_2Co_{17} powder with the addition of 1.2 wt.% Sm and 0.6 wt.% Cu (Recycled+Sm+Cu) was used for the production of SPS magnets, as this composition was shown to produce good magnetic properties when using the conventional sintering route.

Sintering temperatures of 800 °C, 850 °C, 900 °C, 950 °C, and 1000 °C were applied. The magnetic properties and the densities of the produced magnets after SPS sintering and after applying heat treatment (850 °C for 8 h) for the sintered magnets are shown in Table 4.10. The densities of all the produced magnets were less than 96% of the theoretical density of the sintered magnets, even by applying a sintering temperature of 1000 °C, which is very high for SPS applications. For $SmCo_5$ magnets, 950 °C was sufficient to densify the magnets by SPS. The magnetic properties of both only sintered magnets and magnets sintered followed by heat treatment were also very low. The maximum achieved $_iH_c$ was only 192.6 kA/m, for the heat-treated SPS samples from the 900 °C experiment. This is in comparison to >1500 kA/m for the recycled conventionally sintered magnet having the same composition.

Table 4.10: Density, oxygen content and magnetic properties of the SPS-ed samples sintered at 800-1000 °C. The properties of the magnets are also shown after applying the heat treatment (HT) cycle.

Sintering Temp	B_r [T]	$_bH_c$ [kA/m]	$_iH_c$ [kA/m]	$(BH)_{max}$ [kJ/m^3]	ρ [g/cm^3]
800 °C	0.265	97.85	158.58	7.15	6.14
800 °C (HT)	0.286	107.7	191.2	8.4	
850 °C	0.245	82.49	123.8	5.59	6.42
850 °C (HT)	0.301	108	184.9	9.1	
900 °C	0.323	79.05	98.56	8.12	7
900 °C (HT)	0.368	124	202.3	13	
950	0.364	76.52	80.71	9.42	7.5
950 °C (HT)	0.416	125.8	189.7	15.4	
1000 °C	0.397	68.48	76.54	9.54	8.07
1000 °C (HT)	0.445	129.5	192.6	17.1	

To understand the reason for the deterioration in the magnetic properties for the SPS-ed samples, the BSE of the samples sintered at 950 °C and 1000 °C after heat treatment are shown in Figure 4.36. The magnets consist of many phases as shown in Table 4.11, which is different from the magnets from the conventional sintering route, which only have the matrix and Sm-oxide phases. This formation of a multi-phase material hinders the formation of the fine-cellular structure which is essential for the production of high coercivity magnets. This can be explained as the sintering mechanism in SPS involves only the surface of the particle with no contribution from the bulk of the powder. As only the surface of the powder will react in the SPS, this means that the elemental diffusion from the bulk of the powder to form the cellular structure would not happen. For Sm_2Co_{17}

magnets to show good magnetic and mechanical properties, elemental diffusion is necessary from the surface and the bulk of the powder for the formation of the cellular microstructure. This explanation is supported with the presence of chocks of Cu- and Sm-rich phases in the microstructure of the SPS-sintered magnets; due to the incomplete solubility of the added Cu and Sm during the sintering step, with the production of low density and magnetic properties magnets. A pre-heat treatment step for the decrepitated powder might be needed before the SPS in order to regenerate the fine-cellular microstructure.

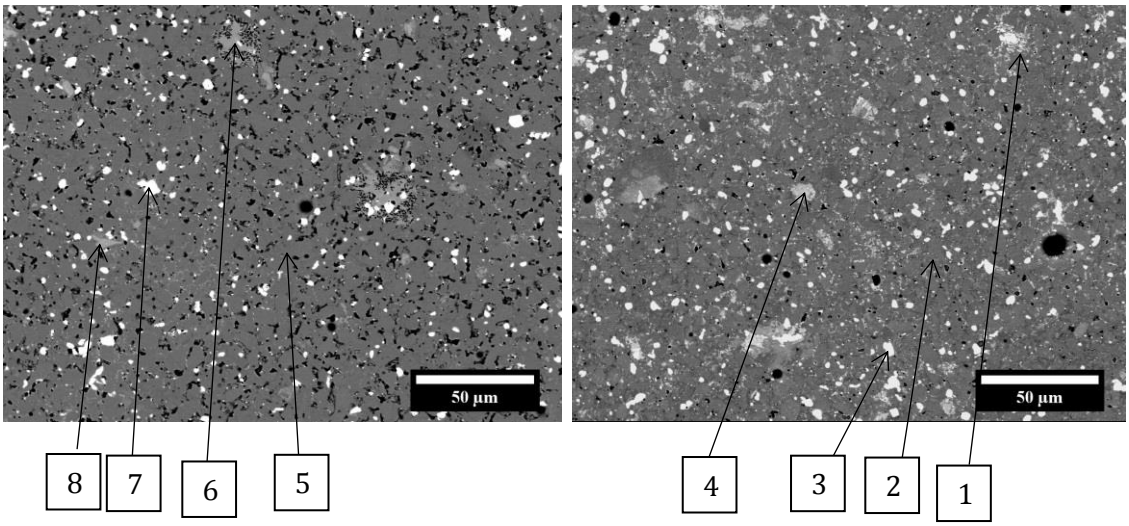

Figure 4.36: The BSE of the SPS-ed samples from the 950 °C (left) and 1000 °C (right) experiments after heat treatment. The samples showed to be composed of many phases in contrast to the conventionally sintered magnets (Figure 4.33).

Table 4.11: EDX analysis in wt.% for the phases formed during the SPS of the recycled Sm_2Co_{17} (Recycled+Sm+Cu) at 950 °C and 1000 °C, as shown in Figure 4.36.

Spot no (sintering temp.)	Sm	Co	Fe	Cu	Zr	O
1 (1000 °C)	30.70	41.66	10.71	16.17	1.11	0.95
2 (1000 °C)	23.25	53.26	19.71	2.82	1.52	1.01
3 (1000 °C)	83.37	2.45	1.49	0.13	0.00	17.16
4 (1000 °C)	26.05	50.20	16.44	4.62	2.60	0.87
5 (950 °C)	24.37	49.45	17.22	6.76	2.78	0.80
6 (950 °C)	33.16	27.28	4.54	34.47	0.53	0.66
7 (950 °C)	84.48	1.49	1.09	0.16	0.00	16.99
8 (950 °C)	33.02	42.86	8.44	10.61	6.51	0.69

4.2.4 Polymer-bonded recycled Sm_2Co_{17} (anisotropic)

The decrepitated powders used for the preparation of polymer-bonded magnets were produced by the decrepitation of the original sintered Sm_2Co_{17} magnets at 20 bar, 2 days at room temperature in the stationary equipment. Only the size fraction of <125 µm was used, which represents about 20% of the decrepitated powder by applying the mentioned conditions. Figure 4.37 shows the demagnetization curve of the magnet and Table 4.12 shows their B_r, coercivity and $(BH)_{max}$. Magnet's density of 5.2 g/cm^3 was achieved which is about 75% of the theoretical calculated density based on the used solid and polymer powders volume fraction. The lower achieved density is basically due to the inefficient coating and packing of the solid powder by the polymer binder due to the absence of any applied pressure during the final heating step, as it was the case for $SmCo_5$. Considering only the solid fraction of the 75% dense polymer-magnets, of which 80% by volume is solid, and as the Sm_2Co_{17} sintered magnets have a B_r of 1.1 T, it means that in case of perfect alignment of the magnetic powder, the theoretical B_r of the polymer-bonded magnet would be 0.66 T. The B_r from the produced magnet was 0.58 T which is 90% of the theoretical value. The magnets were also shown to have a high a $_iH_c$ value of more than 1500 kA/m and $(BH)_{max}$ of 56 kJ/m^3. The magnetic properties of the Sm_2Co_{17} bonded magnets are also measured at 80 °C, as shown in the previous figure and table. As expected, there was only a small change in the magnetic properties of the magnet at high temperature as the polymer-bonded magnet itself was prepared in air at a temperature of 200 °C.

Table 4.12: The magnetic properties of the polymer-bonded Sm_2Co_{17} (recycled) at room temperature and 80 °C.

Measuring temperature	B_r [T]	$_bH_c$ [kA/m]	$_iH_c$ [kA/m]	$(BH)_{max}$ [kJ/m^3]
Room Temp.	0.584	385.3	>1500	56
80 °C	0.572	371.3	>1500	53

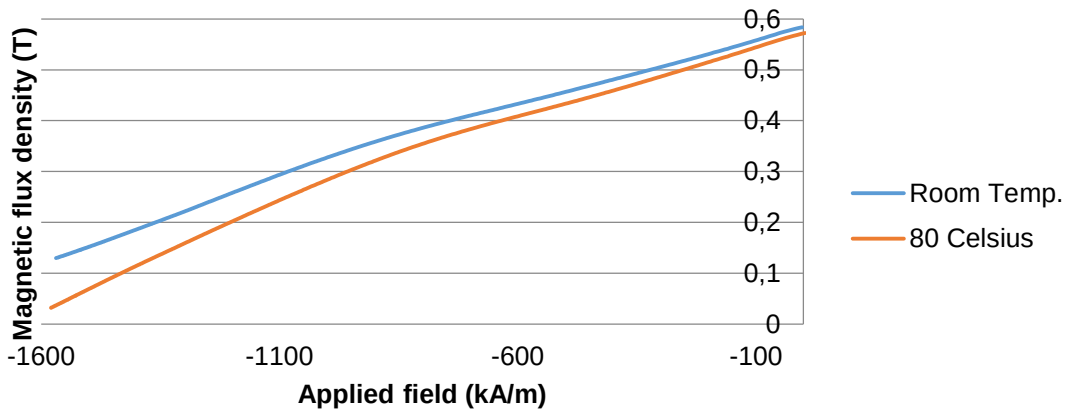

Figure 4.37: Demagnetization curves for the polymer-bonded Sm_2Co_{17} magnets produced from the decrepitated powder, measured at room temperature and 80 °C.

Figure 4.38 shows the BSE images of the Sm_2Co_{17} bonded magnets. The solid powder is immersed in the polymer binder, where white oxides are clearly visible on large powder particles.

When compared to one of the industrially produced polymer-bonded Nd-Fe-B magnets (isotropic) from injection moulding, having B_r of 0.55 T, $_iH_c$ less than 1000 kA/m and $(BH)_{max}$ around 55 kJ/m^3, the produced Sm_2Co_{17} polymer-bonded magnets in this study are attractive for industrial application. The latter claim is also supported by the use of recycled powder and the simplicity of the preparation method for the magnets, as all the steps for the preparation were done in atmospheric air without the need of protective atmosphere or expensive instruments as it is the case for injection or compaction moulding.

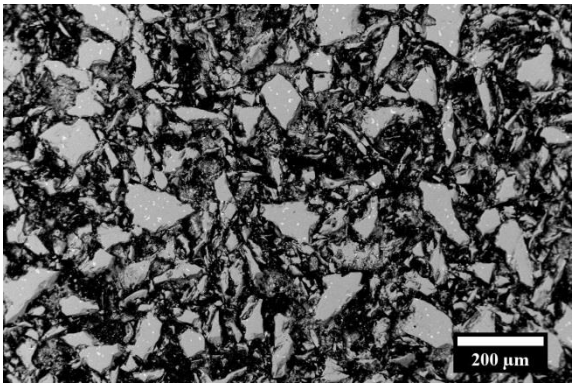

Figure 4.38: BSE of the polymer-bonded Sm_2Co_{17} magnets produced from the decrepitated powder.

4.2.5 Decrepitation of Ni-Cu-Ni-coated Sm_2Co_{17} magnets

As previously explained that sintered Sm_2Co_{17} magnets require a high condition of 20 bar for 2 days for the decrepitation, the presence of the Ni-Cu-Ni layers on the magnets, surface is expected to further increase those conditions as the coating will hinder the direct adsorption of hydrogen on the surface of the Sm_2Co_{17}. 40 bar for 2 days at room temperature were required for the decrepitation of the 1 kg of the coated magnets. Even by applying the latter conditions, only 50 wt.% of the decrepitated powder has a size lower than 400 µm. Most of the coating (around 98 wt.%) was easily separated by sieving via 250 µm sieve.

4.2.6 Chemical dissolution of Ni-Cu-Ni coating on Sm_2Co_{17} magnets

The kinetics of the elements' dissolution by the application of 2M HNO_3 are shown in Figure 4.39. Due to the relatively big volume of the Sm_2Co_{17} in comparison to the previously studied $SmCo_5$, at least 390 min were required for the complete Ni removal using the mentioned concentration and volume of the acid. As discussed previously, cracking or fracture in the coating layers is expected to occur in that long period, which results in the dissolution of the elements from the magnet itself, as shown a high amount of the magnets' elements were dissolved before the complete dissolution of the coating. The colours of the zirconium and iron nitrate are transparent and pale violet, respectively; the colours of the nitrate of the other elements are mentioned previously. Note that the

Sm_2Co_{17} magnets also contain Cu in its microstructure beside the coating layer, this was represented in the figure as Cu-coating and Cu-magnet.

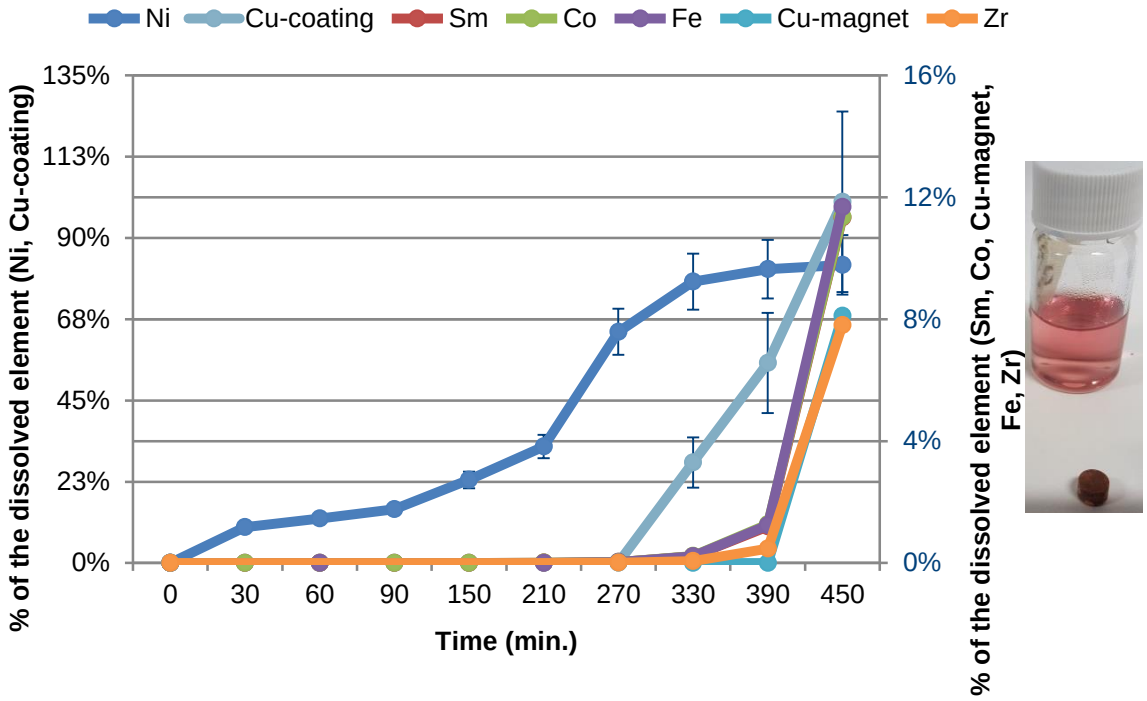

Figure 4.39: The dissolution of Ni, Sm, Co, Cu, Fe and Zr from coated Sm_2Co_{17} magnets by 2M HNO_3.

Similar to the results from $SmCo_5$ magnets, after a reaction for 20 min of the magnets with 1 vol.% Br with DMF, EG, ethanol, MeOAc and EtOAc, there was a relation between the polarity of the used organic and the speed of the reaction, except EG (Figure 4.40). Most of the Ni and Cu from the magnet were removed by using ethanol and DMF. The colours of zirconium and iron bromide are white and brown, respectively.

The kinetics of the elements' dissolution by using the Br solution with ethanol, DMF and EG are shown in Figure 4.41, Figure 4.42 and Figure 4.43, respectively. Similarly to $SmCo_5$, 5-10 min were enough for the DMF to remove all the coating, in case of ethanol, 20-25 min were needed. The amount of the dissolution of all other elements from the magnet was less than 1 vol.% after the previous reaction periods. For EG, even after 4h of reaction, there was no complete dissolution of the coating material.

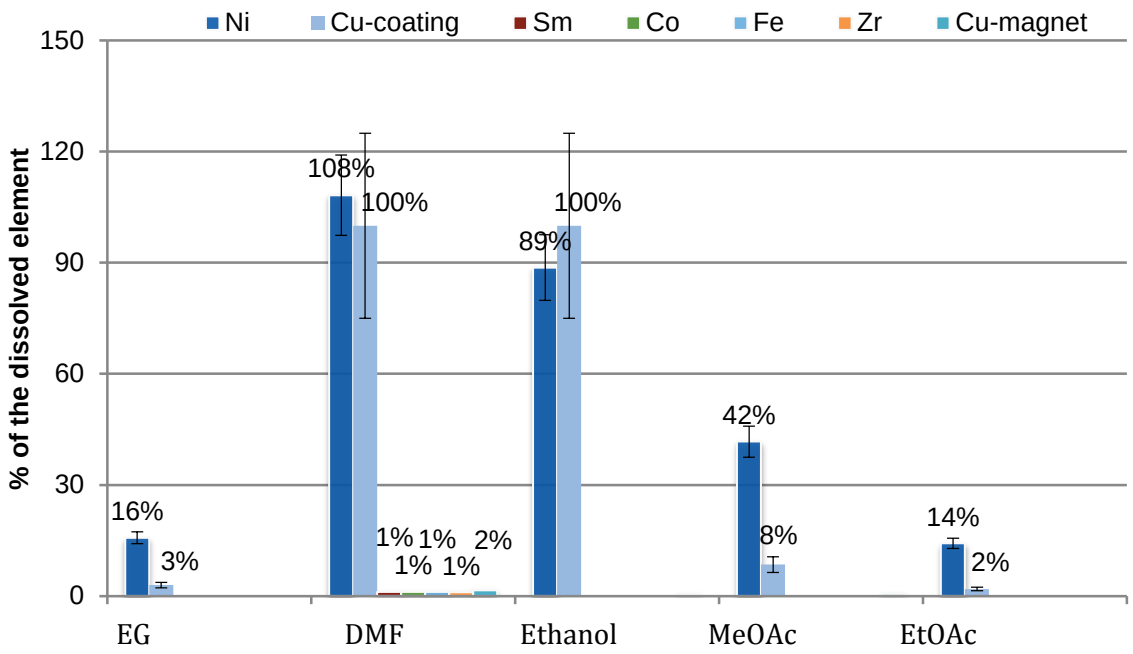

Figure 4.40: The dissolution of Ni, Sm, Co, Cu, Fe and Zr from coated Sm_2Co_{17} magnets by 1 vol.% Br_2/organic in a reaction time of 20 min.

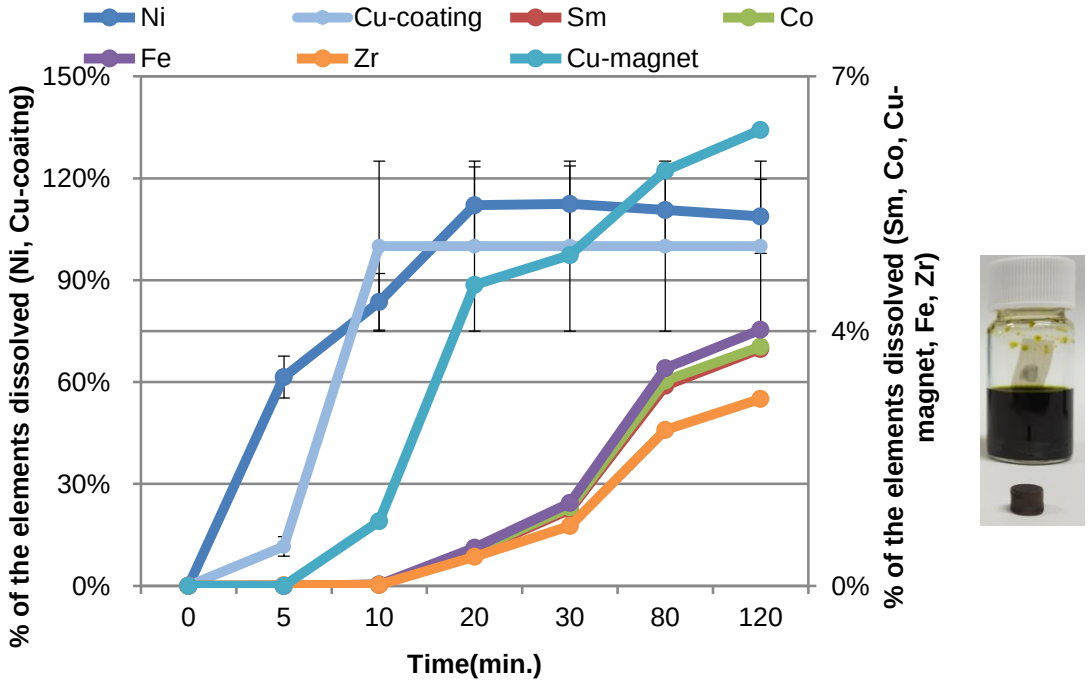

Figure 4.41: The dissolution kinetics of Ni, Sm, Co, Cu, Fe and Zr from coated Sm_2Co_{17} magnets by 1 vol.% Br_2/ethanol.

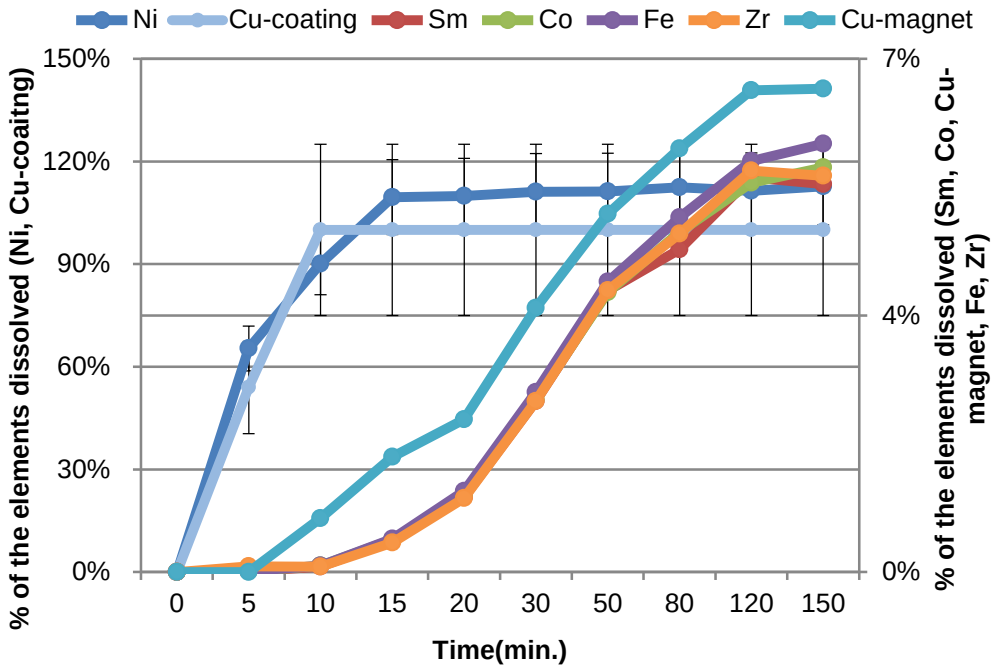

Figure 4.43: The dissolution kinetics of Ni, Sm, Co, Cu, Fe and Zr from coated Sm_2Co_{17} magnets by 1% Br_2/DMF.

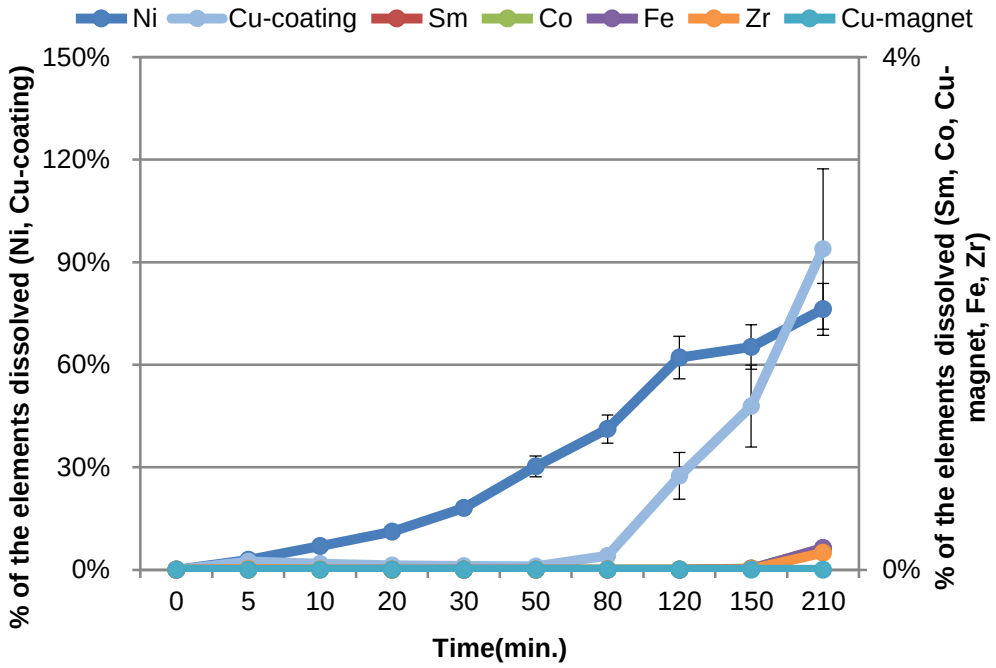

Figure 4.42: The dissolution kinetics of Ni, Sm, Co, Cu, Fe and Zr from coated Sm_2Co_{17} magnets by 1% Br_2/EG.

4.2.7 Properties of Sm_2Co_{17} with different Ni/Cu content

Five magnets were prepared with the addition of Ni/Cu (80 wt.%/20 wt.%), with 0 wt.%, 0.2 wt.%, 0.5 wt.%, 1 and 2 wt.%. The measured densities for all the sintered samples with a different Ni/Cu concentration were higher than 8.3 g/cm^3 which is about 98.5% of the theoretical density for the industrially produced Sm_2Co_{17} samples. The measured oxygen content for all the samples was lower than 0.3 wt.%. Figure 4.44 and Table 4.13 show the demagnetization curves and the change in the B_r, $_bH_c$, $_iH_c$ and $(BH)_{max}$ for the samples with increasing the Ni/Cu concentration. Apart from the B_r values which showed to slightly decrease with the increase in the Ni/Cu concentration, the magnetic properties of the samples showed a tendency of high deterioration with the increase in the concentration of the Ni/Cu addition. Up to Ni/Cu concentration of 1 wt.%, the sample may still be produced industrially as the sample showed $_iH_c$, $_bH_c$ and $(BH)_{max}$ of >1500 kA/m, 750 kA/m and 200 kJ/m^3, respectively. Further increase in the concentration of Ni/Cu to 2 wt.% resulted in the formation of a noticeable knee in the demagnetization curves of the sample with the reduction of the magnetic properties beyond the values which can be accepted for industrial production. The $_bH_c$ and $(BH)_{max}$ for the 2 wt.% Ni/Cu sample is 688.2 kA/m and 188.3 kJ/m^3, respectively.

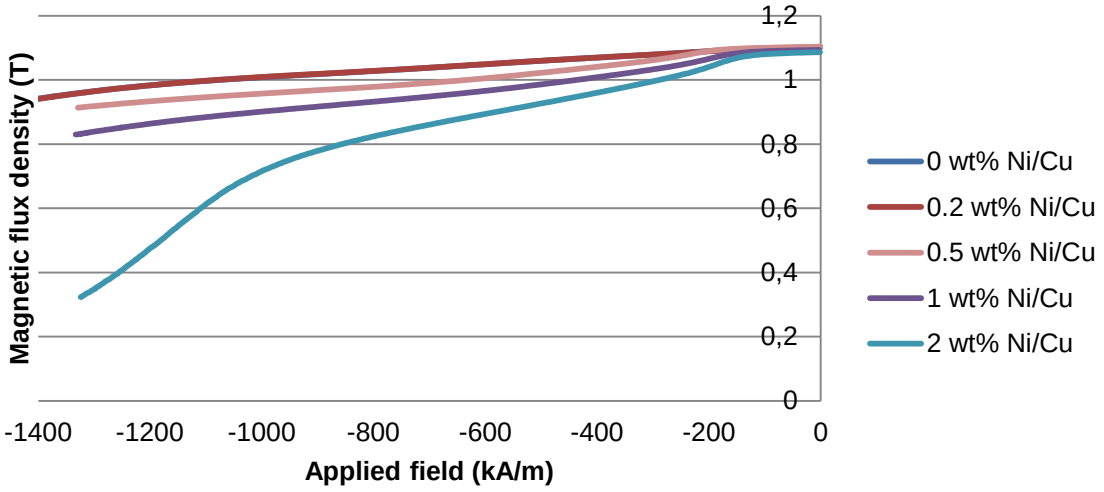

Figure 4.44: The demagnetization curves for the Sm_2Co_{17} magnets with 0-2 wt.% Ni/Cu content.

The coarse-grains and fine-cellular microstructures of the samples with Ni/Cu of 0 wt.%, 1wt.% and 2wt.% are shown in Figure 4.45. Table 4.14 shows the EDX analysis of the matrix phase. The samples showed to consist of a matrix phase with a similar composition to each other, with a Sm-oxide phase (light phase) and traces of a Zr-rich phase (as explained earlier its concentration was similar around 0.5% for all the samples). No trend in the change of the concentrations of the elements was observed with increasing the Ni/Cu content, except the increase in the Ni content in the matrix phase. The XRD studies of the samples with a different Ni/Cu addition are shown in Figure 4.46, as shown no new phases were observed by the XRD analysis.

It was observed that the size of the cells of the $Sm_2(Co,Fe)_{17}$ cellular structure increases with the Ni/Cu concentrations. The cellular structures have sizes of around 120 nm, 160 nm and 200 nm for the samples with 0 wt.%, 1 wt.% and 2 wt.%, respectively. As described earlier, the formation of a small cell interior with homogenous $Sm(Co,Cu)_5$ cell boundary is necessary for the pinning in Sm_2Co_{17} magnets and increasing the size of the cell would lead to a decrease in the coercivity of the magnets, as observed with the increase in the Ni/Cu content. To further confirm the relation between the increase in the

added Ni/Cu content and the cell interior, hence the coercivity, Sm_2Co_{17} magnet with 4 wt.% Ni/Cu was prepared. The fine-cellular microstructure of the 4 wt.% Ni/Cu samples is shown in Figure 4.47, where the cell average interior size was measured to be 230 nm, moreover, the boundary $Sm(Cu,Co)_5$ phase was formed as inhomogeneous for the sample. As expected, the magnetic properties of the magnets with 4 wt.% Ni/Cu were very low with ${}_iH_c$ of 303.3 kA/m and $(BH)_{max}$ of 146 kJ/m^3.

Table 4.13: The magnetic properties of sintered Sm_2Co_{17} magnets with Ni/Cu from 0 wt.% to 2 wt.%. for the magnets is higher than 1500 kA/m.

	B_r [T]	${}_bH_c$ [kA/m]	$(BH)_{max}$ [kJ/m^3]
100 wt.% Sm_2Co_{17}	1.10	816.48	226.9
99.8 wt.% Sm_2Co_{17} – 0.2 wt.% Ni/Cu	1.10	816.93	226.8
99.5 wt.% Sm_2Co_{17} – 0.5 wt.% Ni/Cu	1.10	780.35	215.6
99 wt.% Sm_2Co_{17} – 1 wt.% Ni/Cu	1.08	748.2	203.7
98 wt.% Sm_2Co_{17} – 2 wt.% Ni/Cu	1.08	688.2	188.3

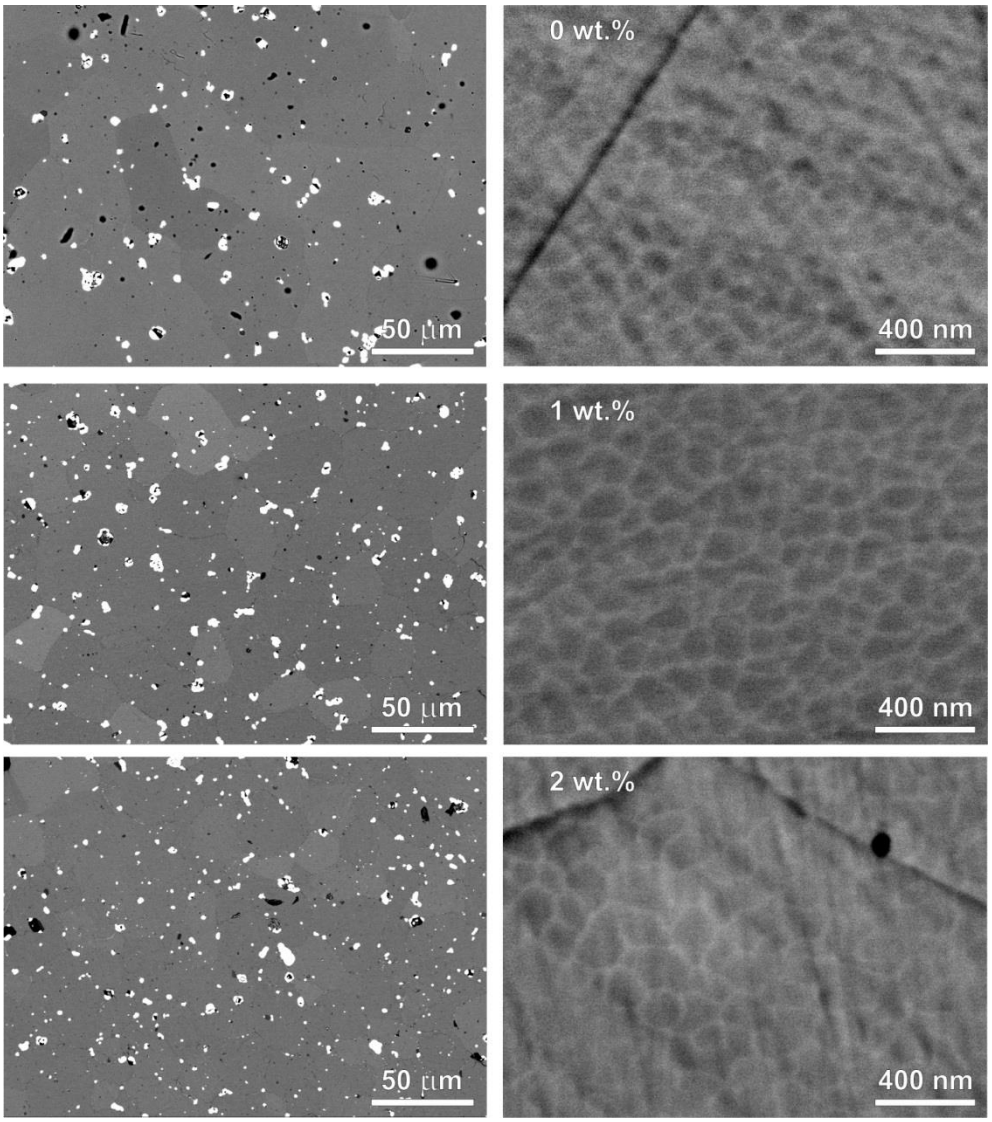

Figure 4.45: The coarse-grains (left) and the fine-cellular (right) microstructures for the Sm_2Co_{17} magnets. From top to bottom: 0 wt.% Ni/Cu, 1 wt.% Ni/Cu, 2 wt.% Ni/Cu.

Table 4.14: The matrix phase composition (in at.%) for the sintered Sm_2Co_{17} with Ni/Cu of 0 wt.%, 1wt.% and 2wt.%.

	Sm	Co	Fe	Cu	Zr	Ni
100 wt.% Sm_2Co_{17}	11.0	58.0	22.8	5.95	2.31	-
99 wt.% Sm_2Co_{17} – 1 wt.% Ni/Cu	10.8	57.4	22.1	5.95	2.36	1.11
98 wt.% Sm_2Co_{17} – 2 wt.% Ni/Cu	10.7	57.2	21.9	6.09	2.15	2.04

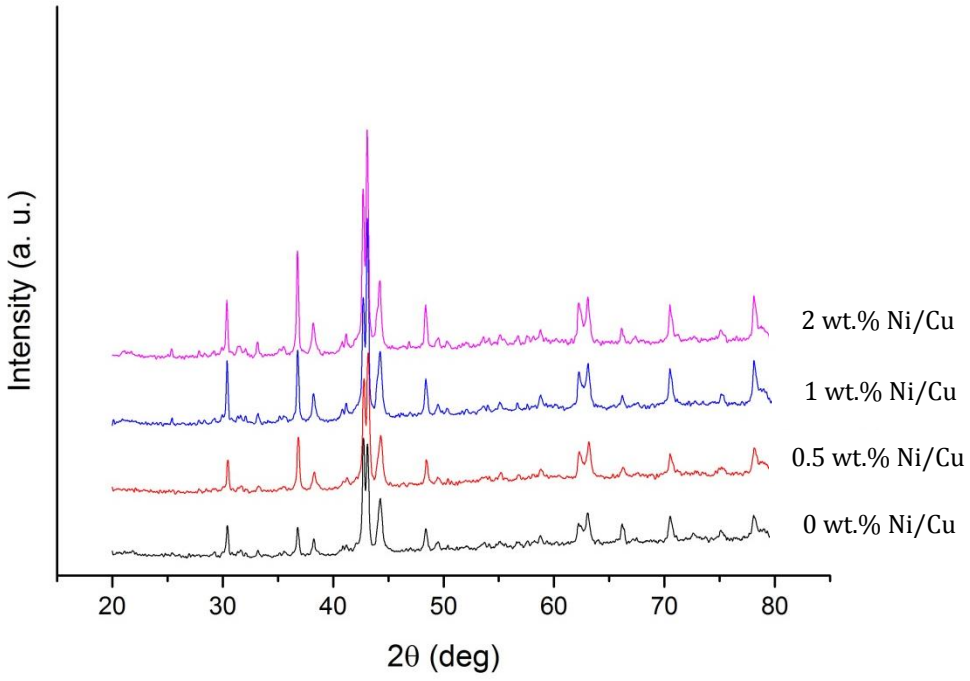

Figure 4.46: XRD patterns of the sintered Sm_2Co_{17} samples with 0 wt.% Ni/Cu, 0.5 wt.% Ni/Cu, 1 wt.% Ni/Cu, 2 wt.% Ni/Cu.

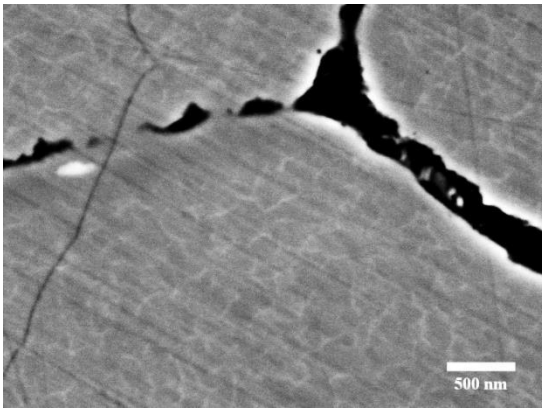

Figure 4.47: Fine-cellular microstructure of the Sm_2Co_{17} magnets with 4 wt.% Ni/Cu.

In order to locate the added Ni/Cu and as it was not visible by SEM and XRD analysis, TEM study for the sample with 2 wt.% was performed (Figure 4.48); the latter was chosen

as it was the start for the noticeable deterioration of the magnetic properties. The concentration of the Ni element was shown to be higher in the cell boundary phase, as shown by a line scan in the figure. The presence of the Ni in the cell boundary phase hindered the formation of the appropriate cellular microstructure at the applied conditions which would result in decreasing the intrinsic coercivity and the pinning strength of the cell boundary phase with a negative effect on the magnetic properties. The same behaviour was observed by Tang et al. [115] for the study conducted in the replacement of Cu by Ni in the Sm_2Co_{17} magnets.

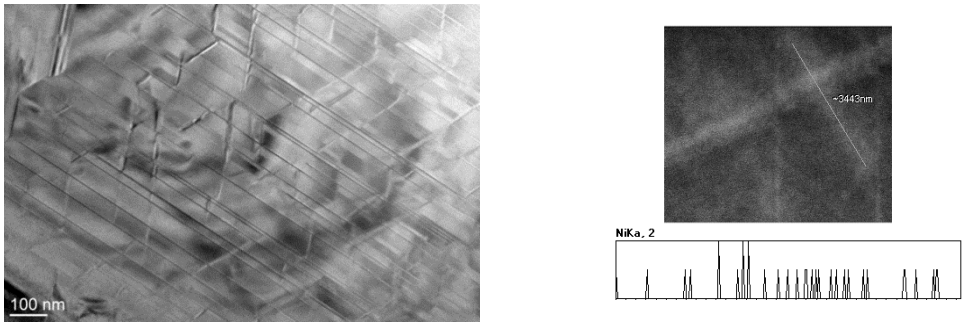

Figure 4.48: The cellular structure of the 2 wt.% Ni/Cu magnets (parallel to the c axis of the 2:17 phase), showing the lamellar $Zr(Co,Fe)_3$ phase (left). A line scan showing the increase of the Ni content in the cell boundary phases (right).

4.2.8 Other way to recycle Sm_2Co_{17} magnets: strip casting

The strip-cast Sm_2Co_{17} produced from using the sintered magnets as the starting material has an oxygen content lower than 0.02 wt.%. Figure 4.49 and Figure 4.50 show the microstructure and the XRD patterns of the strip-cast material, respectively. The microstructure of the strip-cast material was similar to the one for book moulding with very fine columnar grains of less than 5 μm. The composition of the matrix phase was measured by EDX to be 24.33 wt.%, Sm, 49.6 wt.% Co, 18.92 wt.% Fe, 4.85 wt.% Cu and 2.3 wt.% Zr, which is similar to the matrix phase in sintered magnets. Hence recovery of less than 50% was achieved out of the starting material; the strip-cast material was not proceeded to produce recycled magnets. However further experiments are planned to increase the recovery value and to continue the recycling scheme by the production of sintered magnets from the strip cast both by applying HD or a normal crushing route.

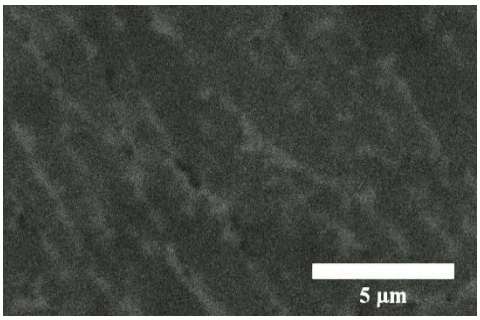

Figure 4.49: BSE images for a strip-cast product from sintered Sm_2Co_{17}. Refinement in the microstructure was observed after strip casting.

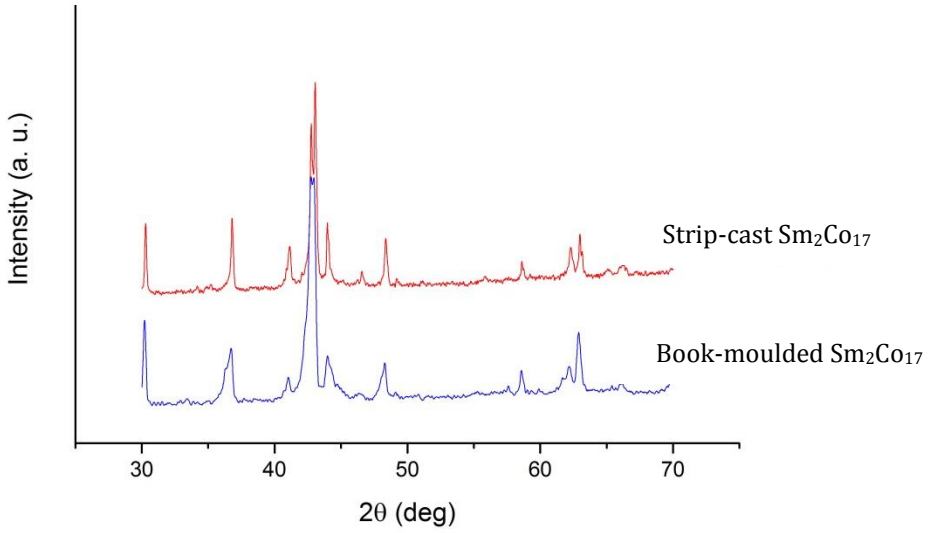

Figure 4.50: The XRD patterns showing the similarity of the peaks for the book-moulded (rich in Co as in Figure 4.30, left) and the strip-cast Sm_2Co_{17} material.

Chapter 5

Conclusions and Future Work

5.1 Conclusions

HD has been shown to be an effective technique for the recycling of both $SmCo_5$ and Sm_2Co_{17} magnets. A pressure of hydrogen as low as 1 bar can be applied for the decrepitation of $SmCo_5$ magnets, where the decrepitation reaction starts with the reaction of Sm-rich phases of a composition close to Sm_2Co_7. On the other hand, at least 20 bars are required for Sm_2Co_{17} magnets, because of the lower Sm content in the Sm_2Co_{17} magnets, where the highest Sm content phase in the magnet is $Sm(Co,Cu)_5$. $Sm(Co,Cu)_5$ is the phase which starts the hydrogen absorption and the decrepitation in Sm_2Co_{17} magnets. By using a conventional sintering technique, the decrepitated powders were used for the preparation of recycled magnets containing more than 98 wt.% recycled material for both $SmCo_5$ and Sm_2Co_{17} magnets with as good magnetic properties as the original magnets before recycling. For $SmCo_5$ the properties of the recycled magnets were; $B_r = 0.94$ T, ${}_iH_c$ >1500 kA/m, $(BH)_{max}$ of 171.1 kJ/m^3 and for Sm_2Co_{17}; $B_r = 1.09$ T, ${}_iH_c$ >1500 kA/m and $(BH)_{max} = 218.3$ kJ/m^3. The HD process was also applied to fresh as-cast $SmCo_5$ and Sm_2Co_{17} alloys, pressure of 1 bar of hydrogen was sufficient for the decrepitation of all the used alloys; except the Sm_2Co_{17} alloy with a low Sm content of 24 wt.%, a pressure of 4 bar was required.

SPS technique was used for the consolidation of the recycled powder to produce isotropic recycled magnets. The process was shown to be effective for the preparation of $SmCo_5$ magnets with very good magnetic properties of ${}_iH_c$ over 1500 kA/m. The microstructure of the SPS-ed $SmCo_5$ sintered at 900 ^oC magnets showed to contain $SmCo_5$ matrix phase with Sm_2Co_7, which is similar to the conventional sintered magnets. The SPS-ed samples also showed relatively good magnetic properties at 180 ^oC. On the other hand, SPS-ed Sm_2Co_{17} magnets showed to have poor magnetic properties, because of the complex structure required for the magnetic properties which can only be formed at slow conventional heat treatments. The microstructures of the SPS-ed Sm_2Co_{17} samples show to be inhomogeneous with the formation of several impurity phases.

Polymer-bonded magnets were also shown to be a good alternative procedure for processing Sm_2Co_{17} recycled powder. Relatively good magnetic properties were achieved; $B_r = 0.58$ T, ${}_iH_c$ >1500 kA/m and $(BH)_{max} = 56$ kJ/m^3. For $SmCo_5$ magnets, the properties of the magnets were poor because of the oxidation of the Sm-rich phase during the atmospheric heating step.

It was possible to remove all the coating material on the magnets, surface by reacting with 1% Br/DMF or ethanol solutions for less than 20 min or sieving the decrepitated powder; only 2 wt.% of the coating was left in the decrepitated powder. The presence of coating residuals on the magnetic properties of the magnets was studied, where it was shown that coating residuals up to 2 wt.% can be present in the $SmCo_5$ recycled powder and 1 wt.% for Sm_2Co_{17}, without much effect on the properties of the recycled magnets.

Strip-casting technique was also studied. It was shown that this technique was a possible effective recycling route for the magnets. Its downside was relatively low recovery because a large amount of material was discarded as waste.

5.2 Future Work

The possibility of the decrepitation of as-cast Sm-Co alloys at low pressures of atmospheric level opens the possibility to use HD as a crushing method industrially. Fresh sintered Sm-Co magnets by using HD process for crushing instead of the hammering process will be prepared after milling the decrepitated powders and to compare the properties of the magnets with the industrially produced ones.

Strip casting was also shown to be an effective technique for removing the oxygen from the magnets to be recycled, but as we mentioned this results in wasting a large amount of the material. The parameters of the casting will be studied to decrease the amount of the waste material to lower than 20 wt.% and the strip-cast recycled material will be used for the preparation of sintered magnets after crushing or HD and milling.

Appendix A

Safety and Health Issues

This section is devoted to anyone who would like to know more about the background of the risk associated with the given work or the precautions required to apply it.

A.1 Hydrogen Decrepitation

The process of hydrogen decrepitation involves applying hydrogen gas, where high pressures may be needed to break the solid samples. The type of the vessel in which the decrepitation is being performed should be non-reactive at all to the hydrogen gas. Introducing other gases to the vessel with hydrogen gas should be done only after careful investigation about the possible interactions.

Mostly, after decrepitation, the materials keep some of the hydrogen absorbed in its microstructure. Hydrogen may be released by time or at certain temperatures and the previous note should always be remembered when storing or further processing the material.

A.2 Magnetic Field

There is no data about the hazardous effects due to the exposure to magnetic fields, even strong ones. However, in case of the presence of any metallic materials in or/and on the body; as pacemakers, bracelets and watches, the exposure should be avoided due to the possible interaction between the field and the metallic components. Moreover, the magnetic field generated by the magnets can be very strong; therefore handling the magnets should be carried out with great care to avoid injuries.

A.3 Bromine

Bromine is a fuming liquid which evaporates at room temperature. Always wear the appropriate safety equipment when handling and open the bottle containing the element only inside a fume hood. It is recommended to put the bottle in an ice bath before the usage in order to decrease the evaporation of the element.

A.4 Unexpected Problems During the Reproduction of the Work

Problem: Sensitivity of Sm-Co for sintering and heat treatment temperature, especially for $SmCo_5$ which might result in bad magnetic properties for the produced magnet.
Solution: Check the temperature and the partial pressure stability, the leaking of the furnace, the oxygen content, and the quality of the inert gas.

A.5 The Safety Symbols for all Used Materials

Table A.1 shows the safety symbols for all the used materials in this study. Before starting work with any of the material, checking the safety symbols and material safety data sheet is recommended.

Table A.1: Safety symbols for materials used in this study.

Material	Form used	GHS label	NFPA 704 label
SmCo	Powder		
Sm	Powder		
Cu	Powder		
H_2	Gas		
Ar	Gas		
Co	Powder		
Ni	Powder		
Fe	Powder		
HCl	Liquid		

Table 1: Safety symbols for materials used in this study.

Material	Form used	GHS label	NFPA 704 label
HNO_3	Liquid		
MeOAC	Liquid		
EtOAC	Liquid		
Ethanol	Liquid		
DMF	Liquid		
EG	Liquid		
Br_2	Liquid		

Appendix B

The Function of Permanent Magnets in Some Industrial Devices

Permanent magnets (PMs) are those which create their own persistent magnetic field when magnetized by an external magnetic field. The function of permanent magnets in different appliances and instruments is usually one of the following:

- to convert mechanical energy to electrical energy,
- to convert electrical energy to mechanical energy,
- to use the attraction or repulsion between two magnets,
- to control electrons or ions.

Here we will describe the operational functions of permanent magnets in some devices:

B.1 Electric Motors

Electric motors are electrical machines which use electrical energy to produce mechanical energy. Let us take an example of a simple PM brushed direct current motor shown below which contains two essential parts, a fixed stator which is usually a permanent magnet and inside the stator there is a rotor which is usually an electromagnetic coil. When applying electricity in the coil, it produces a magnetic field which reacts with the magnetic field produced from the permanent magnet stator causing the production of mechanical energy in the form of rotating the electromagnetic coil. This mechanical energy is used to move cars, rotate fans, fly drones and so on. Figure B. 1 shows a simplified diagram of electric motors.

B.2 Loudspeakers

Loudspeaker is another device that converts electrical energy to mechanical energy. The permanent magnet in the loudspeaker is fixed close to a mobile electromagnet coil. The electromagnet is attached to a flexible material called a cone (diaphragm). Passing an electric current in the electromagnet causes it to vibrate due to the interaction with the permanent magnet. The cone amplifies these vibrations to produce sound waves. The pitch of the sound is controlled by the frequency of the vibration while the amplitude controls the volume produced. Microphones use the same set as loudspeakers in reverse mechanism to convert sound waves to electrical signal. Figure B.2 shows a simplified diagram of electric motors.

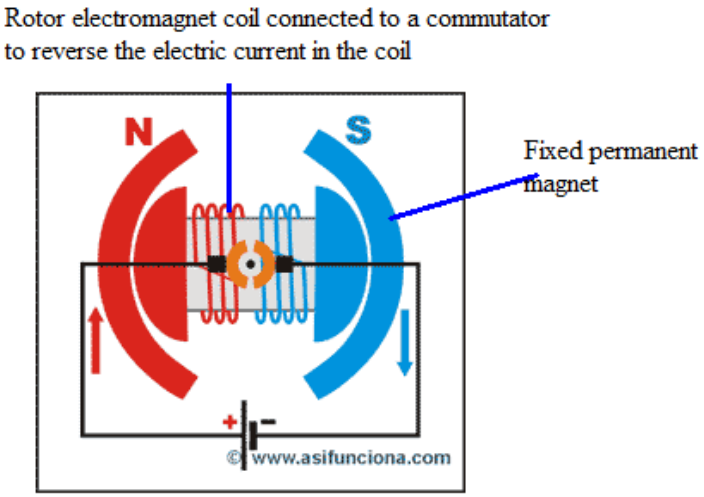

Figure B.1 : A simplified diagram of an electric motor [1].

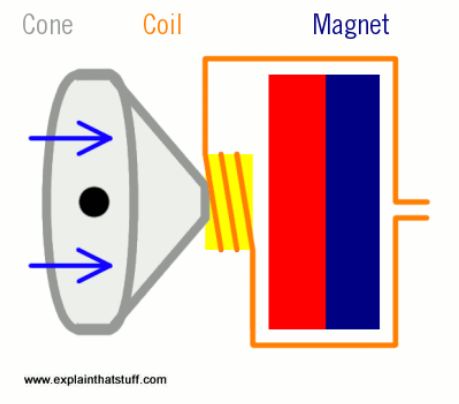

Figure B.2: A simplified diagram of loudspeaker components [2].

B.3 Hard Disk Drives

Hard disk drives (HDDs) use a magnetic storage mechanism in order to write and store information on a magnetic coated disk called platter (the mechanism of reading and writing is fascinating, go and read about it [3]). Usually there are three permanent magnets in a HDD. A fixed permanent magnet in the actuator which moves the read-write arm by the interaction with an electromagnet (electrical to mechanical energy), a small magnet at the end of the read-write arm which is responsible for the reading-writing actions with the platter, and a third permanent magnet in the spindle motor to allow the platter to rotate at high speed. Figure B.3 shows the component of a hard disk drive.

B.4 Electric Generators

In contrast to electric motors, electric generators convert mechanical energy to electricity. The mechanical energy is driven from winds as in wind turbines, from water as in water

turbines, from steam as in steam turbines from human muscle power, etc. An example of an electric generator is shown below. The permanent magnet here is fixed surrounding a coil which is connected to the mechanical energy source causing the latter to rotate. An induced current passes through the coil resulting from the rotation of the coil in the magnetic field from the permanent magnet. Figure B.4 shows a simplified diagram of electric generators.

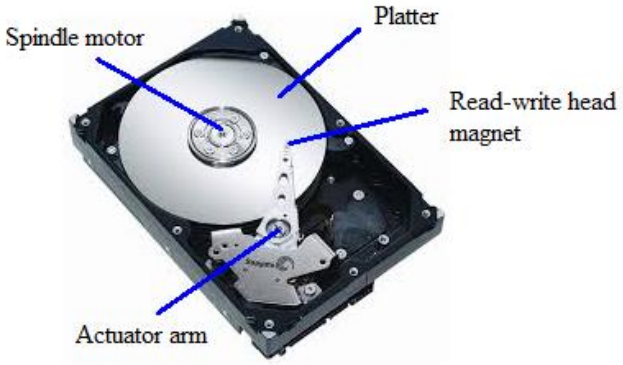

Figure B.3: Hard disk drive [3].

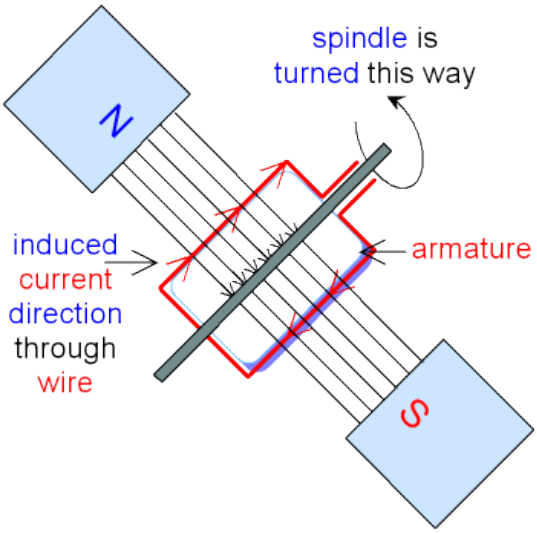

Figure B.4: A simplified diagram of an electric generator [4].

B.5 Maglev

Maglev is a transportation system that uses magnetic levitation to move vehicles [5]. Electrodynamic suspension (EDS) is one type of the Maglev technologies. In EDS both the train and the track exert a magnetic field and the train is levitated by repulsion and attraction forces between them. The magnetic field of the train is produced by PMs or

superconductors where an induced magnetic field is created in the track to move the train by the attraction and repulsion forces. Figure B.5 shows the idea of working of EDS.

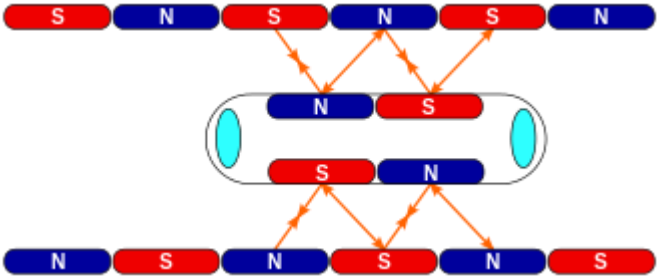

Figure B.5: EDS Maglev [6].

The function of permanent magnets in different appliances and instruments can be easily manipulated depending on the application in use. This permits them to be used in an unlimited number of products as in mobiles, televisions, laundry machines, microwaves, cars, synchrotrons, wind turbines and so on. And any simple idea can permit the use of PMs in a new set of applications. Go and check some videos for mind blowing uses of magnets and magnetism.
Some interesting videos:

- https://www.youtube.com/watch?v=ZZEFTEEHOPU
- https://www.youtube.com/watch?v=Pcw6vH0Eiug
- https://www.youtube.com/watch?v=5BeFoz3Ypo4
- https://www.youtube.com/watch?v=1RbsCiorwzI
- https://www.youtube.com/watch?v=IANBoybVApQ
- https://www.youtube.com/watch?v=jiAhiu6UqXQ
- https://www.youtube.com/watch?v=iZ4pQ9-IJ1w
- https://www.youtube.com/watch?v=58Gxe2ewHGo

B.6 References and Further Readings:

[1] J. Antonio, and G. Álvarez, “Así funciona el motor de corriente directa o continua” 2015. [online]. Avaliable: http://www.asifunciona.com/electrotecnia/af_motor_cd/af_motor_cd_7.htm. [Accessed: Jan. 1, 2019].
[2] C. Woodford, “Loudspeakers” 2018. [online]. Avaliable: https://www.explainthatstuff.com/loudspeakers.html. [Accessed: Jan. 1, 2019].
[3] “Magnetic storage” 2019. [online]. Avaliable: https://en.wikipedia.org/wiki/Magnetic_storage. [Accessed: Jan. 1, 2019].
[4] “Electromagnetism” 2015. [online]. Avaliable: http://www.gcsescience.com/pme18.htm. [Accessed: Jan. 1, 2019].
[5] “Magnetic levitation” 2019. [online]. Avaliable: https://en.wikipedia.org/wiki/Magnetic_levitation. [Accessed: Jan. 1, 2019].
[6] “Maglev” 2019. [online]. Available: https://en.wikipedia.org/wiki/Maglev. [Accessed: Jan. 1, 2019].

References

[1] A. Eldosouky and I. Škulj, "Recycling of $SmCo_5$ magnets by HD process," *Journal of Magnetism and Magnetic Materials*, vol. 454, pp. 249-253, 2018.

[2] A. Eldosouky, A. Ikram, M. F. Mehmood, X. Xu, S. Šturm, K. Ž. Rožman and I. Škulj, "Hydrogen decrepitation and spark plasma sintering to produce recycled $SmCo_5$ magnets with high coercivity," *IEEE Magnetics Letters*, vol. 9, pp. 1-4, 2018.

[3] A. Eldosouky and I. Škulj, "Hydrogen Reaction with SmCo Compounds: Literature Review," *Journal of Sustainable Metallurgy*, vol. 4, pp. 516–527, 2018.

[4] K. H. J. Buschow and E. P. Wohlfarth, *Handbook of Ferromagnetic Materials*. North Holland, 1988.

[5] J. Needham, *Science and civilisation in China*. Cambridge University Press, 1962.

[6] C. N. Bromehead, "Alexander Neckam on the Compass-Needle," J*ournal of geophysical research*, vol. 50, pp. 139-140, 1945.

[7] G. Turner, *North Pole, South Pole: The epic quest to solve the great mystery of Earth's Magnetism*. The Experiment, 2011.

[8] G. L. Verschuur, *Hidden attraction: The Mystery and History of Magnetism*. Oxford University Press, 1996.

[9] C. L. Smithells, Eds., *Metals Reference Book*. Butterworth-Heinemann, 1976.

[10] E. W. Lee, *Magnetism: an introductory survey*. Courier Corporation, 1970.

[11] M. McCaig, *Permanent magnets in theory and practice*. Wiley, 1987.

[12] J. J. Went, G. W. Rathenau, E. W. Gorter and G. W. van Oosterhout, "Ferroxdure. a class of new permanent magnet materials," *Phil. Tech. Rev.*, vol. 13, no. 7, pp. 194-208, 1952.

[13] K. J. Strnat, G. Hoffer, J. Olson, W. Ostertag and J. J. Becker, "A family of new cobalt base permanent magnet materials," *J. Appl. Phys*, vol. 38, no. 3, pp. 1001–1002, 1967.

[14] D. K. Das, "Twenty Million Energy Product Samarium-Cobalt Magnet," *IEEE Trans. Magn.*, vol. 5, no. 3, pp. 214–216, 1969.

[15] M. G. Benz and D. L. Martin, "Mechanism of Sintering in Cobalt Rare-Earth Permanent-Magnet Alloys," *J. Appl. Phys.*, vol. 43, no. 7, pp. 3165–3170, 1972.

[16] H. Nagel, A. J. Perry and A. Menth, "Hard-magnetic properties and microstructure of Sm(Co,Cu)z compounds," *J. Appl. Phys.*, vol. 47, no. 6, pp. 2662–2670, 1976.

[17] K. J. Strnat and R. M. W. Strant, "Rare earth-cobalt permanent magnets," *J. Magn. Magn. Mater.,* vol. 100, pp. 38–56, 1991.

[18] J. J. Croat, J. F. Herbst, R. W. Lee and F. E. Pinkerton, "Pr-Fe and Nd-Fe-based materials: A new class of high-performance permanent magnets," *J. Appl. Phys.*, vol. 55, no. 6, pp. 2078–2082, 1984.

[19] M. Sagawa, S. Fujimura, N. Togawa, H. Yamamoto and Y. Matsuura, "New material for permanent magnets on a base of Nd and Fe," *J. Appl. Phys.*, vol. 55, no. 6, pp. 2083–2087, 1984.

[20] Y. Matsuura, "Recent development of Nd-Fe-B sintered magnets and their applications," *J. Magn. Magn. Mater.*, vol. 303, no. 2, pp. 344–347, 2006.

[21] H. Izumi, K. Machida, A. Shiomi, M. Iguchi, K. Noguchi and G. Adachi, "Preparation of $Sm_2Fe_{17}N_x$ powders and their bonded magnets with high-performance permanent magnetic characteristics," *Chem. Mater.*, vol. 9, no. 12, pp. 2759–2767, 1997.

[22] O. Gutfleisch, M. A. Willard, E. Brück, C. H. Chen, S. G. Sankar and J. P. Liu, "Magnetic materials and devices for the 21st century: stronger, lighter, and more energy efficient," *Adv. Mater.*, vol. 23, no. 7, pp. 821–842, 2011.

[23] M. Getzlaff, *Fundamentals of magnetism*. Springer, 2007.

[24] W. D. Callister, *Materials science and engineering*. John Wiley & Sons, Inc., 2007.

[25] S. Pan, *Rare Earth permanent-magnet alloys' high temperature phase transformation: In situ and dynamic observation and its application in material design*. Springer, 2014.

[26] J. M. D. Coey and H. Sun, "Improved magnetic properties by treatment of iron-based rare earth intermetallic compounds in anmonia," *J. Magn. Magn. Mater.*, vol. 87, no. 3, pp. L251–L254, 1990.

[27] K. Kumar, D. Das and E. Wettstein, "High coercivity, isotropic plasma sprayed samarium-cobalt magnets," *J. Appl. Phys.*, vol. 49, no. 3, pp. 2052-2054, 1978.

[28] J. M. D. Coey, *Magnetism and Magnetic Materials*. Cambridge University Press, 2010.

[29] S. Liu, J. Yang, G. Doyle, G. E. Knhl, C. Chen, M. Walmer, M. Walmer and G. Simon, "New Sintered High Temperature Sm-Co Based Permanent Magnet Materials," *IEEE Trans. Magn.*, vol. 35, no. 5, pp. 3325–3327, 1999.

[30] J. Bernardi, J. Fidler, M. Sagawa and Y. Hirose, "Microstructural analysis of strip cast Nd-Fe-B alloys for high $(BH)_{max}$ magnets," *J. Appl. Phys.*, vol. 83, no. 11, pp. 6396–6398, 1998.

[31] Vacuumschmelze.com, "Permanent magnets & systems," 2012. [online]. Avaliable: https://www.vacuumschmelze.com/en/research-innovation/process-technology/permanent-magnets-systems.html. [Accessed: Jan. 1, 2019].

[32] S. Diouf and A. Molinari, "Densification mechanisms in spark plasma sintering: Effect of particle size and pressure," *Powder Technol.*, vol. 221, pp. 220–227, 2012.

[33] Z. Zhaohui, W. Fuchi, W. Lin, L. Shukui and S. Osamu, "Sintering mechanism of large-scale ultra fi ne-grained copper prepared by SPS method," *Materials Letters*, vol. 62, no. 24, pp. 3987–3990, 2008.

[34] W. Q. Liu, Z. Z. Cui, X. F. Yi, M. Yue, Y. B. Jiang, D. T. Zhang, J. X. Zhang and X. B. Liu, "Structure and magnetic properties of magnetically isotropic and anisotropic Nd–Fe–B permanent magnets prepared by spark plasma sintering technology," *J. Appl. Phys.,* vol. 107, pp. 09A719-3, 2010.

[35] W. Mo, L. Zhang, A. Shan, L. Cao, J. Wu and M. Komuro, "Microstructure and magnetic properties of NdFeB magnet prepared by spark plasma sintering," *Intermetallics,* vol. 15, no. 11, pp. 1483–1488, 2007.

[36] D. T. Zhang, W. C. Lv, M. Yue, J. J. Yang, W. Q. Liu, J. X. Zhang and Y. Qiang, "Nanocrystalline $SmCo_5$ magnet synthesized by spark plasma sintering," *J. Appl. Phys.,* vol. 107, pp. 09A701-4, 2010.

[37] M. Yue, J. H. Zuo, W. Q. Liu, W. C. Lv, D. T. Zhang, J. X. Zhang, Z. H. Guo and W. Li, "Magnetic anisotropy in bulk nanocrystalline $SmCo_5$ permanent magnet prepared by hot deformation," *J. Appl. Phys.,* vol. 109, pp. 07A711-3, 2011.

[38] L. Fang, T. Zhang, H. Wang, C. Jiang and J. Liu, "Effect of ball milling process on coercivity of nanocrystalline $SmCo_5$magnets," *J. Magn. Magn. Mater.*, vol. 446, pp. 200–205, 2017.

[39] P. Saravanan, R. Gopalan, D. Sivaprahasam and V. Chandrasekaran, "Effect of sintering temperature on the structure and magnetic properties of $SmCo_5$/Fe nanocomposite magnets prepared by spark plasma sintering," *Intermetallics*, vol. 42, pp. 199–204, 2013.

[40] T. Saito and D. Nishio-Hamane, "High-coercivity $SmCo_5$/α-Fe nanocomposite magnets," *J. Alloys Compd.*, vol. 735, pp. 218–223, 2018.

[41] Q. M. Lu, C. Zhou and M. Yue, "Enhanced Magnetic Properties and Thermal Stability of $Nd_2Fe_{14}B$/$SmCo_5$ Composite Permanent Magnets Prepared by Spark Plasma Sintering," *IEEE Trans. Magn.*, vol. 51, no. 11, pp. 3–6, 2015.

[42] D. Kopeliovich, "Spark plasma sintering," 2012. [Online]. Available: http://www.substech.com/dokuwiki/doku.php?id=spark_plasma_sintering. [Accessed: Jan. 1, 2019].

[43] J. Ormerod and S. Constantinides, "Bonded permanent magnets: Current status and future opportunities," *J. Appl. Phys.*, vol. 81, no. 8, pp. 4816–4820, 1997.

[44] S. Sugimoto, "Current status and recent topics of rare-earth permanent magnets," *J. Phys. D. Appl. Phys.*, vol. 44, no. 6, pp. 064001-11, 2011.

[45] Magmamagnets.com, "Neodymium magnets coating" [Online]. Available: http://www.magmamagnets.com/permanent-magnets/neodymium-rare-earth-magnets/neodymium-magnets-coating/. [Accessed: Jan. 1, 2019].

[46] A. Walton, Han Yi, N. A. Rowson, J. D. Speight, V. S. J. Mann, R. S. Sheridan, A. Bradshaw, I. R. Harris and A. J. Williams "The use of hydrogen to separate and recycle neodymium-iron-boron-type magnets from electronic waste," *J. Clean. Prod.*, vol. 104, pp. 236–241, 2015.

[47] V. Fernandez, "Rare-earth elements market : A historical and financial perspective Rare-earth elements market," *Resour. Policy*, vol. 53, pp. 26–45, 2017.

[48] Eurare.eu, Available: http://www.eurare.eu. [Accessed: Jan. 1, 2019].

[49] Palisadeglobal.com, Available: https://www.palisadeglobal.com/. [Accessed: Jan. 1, 2019].

[50] P. Searle, "Forecasting the cobalt market through 2015," *J. Miner. Met. Mater. Soc.*, vol. 50, no. 10, pp. 42–43, 1998.

[51] K. Binnemans and P. T. Jones, "Rare Earths and the balance problem," *J. Sustain.*

Metall., vol. 1, no. 1, pp. 29–38, 2015.

[52] "Permanent Magnet Market Size, Share & Trend Analysis Report By Product (Ferrite Magnet, Rare Earth), By Application (Automotive, Electronics, Industrial) By Region, And Segment Forecasts, 2013-2024," 2018. [Online]. Available: https://www.grandviewresearch.com/industry-analysis/permanent-magnets-industry. [Accessed: Jan. 1, 2019].

[53] European Commission, "Critical raw materials for the EU, Report of the Ad-hoc Working Group on defining critical raw materials," 2010. [online]. Available: https://ec.europa.eu/growth/tools-databases/eip-raw-materials/en/system/files/ged/79%20report-b_en.pdf. [Accessed: Jan. 1, 2019].

[54] European Commission, "Report on critical raw materials for the EU, Report of the Ad hoc Working Group on defining critical raw materials," 2010. [online]. Available: https://ec.europa.eu/docsroom/documents/10010/attachments/1/translations/en/renditions/pdf. [Accessed: Jan. 16, 2019].

[55] European Commission, "Study on the review of the list of critical raw materials," 2017. Available: https://publications.europa.eu/en/publication-detail/-/publication/08fdab5f-9766-11e7-b92d-01aa75ed71a1/language-enhttps://publications.europa.eu/en/publication-detail/-/publication/08fdab5f-9766-11e7-b92d-01aa75ed71a1/language-en. [Accessed: Jan. 16, 2019].

[56] Remanence FP7, Available: http://www.project-remanence.eu/. [Accessed: Jan. 16, 2019].

[57] MAG-DRIVE, Available: http://mag-drive-fp7.eu/. [Accessed: Jan. 16, 2019].

[58] DEMETER, Available: https://etn-demeter.eu/. [Accessed: Jan. 16, 2019].

[59] T. Xu, X. Zhang, Z. Lin, B. Lü, C. Ma and X. Gao, "Recovery of rare earth and cobalt from Co-based magnetic scraps," *J. Rare Earths*, vol. 28, pp. 485–488, 2010.

[60] Z. Wang Jingjing, Xu Tao, Ma Ying and W. D. Gong, "Recycling method of samarium cobalt magnetic waste material," CN Patent 103555950A, 12 Oct., 2013.

[61] H. Okamoto, "Co-Sm (Cobalt-Samarium)," *J. Phase Equilibria Diffus.*, vol. 32, no. 2, pp. 165–166, 2011.

[62] M. F. de Campos and F. J. G. Landgraf, "The occurrence of the phase $SmCoC_2$ in $SmCo_5$ magnets," In *Proc. 14th Int. Workshop on RE Magnets and their Applications, World Scientifc*, Sao Paulo, Brazil, pp. 432–440, 1996.

[63] M. F. de Campos and F. J. G. Landgraf, "On the microstructure of $SmCo_5$ magnets," *In Proc. 14th Int. Workshop on RE Magnets and their Applications, World Scientifc,* Sao Paulo, Brazil, pp. 321–338, 1996.

[64] W. Szmaja, K. Polański, I. Piwoński, A. Ilik and J. Balcerski, "Study of the morphological and magnetic microstructure of $SmCo_5$ magnets," *Vacuum*, vol. 81, no. 10, pp. 1363–1366, 2007.

[65] W. Szmaja, J. Grobelny and M. Cichomski, "Domain structure of sintered $SmCo_5$ magnets studied by magnetic force microscopy," *Appl. Phys. Lett.*, vol. 85, no. 14, p. 2878-2880, 2004.

[66] Dilip K. Das, "Influence of Sintering Temperature on Magnetic Properties of Samarium-Cobalt Magnets," *IEEE T Magn.* vol. 7, pp. 432–435, 1971.

[67] N. M. Talijan, A. Milutinović-Nikolić, R. Jančić, I. Petrović-Prelević and J. Stajić-Trosić, "The influence of the sintering regime on the stability of the SmCo phase," *Materials Letters*, vol. 32, pp. 85–89, 1997.

[68] M. F. de Campos, F. J. G. Landgraf, R. Machado, D. Rodrigues, S. A. Romero. A. C. Neiva and F. P. Missell, "A model relating remanence and microstructure of $SmCo_5$ magnets," *J. Alloys Compd.*, vol. 267, no. 1-2, pp. 257–264, 1998.

[69] D. L. Martin and M. G. Benz, "Review of cobalt-rare earth permanent magnet alloys," *AIP Conf. Proc. 5*, vol. 5, pp. 970-990, 1972.

[70] G. Gessinger, E. De Lamotte and K. Bachmann, "On the sintering mechanism of $SmCo_5$ powders," *IEEE Trans. Magn.*, vol. 8, pp. 557-559, 1972.

[71] K. Kumar, "$RETM_5$ and RE_2TM_{17} permanent magnets development," *J. Appl. Phys.*, vol. 63, no. 6, pp. R13-R57, 1988.

[72] M. F. de Campos, H. Okumura, G. C. Hadjipanayis, D. Rodrigues, F. J. G. Landgraf, A. C. Neiva, S. A. Romero and F. P. Misselle, "Effect of several heat treatments on the microstructure and coercivity of $SmCo_5$ magnets," *J. Alloys Compd.*, vol. 368, no. 1–2, pp. 304–307, 2004.

[73] S. Liu, K. J. Strnat and H. F. Mildrum, "Sintered $SmCo_5$ magnets-relations between coercivity and the anisotropy of major and minor phases," I*n Proc. 3rd International Symposium on Magnetic Anisotropy and Coercivity in RE Transition Metal Alloys, Baden,* Austria, pp. 631–642, 1982.

[74] L. K. Rabenberg, "Phase transformations and the development of magnetic coercivity in samarium-cobalt based permanent magnet alloys," Ph.D. thesis, University of California, 1983.

[75] F. J. A. den Broeder and H. Zijlstra, "Relation between coercive force and microstructure of sintered $SmCo_5$ permanent magnets," *J. Appl. Phys.*, vol. 47, no. 6, pp. 2688–2695, 1976.

[76] F. Okabe, H. S. Park, D. Shindo, Y. Park, K. Ohashi and Y. Tawara, "Microstructures and magnetic domain structures of sintered $Sm(Co_{0.720}Fe_{0.200}Cu_{0.055}Zr_{0.025})_{7.5}$ permanent magnet studied by transmission electron microscopy," *Mater.*, vol. 47, no. 1, pp. 218–223, 2006.

[77] Y. Zhang, W. Tang, G. C. Hadjipanayis, C. Chen, C. Nelson and K. Krishnan, "Evolution of microstructure, microchemistry and coercivity in 2:17 type Sm-Co magnets with heat treatment," *IEEE Trans. Magn.*, vol. 37, no. 4 I, pp. 2525–2527, 2001.

[78] R. Gopalan, K. Hono, A. Yan and O. Gutfleisch, "Direct evidence for Cu concentration variation and its correlation to coercivity in $Sm(Co_{0.74}Fe_{0.1}Cu_{0.12}Zr_{0.04})_{7.4}$ ribbons," *Scr. Mater.*, vol. 60, no. 9, pp. 764–767, 2009.

[79] J. F. Liu, Y. Ding and G. C. Hadjipanayis, "Effect of iron on the high temperature magnetic properties and microstructure of $Sm(Co,Fe,Cu,Zr)_z$ permanent magnets," *J. Appl. Phys.*, vol. 85, no. 3, pp. 1670–1674, 1999.

[80] R. S. Perkins and S. Strässler, "Interpretation of the magnetic properties of pseudobinary $Sm_2(Co,M)_{17}$ compounds. I. Magnetocrystalline anisotropy," *Phys. Rev. B*, vol. 15, no. 1, pp. 477–489, 1977.

[81] G. Wang and C. Jiang, "The coercivity and domain structure of $Sm(Co_{bal}Fe_{0.1}Cu_xZr_{0.033})_{6.9}$ ($x = 0.07$, 0.10, 0.13) high temperature permanent

magnets," *J. Appl. Phys.*, vol. 112, no. 3, p. 033909-5, 2012.

[82] W. Tang, Y. Zhang and G. C. Hadjipanayis, "Effect of Zr on the microstructure and magnetic properties of $Sm(Co_{bal}Fe_{0.1}Cu_{0.088}Zr_x)_{8.5}$ magnets," *J. Appl. Phys.*, vol. 87, no. 1, pp. 399-403, 2000.

[83] I. R. Harris, "The potential of hydrogen in permanent magnet production," *J. Less-common Met.*, vol. 131, pp. 245–262, 1987.

[84] I. R. Harris, C. Noble and T. Bailey, "The hydrogen decrepitation of an $Nd_{15}Fe_{77}B_8$ magnetic alloy," *J. Less-Common Met.*, vol. 106, pp. L1–L4, 1985.

[85] P. J. McGuiness, E. Devlin, I. R. Harris, E. Rozendaal and J. Ormerod "A study of Nd-Fe-B magnets produced using a combination of hydrogen decrepitation and jet milling," *J. Mater. Sci.*, vol. 24, no. 7, pp. 2541–2548, 1989.

[86] P. J. McGuiness, "The Study of NdFeB hydrides and their application to the production of permanent magnets," PhD thesis , University of Birmingham, 1989.

[87] M. Kubis, A. Handstein, B. Gebel, O. Gutfleisch, K.-H. Müller and L. Schultz, "Highly coercive $SmCo_5$ magnets prepared by a modified hydrogenation-disproportionation-desorption-recombination process," *J. Appl. Phys.*, vol. 85, no. 8, pp. 5666-5668, 1999.

[88] H. Zijlstra and F. F. Westendorp, "Influence of hydrogen on the magnetic properties of $SmCo_5$," *Solid State Commun.*, vol. 7, no. 12, pp. 857–859, 1969.

[89] J. H. N. van Vucht, F. A. Kuljpers and H. C. A. M. Bruning, "Reversible room-temperature absorption of large quantities of hydrogen by intermetallic compounds," *Philips Res. Repts*, vol. 25, pp. 133–140, 1970.

[90] F. A. Kuijpers and H. H. van Mal, "Sorption hysteresis in the $LaNi_5$-H and $SmCo_5$-H systems," *J. Less-Common Met.*, vol. 23, no. 4, pp. 395–398, 1971.

[91] X. G. Li, A. Chiba and S. Takahashi, "Phase transformation of $SmCo_5$ due to hydrogenation and nitridation," *J. Appl. Phys.*, vol. 81, no. 6, pp. 2895–2897, 1997.

[92] J. S. Raichlen and R. H. Doremus, "Kinetics of hydriding and allotropic transformation in $SmCo_5$," *J. Appl. Phys.*, vol. 42, no. 8, pp. 3166–3170, 1971.

[93] A. Apostolov, L. Bozukov, N. Stanev, T. Mydlarz, "A Change in magnetic properties of R_2Co_7 intermetallic (R = Pr, Sm, Tb and Ho) upon hydrogen absorption," *J. Magn. Magn. Mater.* vol. 50, pp. 286–288, 1990.

[94] Z. J. Cao, L. Z. Ouyang, H. Wang, J. W. Liu, D. L. Sun, Q. A. Zhang and M. Zhu, "Structural characteristics and hydrogen storage properties of Sm_2Co_7," *J. Alloys Compd.*, vol. 608, pp. 14–18, 2014.

[95] C. N. Christodoulou and T. Takeshita, "Reaction of samarium with hydrogen and nitrogen samarium oxides," *J. Alloys Compd.*, vol. 190, no. 1, pp. 99–106, 1992.

[96] J. R. Harris, A. Walton and J. D. Speight "Magnet recycling," US Patent 9,663,843, 30 May, 2017.

[97] J. Evans, C. King and I. R. Harris, "The hydrogenation behaviour of the phases Sm_2Co_{17} and Pr_2Co_{17}," *J. Mater. Sci.*, vol. 20, pp. 817–820, 1985.

[98] T. Ojima, S. Tomizawa, T. Yoneyama and T. Hori, "Magnetic properties of a new type of rare-earth cobalt magnets $Sm_2(Co, Cu, Fe_y M)_{17}$," *IEEE Trans. Magn.*, vol. 13, no. 5,

pp. 1317–1319, 1977.

[99] A. Kianvash and I. R. Harris, "Hydrogen decrepitation as a method of powder preparation of a 2:17-type, Sm(Co, Cu, Fe, Zr)8.92 magnetic alloy," *J. Mater. Sci.*, vol. 20, no. 2, pp. 682–688, 1985.

[100] J. Li, Y. Fang, H. Wang, Z. Guo and W. Pan"Study of hydrogenation decrepitation process on SmCo 2:17-type alloys," *Abstracts of REPM*, pp. 267-269, 2000.

[101] M. Li, Z. Liu, L. Liu "Effect of Fe on hydrogenation and dehydrogenation of $Sm(Co_{bal}Fe_xCu_{0.053}Zr_{0.02})_{7.84}$ (x = 0.2,0.3,0.4,0.5) Alloys," *Abstracts of INTERMAG*, pp. 1-1, 2015.

[102] H. Nakamura, S. Sugimoto, T. Tanaka, M. Okada and M. Homma, "Effects of additional elements on hydrogen absorption and desorption characteristics of Sm_2Fe_{17} compounds," *J. Alloys Compd.*, vol. 222, no. 1–2, pp. 13–17, 1995.

[103] M. Li, Z. Liu, L. Liu, H. W. Zhang, R. J. Chem, X. C. Liu, D. Lee and A. Yan, "Effect of Fe and Annealing Treatment on Hydrogenation," *IEEE Trans. Magn.*, vol. 50, no. 11, pp. 1–4, 2014.

[104] O. Isnard, S. Miraglia, D. Fruchart, D. Boursier and P. L'Heritier, "Coercivity in hydrogen-decrepitated Sm_2Co_{17}-type compounds," *J. Alloys Compd.*, vol. 178, no. 1–2, pp. 23–28, 1992.

[105] M. Zakotnik, D. Prosperi and A. J. Williams, "Kinetic studies of hydrogen desorption in SmCo 2/17-type sintered magnets," *Thermochim. Acta*, vol. 486, no. 1–2, pp. 41–45, 2009.

[106] M. Zakotnik, A. J. Williams, G. Martinek and I. R. Harris, "Hydrogen decrepitation of a 2/17 sintered magnet at room temperature," *J. Alloys Compd.*, vol. 450, no. 1–2, pp. L1-L3, 2008.

[107] H. W. Kwon and I. R. Harris, "Study of $Sm(Co,Fe,Cu,Zr)_{7.1}$ magnets produced using a combination of hydrogen decrepitation and ball milling," *J. Appl. Phys.*, vol. 69, no. 8, p. 5856-5858, 1991.

[108] G. C. Hadjipanayis, R. Hazelton, K. Lawless and L. Horton, "Magnetic domains in rare-earth cobalt permanent magnets," *IEEE Trans. Magn.*, vol. 18, no. 6, pp. 1460–1462, 1982.

[109] H. F. Mildrum, "Magnetization of 2-17 type Sm-Co transition metal sintered permanent magnets," *IEEE Trans. Magn.*, vol. 2, no. 5, pp. 769–771, 1986.

[110] Q. Ma, M Yue, X. Xu, H. Zhang, D. Zhang and X. Zhang, "Effect of phase composition on crystal texture formation in hot deformed nanocrystalline $SmCo_5$ magnets Effect of phase composition on crystal texture formation in hot deformed nanocrystalline $SmCo_5$ magnets," *AIP Adv.,* vol. 8, pp. 056214-4, 2018.

[111] V. Menushenkov, "Phase transformation-induced coercivity mechanism in rare earth sintered magnets," *J. Appl. Phys.*, vol. 99, no. 8, pp. 08B523-3, 2006.

[112] A. J. Mackie, G. D. Hatton, H. G. C. Hamilton, J. S. Dean and R. Goodall, "Carbon uptake and distribution in Spark Plasma Sintering (SPS) processed $Sm(Co, Fe, Cu, Zr)_z$," *Mater. Lett.*, vol. 171, pp. 14–17, 2016.

[113] I. S. Busheina and J. B. Headridge, "Studies in chemical phase analysis. Part I. Determination of the solubilities of elements in certain organic solvent-bromine mixtures," *Analyst*, vol. 105, pp. 600–604, 1980.

[114] C. Zhang, Z. Liu, M. Li, L. Liu, T. Li, R. Chen, D. Lee and A. Yan, "The evolution of phase constitution and microstructure in iron-rich 2:17-type Sm-Co magnets with high magnetic performance," *Sci. Rep.*, vol. 8, no. 1, pp. 1–9, 2018.

[115] W. Tang, Y. Zhang and G. C. Hadjipanayis, "Effect of Ni substitution on the microstructure and coercivity of $Sm(Co_{bal}Fe_{0.1}Ni_yZr_{0.04})_{8.5}$ magnets," *J. Appl. Phys.,* vol. 91, no. 10, pp. 7896–7899, 2002.

Videos

1- https://www.youtube.com/watch?v=KBE5xbUKuLw&feature=youtu.be
2- https://www.youtube.com/watch?v=HA-d3MD0XJk&feature=youtu.be

Bibliography

Publications Related to the Thesis

Journal Articles

A. Eldosouky and I. Škulj, "Recycling of $SmCo_5$ magnets by HD process," *Journal of Magnetism and Magnetic Materials*, vol. 454, pp. 249-253, 2013.

A. Eldosouky, A. Ikram, M. F. Mehmood, X. Xu, S. Šturm, K. Ž. Rožman and I. Škulj, "Hydrogen decrepitation and spark plasma sintering to produce recycled $SmCo_5$ magnets with high coercivity," *IEEE Magnetics Letters*, vol. 9, pp. 1-4, 2018.

A. Eldosouky and I. Škulj, "Hydrogen Reaction with SmCo Compounds: Literature Review," *Journal of Sustainable Metallurgy*, vol. 4, pp. 516–527, 2018.

M. Orefice, A. Eldosouky, I. Škulj and K. Binnemans, "Removal of metallic coatings from rare-earth permanent magnets by solutions of bromine in organic solvents," *RSC Advance*, vol. 9, pp. 14910-14915, 2019.

Conference contribution: oral presentations

A. Eldosouky, A. Ikram, F. Mehmood, S. Kobe , S. Šturm, K. Ž. Rožman and I. Škulj "The use of SPS technique for the production of high coercivity recycled $SmCo_5$ magnet prepared by HD process," *IEEE AIM 2018 Conference*, La Thuile (Italy), 4-7 February 2018.

A. Eldosouky and I. Škulj, "Recycling of $SmCo_5$ magnets by HD process," *Magnetism 2018*, University of Manchester, Institute of Physics, Magnetism Group (UK), 9-10 April 2018.

Other Publications

A. Ikram, M. F. Mehmood, M. Podlogar, A. Eldosouky, R. S. Sheridan, M. Awais, A. Walton, M. M. Kržmanc, T. Tomse, S. Kobe, S. Sturm and K. Ž Rožman "The sintering mechanism of fully dense and highly coercive Nd-Fe-B magnets from the recycled HDDR powders reprocessed by spark plasma sintering," *Journal of Alloys and Compounds,* vol. 774, pp. 1195-1206, 2019.

A. Ikram, A. Walton, A. Eldosouky, K. Ž. Rožman, M. Awais, M. F. Mehmood, R. Sheridan, S. Šturm and S. Kobe, "Particle size dependent sinterability and magnetic properties of the recycled HDDR Nd-Fe-B powders consolidated with Spark Plasma Sintering," *Journal of Rare Earths*, 2019

Biography

The author of this thesis is an Egyptian, born in 1989, in Cairo. He graduated from the Faculty of Science, Helwan University, Cairo, Egypt, in 2010. His graduation project was about the early hydration of cement. After graduation, he worked in a company as a researcher of synthesis auxiliary chemicals, and after that, he was involved in the extraction, recycling and analysis of lanthanides and actinides in the Nuclear Materials Authority of Egypt. In 2013, he joined an Erasmus Mundus program called SERP Chem, where he followed courses about chemistry and material engineering in Italy and Poland, where he also prepared his master thesis about the analysis of lanthanides.